

Application and analysis of marine water jet propulsion

Md. Jiaur Rahman

Naval Architect & Marine Engineer (BUET). AMRINA(UK), MIEB, Managing Director of DNAME.

Email: jia011_buet@yahoo.com.

Abstract

Water jets are common place in vessels needing to achieve speeds of 30+ knots where conventional propeller solutions are unable to overcome the associated issues of cavitation, which in turn can lead to thrust breakdown and material failure. Any vessel designed for high speed requires a low resistance and corresponding slender hull. The propulsor needs to also be capable of accepting a high level of power and hence for a given diameter a high power density. There is a very few papers about the application of water jet propulsion of different type of ship. Water jet propulsion is widely applied in small ship as well as different kinds of big ships which are elaborately discussed in this paper. Here is also discussed the mathematical analysis of different types of water jet inlet as well as over all view of water jet propulsion from early to present as. In this analytical study, the important design variables for water jet propulsion system are established and the theoretical relationships between these variables are derived. Bottom mounted water jet has additional sinkage of stern which is consequence of waterjet hull interaction effect and this effect discussed by various mathematical parameters as well as with graphical presentation.

Key Words: Water jet propulsion, waterjet-hull interaction, hydrofoil, T-craft, SES (surface effect ship).

Nomenclatures:


A_j jet cross sectional area	V_{cr} the critical velocity
A_P Propeller blade projected area	V_A the speed of advance,
C_T coefficient of thrust	V_I the velocity of water at the inlet
C_{Tcr} critical thrust coefficient	V_J the velocity of the jet at the nozzle exit
dE Energy difference between jet and ship	V_S the velocity of the ship
dE` Energy difference between jet and ship with ξ	ω the wake fraction($\frac{V_S-V_A}{V_S}$)
IVR inlet velocity ratio V_i/V or V_i/V_s	v the velocity ratio(V_J/V_S)
m mass of water flowing per second	α the velocity ratio (V_I/V_S)
P_C propulsive coefficient	η_H the hull efficiency (P_E/P_T)
P_E effective horsepower	η_t transmission efficiency, shp/bhp
P_I energy input,	η_P pump hydraulic efficiency
P_i pressure in front of the inlet	η_i propeller efficiency
P_o water pressure below water line	η_J the efficiency of the water jet
P_T thrust horsepower	η_{Jmax} maximum efficiency of the water jet
T propelling force or thrust	ρ density of water
V free stream velocity	ξ loss coefficient




1. Introduction

Propulsion system is very important for a body which passes through a fluid like air or water. Ship is one of the best example as well as space craft, air craft, submarine etc. A moving ship experiences many kind of resistance such as frictional resistance, wind resistance, wave making resistance, eddy making resistance etc. If a ship wants to go ahead with a satisfactory speed, she must overcome these opposite forces with certain speed and this speed can be


gained from the propulsion system of ship. The using propulsion systems in marine vehicles are following categories. Such as 1. Screw propellers propulsion 2. Vertical axis propeller propulsion 3. Water jet Propulsion 4. Paddle Wheels propulsion. In early time jet propulsion was simple but in modern era it is very sophisticated as well as complicated. A jet type mechanical device consists of prime mover and pump which was granted to Toogood and Hayes in 1661. They described a ship having a channel through the centre in which either a plunger or centrifugal pump was installed. Water was sucked in at the bow opening of the channel, accelerated by pump and ejected at the stern as a jet at higher velocity, the reaction providing the thrust. This is one of the earliest references to a form of propulsion often proposed in later years. Benjamin Franklin made a proposal for jet propulsion of a boat in 1775. Water jet propulsion was actually applied by James Rumsey [29] in 1784. He had built an 80 foot steam propelled boat of the hydraulic jet propulsion type and made numerous private experiments with it in the Potomac river for about three years. In 1787 Rumsey held a public demonstration before several hundred people including General George Washington. Between 1830 and 1860 in England alone, there were at least 35 patent applications for different means of propelling ships with water jets. A systematic account of the hydraulic jet propulsion is recorded by Pollard and Dedebout [25] in their "Theorie du Navire" Although the basic principle of these numerous propulsion ideas are the same, there are several different methods of attaining propulsive thrust from the water jet. In the 20th century, interest in the hydraulic jet for ship propulsion has continued and during the last few decades it developed tremendously. There was considerable interest in waterjet for naval vessels. Comparatively trials were made by British Admiralty and the Swedish Government of water jet and propeller-driven ships. More conventional pumps have been used successfully in advance marine vehicles since the 1950's. Hamilton [7] in New Zealand have pursued their own independent approach since 1954. He is the pioneer man of modern waterjet propulsion for small craft. Hamilton applied the waterjet propulsion system in small planing craft where the hull surface was skimmer. Now a day Water jet propulsion is suitable in defense purpose due to produce high speed and low noise as well as use in high speed commercial vessel such as passenger ferry, offshore vessel, patrol craft, littoral combat ship (LCS), multi roll vessel (MRV), sea truck etc.

Water jet Application: Marine water jet propulsion has been used for a variety of ships. This paper highlights their applications below from early times to present times as well as their principle particulars. Latter this paper also highlight the mathematical analysis of marine waterjet propulsion

	<p>PRINCIPLE PARTICULARS</p> <p>Length 160 ft (48.8 m) Beam 43.0 ft (13.1m) Propulsion Water jet Displacement light 150 tons Displacement max 205 tons Design Speed 30 knots at sea state 0 but 25 knots at sea state 3 Crew 18 (2 officers, 1 chief petty Same officer, 15 enlisted) Main Engines Two Detroit Diesel 16V-149TI Same 1600 shp at 1900 rpm.</p>
<p>This vessel is the SES-200. The Coast Guard of USA tested the Navy 110' SES in 1981 before it was extended to 160' (Subsequently, three 110' Bell Halter, Inc. SES's were purchased by the Coast Guard and placed into service in the newly formed SES Division out of Key West, Florida. These vessels have the same main engines as the SES-200. The SES-200 operates below the high wave drag hump speed which is in the 30+ knot range [26] [24][30].</p>	

 <p>It is an innovative T-Craft Demonstrator design has been developed which fully achieves the extremely demanding performance goals defined in the Office of Naval Research Broad of USA. It also known as surface effect ship (SES). This T-Craft have self-deploy over long open ocean distances, interface with Sea Base assets while at-sea, transfer cargo from vessel to vessel in medium sea states, transit at high speed to a tactical location, and ultimately cross sandbars, reefs, and mudflats to get “feet dry” on the beach to discharge its cargo. The T-Craft design progressed through two major phases of development, and included concept exploration, concept development, technology development, and design development efforts. The final design product has been reviewed by ABS and is suitable for beginning Detail Design and Construction, should the program go forward. It has also been shown to be scalable to a wide variety of missions [4].</p>	<p>PRINCIPLE PARTICULAR Length (overall) 80.7 m Beam (overall) 20.6 m Beam (side hull) 5.0 m Lightship displacement 1,358 tonne Tactical payload 305 tonne Full load (tactical) 1,792 tonne Full load (transit) 1,888 tonne Draft (off-cushion) 4.45 m Draft (on-cushion) 1.85 m Survival Sea State SS 8 Maximum Speed 41 knots Propulsion engine Two 22MW gas turbines Water jet Two WLD 1720+ High speed generator One 14MW Air propulsor Four 6.4 m shrouded airscrews Airscrew motor Four 4MW permanent magnetic motors,. Lift fan Four 2.1 m dia. lift fans engine Four MTU 16V4000 diesels</p>
 <p>The hydrofoil ship Tucumari (1968-72) was water jet propelled. This was followed by the PHM which was initiated by a join effort of NATO. Almost six ships like this built and these ships are used for US navy as well as NATO mission. The Tucumcari was effectively used during the Vietnam conflict and led to development of the missile-carrying Patrol Hydrofoil Missile ship (PHM) for NATO, first launched Nov. 9, 1974. Boeing built six PHMs, named Pegasus, Taurus, Aquila, Aries, Gemini and Hercules. The 131-foot PHM carried eight Harpoon anti ship missiles, a 75 mm rapid-fire gun, Rapid Bloom Off board Chaff System and an MK-92 fire control system [10][12].</p>	<p>Model number: 929 Classification: Warship Length: 40 meter Width: 8.6 meter Cruising speed: 40 knots Draft (foilborn): 2.52 meter Propulsion: Two waterjets powered by two 800 HP Mercedes-Benz diesel engines (hull born), one waterjet powered by 17000 HP GE marine gas turbine engine (foilborn) Accommodation: 21 to 24 crew</p>
 <p>The Jetfoil is the name Boeing 929 for a passenger-carrying waterjet-propelled hydrofoil design by Boeing. Boeing began adapting many systems used in jet airplanes for hydrofoils. Robert Bateman led development. Boeing launched its first passenger-carrying waterjet-propelled hydrofoil in April 1974. It could carry from 167 to 400 passengers. It was based on the same technology pioneered by the patrol hydrofoil Tucumcari, and used some of the same technology used in the Pegasus class military patrol hydrofoils. Currently this product line is sold to the Japanese company Kawasaki Heavy Industries [16][12].</p>	<p>First Launch: March 29, 1974 Model number: 929-100 Classification: Passenger Hydrofoil Length: 27.43 meter Width: 9.15 meter Cruising speed: 45 knots Draft (foilborn): 1.73 m to 1.98 m Propusion: Two Allison 501-KF turbine engines with two Rocketdyne waterjet pumps Accomodation: 4 to 8 crew, 250 to 350 passengers.</p>

 <p>This one great beauty of aluminum water jet propelled ship which having speed up to 40 knots at 90% MCR with length overall 107 meters. This high-speed vehicle-passenger ferry “Alakai”, built for Hawaii Superferry, has recommenced its daily service between Maui and Oahu. It’s maximum dead weight 800 tonnes with 866 passengers and 282 cars. The vessel performed very well in the extreme operating conditions upto sea state 6 [32].</p>	<p>PRINCIPAL PARTICULARS Length overall: 106.5 metres Beam moulded: 23.8 metres Hull depth moulded: 9.4 metres Maximum deadweight: 800 tonnes Passengers: 866, Vehicles: 282 cars or 28 trucks 65 cars, Main engines: 4 xMTU 20V 8,000 M71 4 x 8200kW, Gearboxes: 4 x ZF 53000-2 Water jets: KaMeWa 125 S11 Operational speed: 40 knots @ 90% MCR Classification: Germanischer Lloyd</p>
 <p>“Cat No.1”, a 52 metre high speed passenger catamaran, has made an impressive debut in the German Bight for AG Reederei Norden-Frisia. Seakeeping was extremely important to Norden Frisia and was the prime consideration in the vessel’s design to ensure a smooth operation in its North Sea conditions where it will experience significant wave heights of up to 2.5 metres and Beaufort Force 7 winds. In addition to Austal’s well proven rounded-bilge and bulbous-bow semiswath hull form, a unique feature of the aluminum catamaran is its middle bow hull form which only comes into effect in seas greater than 2.0 metres [32].</p>	<p>PRINCIPLE PARTICULARS Length Overall 52.4 metres Length Waterline 45.4 metres Beam (Moulded) 13.0 metres Hull Draft 1.5 metres Passengers. 432 nos Propulsion:Main Engine 4 x MTU 16V 2320kW@2000rpm Gearboxes 4 x Reintjes VLJ 930 Waterjets..... 4 x KaMeWa 71 S11 Service Speed..... 40 knots (100% MCR) Classification..... Germanischer Lloyd.</p>
 <p>This amazing new AIR RIDER have been launched early February 2013. Sporting twin V12 MAN diesels with DOEN water jets and a top speed over 30 knots, this hull re-define performance. Built as a Bangladesh Coast Guard Patrol Vessel and built by Dockyard & Engineering Works, Naryangonj Ltd. This ship is constructed under the author supervision as well as consultancy service. The hull material is aluminum 5083, 6082 and electrode filler material is 5363. Same vessel almost 10 nos built in Malaysia and the designer was Global Marine Design Pty Ltd [33].</p>	<p>PRINCIPLE PARTICULARS Overall Length 20.11 m Waterline Length 16.55 m Beam 5.20 m Draft @ Working Displ. 1.00 m Working Displacement 35 T Light Displacement 31 T Deck height above Waterline 1.80 m Bow Freeboard at rest 2.04 m , Fuel Capacity 6,000 L Engine/s 2 x MAN V12 D2862 LE463 2 x DOEN DJ220 Waterjet Total Installed Power 2 x 1,030 kW 2 x 1,400 HP @ 2100 RPM , Cruise Speed 28 + Knots</p>

	<p>PRINCIPAL DIMENSIONS Length overall 127.1 metres Beam overall 31.4 metres Hull draft (maximum) 4.5 metres Payload and capacities: Complement, Core Crew 40, Mission crew 36 Maximum mission load 210 tonnes Mission packages ASW, SUW, MIW Main engines 2 x GE LM2500 2 x MTU 20V Waterjets 4 x Wartsila steerable</p> <p>PERFORMANCE Speed 40 knots, Range 3,500 nm Operational limitation Survival in Sea State 8</p> <p>WEAPONS AND SENSORS Standard 1 x 57 mm gun, 4 x .50 calibre guns 1 x SAM launcher, 3 x weapons modules</p>
 <p>The vessel is a 290m, 6500t Dwt high speed Pentamaran Ro-Pax vessel designed for SeaBridge International Inc. The vessel is powered by a Diesel Electric Propulsion plant in combination with waterjets. A rendering of the vessel is shown in Figure of The SeaBridge approach uses the sea to complement existing land-based travel on selected routes to attract freight movements away from overcrowded highways, for at least part of the journey from shipper to receiver. By using the sea as a bridge, SeaBridge intends to transport more goods, with less environmental impact, at lower cost, and in a shorter time frame than any comparable transportation alternative available today [9].</p>	<p>PRINCIPLE PARTICULARS LOA 300.00 m LWL 290.00 m Beam Moulded 45.00 m Beam Central Hull WL 20.70 m Design Displacement 30000.0 t Scantling Displacement 34000.0 t Main Engines 8 x MAN 48/60B 18V Waterjets 8 x LIPS/Kamewa Speed at 90% MCR 41.5 knots</p>

Mathematical analysis of water jet: In early of waterjet era, mathematical treatment had started with elementary momentum theory and this theory could not compete with propeller propulsion efficiency with pumps of realistic size. But in present time sophisticated treatment evolve which show that waterjet has a secondary effect and this effect influence on efficiency of waterjet. The simple momentum theory will be discussed here as well as few complicated theory. Let consider a ship, taking water in bow and pump out at nozzle which situated at stern of ship. The bow intake and nozzle connected by a duct and the duct made a tunnel between them. This duct is installed along the centre line of ship and all nozzle water passes through it. When water impulse on water through nozzle then thrust is produced and ship goes ahead. Since intake at bow, no intake losses occur and the intake velocity of water and ship velocity will be equal to each other [1], [18].

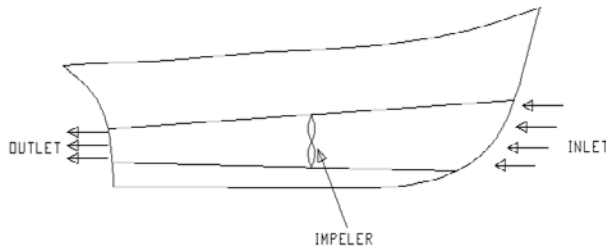


Figure 1 shows duct system which passes water from intake to nozzle.

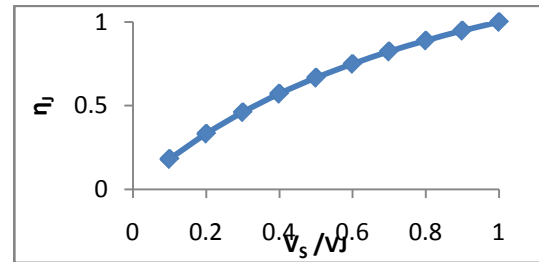


Figure 2: Variation of jet efficiency (η_j) and velocity ratio ($\mu = V_s/V_j$) denoted by ship speed to jet speed.

Now the mass of water discharge per unit time through nozzle, $m = \rho AV_j \dots$ (1), Change in velocity = $(V_j - V_s)$, The thrust developed by water jet $T = \rho AV_s (V_j - V_s) \dots \dots$ (2) Useful work done by waterjet on the ship = thrust * speed of the ship = $TV_s = \rho AV_s (V_j - V_s) V_s \dots \dots$ (3) The waterjet cannot impulse totally on water due to ship velocity. Because of this, a lost velocity occur and which equal to $(V_j - V_s)$. So the lost kinetic energy of jet = $\frac{1}{2} m (V_j - V_s)^2 = \frac{1}{2} \rho A V_s (V_j - V_s)^2 \dots \dots$ (4) Energy delivered by the jet = $\frac{1}{2} m V_j^2$. Let us consider the intake velocity of water at bow V_I . Then energy delivered by the pump $E = \frac{1}{2} m V_j^2 - \frac{1}{2} m V_I^2 \dots$ (5). Where $\frac{1}{2} m V_I^2$ is the inlet kinetic energy of water. Or, $E = \frac{1}{2} \rho AV_j V_j^2 - \frac{1}{2} \rho AV_j V_I^2 = \frac{1}{2} \rho AV_j (V_j^2 - V_I^2) \dots \dots$ (6) So the efficiency of jet, $\eta_j = \frac{\text{Energy output or useful workdone}}{\text{Energy Input by the pump}}$
 $\eta_j = \frac{\rho AV_j (V_j - V_s) V_s}{\frac{1}{2} \rho AV_j (V_j^2 - V_I^2)} = \frac{2(V_j - V_s) V_s}{(V_j^2 - V_I^2)} = \frac{2(V_j - V_s) V_s}{(V_j + V_I)(V_j - V_I)} = \frac{2V_s}{V_j + V_I} \frac{V_j - V_s}{V_j - V_I} \dots \dots$ (7). Let consider the fluid is ideal, therefore $V_s = V_I$

Now the equation (7) become $\eta_j = \frac{2V_s}{V_j + V_I} \dots$ (8) Now introduce a new term μ is ratio of ship speed and jet velocity. Therefore $\mu = \frac{V_s}{V_j}$. So the efficiency becomes $\eta_j = \frac{2\mu}{1 + \mu} \dots$ (9) Based on equation (9) a graphical view is shown in figure 2.

When the forward of the ship or bow need to install something (like a bow thruster), then there is no opportunity to ducting. Therefore the ships have to intake water from another portion of underwater of hull. Let consider the inlets are now in starboard and port of ship in below water level. Now additional kinetic energy is needed to intake water. In this case water in rest condition and ship speed is V_s . If we consider the ship speed zero and water speed V_s with respect to ship then the value of efficiency do not vary. Now the additional intake kinetic energy will be equal to $\frac{1}{2} m V_s^2$. So the efficiency $\eta_j = \frac{\text{Usefull workdone}}{\text{Use full work + Lost kinetic energy of jet} + \text{Additional kinetic energy}} = \frac{\rho AV_j (V_j - V_s) V_s}{\rho AV_j (V_j - V_s) V_s + \frac{1}{2} \rho AV_j (V_j - V_s)^2 + \frac{1}{2} \rho AV_j V_s^2}$

$$\eta_j = \frac{2(V_j - V_s) V_s}{V_j^2} \dots$$
 (10). Let the two ratio $\frac{V_j}{V_s} = v$ and $\frac{V_I}{V_s} = \alpha$, Then the equation become $\eta_j = \frac{2}{v + \alpha} \frac{v - 1}{v - \alpha} = \frac{2(v - 1)}{v^2 - \alpha^2} \dots$ (11)

To obtain maximum jet efficiency, equation (11) have to differentiate with respect to v and it becomes $\frac{d\eta_j}{dv} = \frac{2}{v^2 - \alpha^2} - \frac{2(v - 1)2v}{(v^2 - \alpha^2)^2} \dots$ (12). For maximum value of η_j , $\frac{d\eta_j}{dv}$ equal to must be zero. Hence the equation (12) after simplification becomes $v^2 - 2v + \alpha^2 = 0$, So we get $v = 1 \mp \sqrt{1 - \alpha^2}$, Since v is the ratio of $\frac{V_j}{V_s}$ and V_j is always greater than V_s . So v must be always greater than unity. Taking positive value of above equation for critical velocity and it becomes $v_{cr} = 1 + \sqrt{1 - \alpha^2} \dots \dots$ (13). From equation (2) we know Or $T = \rho Av V_s^2 (v - 1)$ after substituting the value of V_j . But thrust coefficient is defined as follows $C_T = \frac{T}{\frac{1}{2} \rho AV_s^2} \dots \dots$ (14) = $\frac{\rho Av V_s^2 (v - 1)}{\frac{1}{2} \rho AV_s^2}$ Or $C_T = 2v(v - 1) \dots \dots$ (15)

It is known as critical thrust coefficient. If the value of v equal to unity then the critical thrust coefficient is zero. It is possible when jet velocity and ship velocity equal to each other. These characteristics are drawn in figure 3 using equation (15).

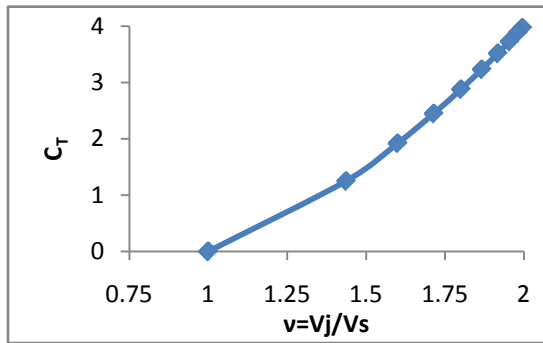


Figure3: Variation of thrust coefficient (C_T) with velocity ratio (v).

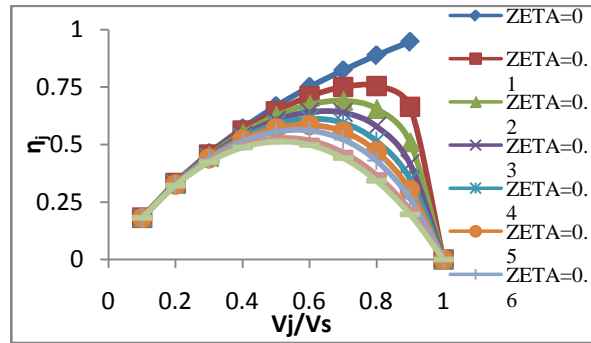


Figure4: Variation of efficiency (η_j) with the ratio of jet velocity to ship velocity (V_j/V_s) at different values of zeta (ξ).

Loss consideration: In case of ideal fluid resistance and drag force of ship and nozzle was not considered. But in real case ship must experience resistance and drag forces which create a loss in efficiency [1]. Let the loss coefficient is ξ . Then the loss term become $(\frac{1}{2}\rho AV_j V_s^2)\xi$. Now the loss energy term will be added with energy difference term dE . So $dE = \frac{1}{2}\rho AV_j(V_j^2 - V_s^2) + (\frac{1}{2}\rho AV_j V_s^2)\xi \dots \dots (16) = \frac{1}{2}\rho AV_j[V_j^2 - V_s^2(1 - \xi)]$. So the jet efficiency $\eta_j = \frac{\text{Useful workdone}}{\text{Energy delivered by pump}(dE)} = \frac{\rho AV_j(V_j - V_s)V_s}{\frac{1}{2}\rho AV_j[V_j^2 - V_s^2(1 - \xi)]} = \frac{2\mu(1 - \mu)}{1 - \mu^2(1 - \xi)} \dots \dots (17)$. Based on the equation (17) following figure 4 can be drawn.

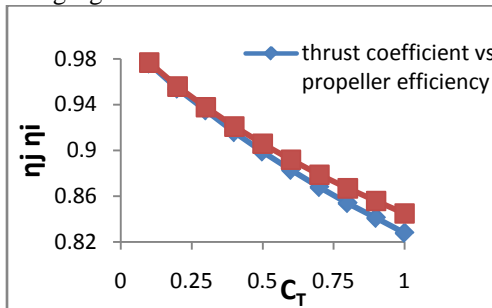


Figure 5: comparison propeller efficiency (η_i) and jet efficiency (η_j) with thrust coefficient(c_T).

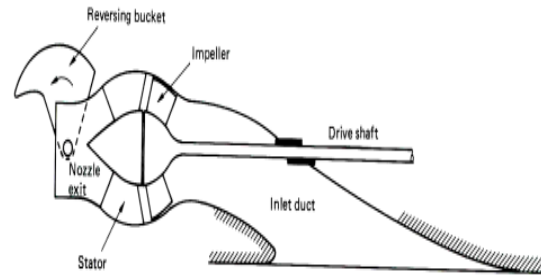


Figure6 shows waterjet propulsion system with suction inlet and nozzle

Jet efficiency can be expressed in terms of thrust coefficient $\eta_j = \frac{4}{3 + \sqrt{1 + 2C_T}} \dots \dots (18)$ Where $C_T = \frac{T}{\frac{1}{2}\rho AV_j V_s^2}$

For propeller the efficiency is $\eta_i = \frac{2}{1 + \sqrt{1 + C_T}} \dots \dots (19)$ Where $C_T = \frac{T}{\frac{1}{2}\rho A_P V_s^2}$.

But the overall propulsive coefficient $PC = \eta_j * \eta_P * \eta_r * \eta_i * \eta_H$. In case of water jet, relative rotative efficiency η_r equal to unity. Therefore the propulsive coefficient become $PC = \eta_j * \eta_P * \eta_i * \eta_H \dots \dots (20)$

Water jet-hull interaction effect: Hydrodynamic characteristics of bottom mounted transom suction waterjet is very complicated. When a ship moving, a continuous flow flowing through duct from inlet to nozzle according to figure6. Water is sucked at inlet opening and exhale at nozzle with very high speed. With respect to water suck speed, inlet flow pattern will be changed according to figure7 and this will discussed latter in this section. Applying Bernoulli's equation between inlet and outlet points, it becomes $\frac{P_i}{\rho g} + h_i + \frac{V_s^2}{2g} = \frac{P_o}{\rho g} + h_o + \frac{V_j^2}{2g} \dots (22)$. The pressure P_o is atmospheric pressure plus water pressure below the water line. The magnitude of P_o and water depth h_o are small with respect to inlet pressure P_i and inlet depth h_i respectively. Now ignoring these P_o & h_o , equation (22) becomes $\frac{P_i}{\rho g} + h_i + \frac{V_s^2}{2g} = \frac{V_j^2}{2g}$. Or, $V_j = \sqrt{(V_s^2 + P_i + \rho g h_i)} \dots (23)$. Here P_i is the static pressure in front of the inlet and $\rho g h_i$ is static pressure at inlet. When ship start to move forward from rest, then the boundary layer at inlet will be accelerated. This acceleration is produced by absorbing pressure energy and the absorption reduce the static pressure at inlet because the total energy is constant (from Bernoulli's Equation). Due to the reduction of static

pressure, jet velocity should be decreased according to equation (23). But at time of operation the jet velocity remains same. Now a question arise in mind that how is it possible? During moving condition, ship stern sinkage is bigger than rest ship sinkage and result of them increasing stern draft[2]. Because of increasing this draft and ship movement, the static pressure in front of the inlet (P_i) is reduced. Due to reduction of this pressure ship is sink further and static pressure (ρgh_i) increase which keep jet velocity V_j remains same.

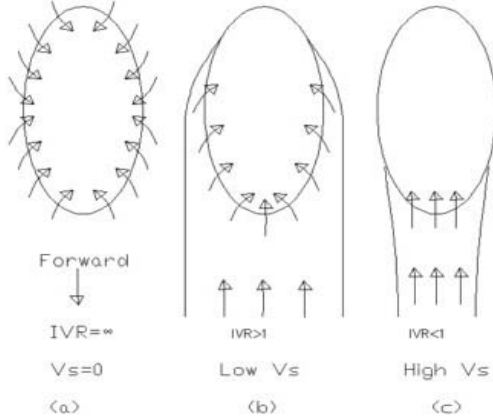


Figure 7 shows inlet flow pattern at different speed.

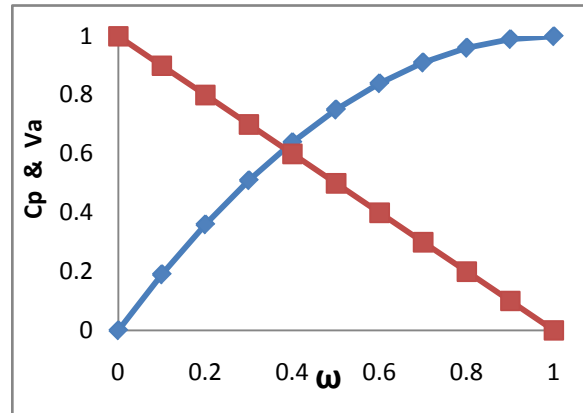


Figure 8 shows the pressure coefficient (C_p) and speed of advance (V_a) with wake fraction (ω).

waterjet-inlet interaction effect discussed by Svenssons [26] and it is about lifting force at the stern of ship and this lifting force is produced in the vicinity of waterjet inlet. Svensson introduce a pressure coefficient C_p and which is equal to $\frac{P_s - \rho gh_i}{\frac{1}{2}\rho V_s^2}$. Therefore it can be written as $C_p = \frac{P_s - \rho gh_i}{\frac{1}{2}\rho V_s^2} \dots (24)$ Where P_s is static pressure in front of the inlet h_i is depth of inlet. This pressure coefficient is related by another relation[27] $C_p = 1 - (\frac{V_a}{V})^2 \dots (25)$ Where V_a is the speed of advance. V is the free stream velocity. But the free stream velocity can be replaced by ship speed V_s and the equation (25) becomes $C_p = 1 - (\frac{V_a}{V_s})^2 \dots (26)$ V_a and V_s are related by another relation that $V_a = (1-\omega)V_s \dots (27)$ Where ω is the wake fraction. Now substitute the value of V_a in equation (26) and it becomes $C_p = 1 - (1-\omega)^2$ Or, $C_p = \omega(2-\omega) \dots (28)$. On the basis of equation (27) and (28) the above figure can be drawn and which intersect at value of ω of 0.38. Let consider the ship is not in underway or in bollard pull test then the inlet velocity flow pattern will be like a patch of skins of figure 7a. In this condition inlet velocity ratio (IVR) is infinite and capture area maximum. If the ship start to move forward with very low ship speed or with IVR of greater than unity, then the stream line will be like figure 7b. In this state the capture area is less than from previous condition but flow entering amount has no variation which is proven from equation of continuity. If ship speed further increase or with IVR less than unity, the capture area will be decreased further without no changing of flow entering amount. But at low IVR condition, the stern of ship sink further due to pressure variation in the vicinity of inlet which is already been discussed earlier in this section.

Results and Discussions: Figure 2 based on equation (5) and shows variation of jet efficiency (η_j) with velocity ratio (V_s/V_j). With increasing velocity ratio, the jet efficiency increases. The increasing rate not linear but slightly decrease with increasing of velocity ratio. That means for lower velocity ratio or at higher velocity of jet, the efficiency is high. Therefore marine water jet propulsion is appropriate for higher velocity. Figure 3 based on equation (15) and it shows that the variation of critical velocity with respect to velocity ratio v . For unity value of v , the critical thrust coefficient is zero. Due to equal velocity of jet and ship or unity value of v , thrust coefficient C_T is zero which is proven from equation (15) as well as from figure 3. Figure 4 based on equation (17) and shows the variation of velocity ratio and jet efficiency with loss consideration. When the loss coefficient ζ is increase successively, the efficiency decreases successively. At ζ equal to zero the efficiency is maximum and same as figure 2 which is for ideal condition. Since the loss coefficient decrease efficiency and the loss associated with duct, the inlet duct system should design in such a way that loss should be minimized. Therefore this formulae help to designer to design water jet system in efficient way. Figure 5 based on equation (18) and (19) and it shows the variation of thrust coefficient with propeller and jet efficiency. The efficiencies are decrease with increasing thrust coefficient but not equally. At very lower value of C_T or higher value of V_s the efficiencies are equal. But at higher velocity of ship, propeller blade break down can be happened which is avoidable in case of waterjet propulsion. Due

to these reasons waterjet propulsion is suitable over the propeller propulsion at higher speed and jet propulsion system generally installed in high speed craft. Figure 8 is drawn on the basis of equation (27) and (28) with unity ship velocity. The pressure coefficient C_p and speed of advance V_a is drawn with wake fraction ω and these curves intersect at point $\omega=0.38$ that is at this value of wake fraction 0.38, pressure coefficient C_p and speed of advance V_a have same values. Higher value of C_p decreases efficiency [1] but lower value reduces ship speed. Another relation speed of advance V_a increases efficiency but the efficiency also depends on other values. This wake fraction with pressure coefficient and speed of advance gives particular type of stream line or inlet flow pattern. This flow pattern involves with lifting coefficient at vicinity of waterjet inlet [1] and with other hydrodynamic characteristics which help designer to design appropriate position and size of waterjet inlet.

Conclusion: In this paper clearly discussed the beauty application of waterjet propulsion in case of small vessel as well as big type of ship with high service speed. From above discussions it is clear that waterjet propulsion can be drive passenger ferry to cruise ship, fire fighting vessel to offshore vessel, vehicle carrier to yacht, pleasure craft etc and these discussions will raise importance of waterjet propulsion to the rest of the world. Mathematical operations are mentioned for all type of inlets which are give different view among them. Waterjet-hull interaction effect has shown with pressure coefficient, wake fraction, speed of advance as well as graphical characteristics of them which help to designer to design inlet size, inlet position etc. Waterjet-hull interaction effect also discussed with Bernoulli's equation and mathematically established the relations among jet velocity, hydrostatic pressure, sinkage, trim etc based on equation (22), (23) & (24).

REFERENCE:

1. Allison J.L., "Marine waterjet propulsion," in Transactions - Society of Naval Architects and Marine Engineers, 1993, vol. 101, pp. 275-335.
2. Arash Eslamdoost, Investigations of Waterjet-Hull Interaction Effects, Department of Shipping and Marine Technology Division of Marine Design Chalmers University of Technology, Gothenburg, Sweden 2012.
3. Baxter B., "Naval Architecture : Examples and Theory", Charles Griffin and Company Limited., London, 1st. Edition, 1977, pp.45-46.
4. Christopher J. Ryan, Mark Redmond, Weimin Hu, Michael Badal, and William Latham, 11th International Conference on Fast Sea Transportation FAST 2011, Honolulu, Hawaii, USA, September 2011. T-Craft – A Transformable Sea Base Connector.
5. Clement, E.P., "Graphs for Predicting the Resistance of Round-Bottom Boats", International Ship-building Progress, Vol. 11, No. 114, February, 1964.
6. Comstock, J.P., "Principles of Naval Architecture", Revised Edition, The Society of Naval Architect and Marine Engineers, New York, 1967, p. 339
7. Davison, G.H., "Modern Marine Jet Propulsion", The naval architect, London, No.6, November, 1979, pp 234-235.
8. Du Cane, P., "High Speed Small Craft", Temple Press Books, London, Third Edition, 1964, p.1.
9. Ed Dudson, Stefan Harries, "Hydrodynamic Fine-Tuning of a Pentamaran for High-Speed Sea Transportation Services". International Conference on Fast Sea Transportation. June 2005, St. Petersburg, Russia.
10. Edgar Scott Ball, Jr. Thesis of Lesson learned from the patrol hydrofoil missile (PHM) Program. Supervisor Alan W Masters, March 1979.
11. Froude, R.E., "On the Constant System of Notation of Results of Experiments on Models Used at the Admiralty Experiments Works", INA, 1888.
12. George Jenkins, Patrol Combatant Missile (Hydrofoil) PHM History 1973 – 1993. Presented in 14 June 1995.
13. Gillmar, T. C. and Johnson, B., "Introduction to Naval Architecture", First edition E. & F. Spon., London, 1982, p 231.
14. Gillmar, T. C., "Modern Ship design", second edition, Naval Institute Press, Annapolis, Maryland, U.S.A., 1975, p.128
15. Haglund, K., Svensson, R. and Bjorheden, O., "Design and Testing of a High Performance Water jet Propulsion Unit", Symposium on small Fast Warship and Security Vessels, The Royal Institute of Naval Architect, London, May, 1982.
16. http://en.wikipedia.org/wiki/Boeing_929
17. Khalil G.M., "Design of a High-Performance Water Jet Propulsion Unit", Report Submitted to the Committee of Advanced Studies and Research, Bangladesh University of Engineering and Technology, Dhaka-1985.
18. Khalil G.M. An Analytical Study of The Hydrodynamic Characteristic of Waterjet Propulsion and The Feasibility of Its Application to High Speed Vessels. Seminar Papers, Offshore Technology Malaysia, 1985.
19. Kim, H.C., "Hydrodynamic Aspects of Internal Pump Jet Propulsion", Department of Naval Architecture and Marine Engineering, The University of Michigan, Ann Arbor, Michigan, May, 1964.
21. Marwood, W.J. & Silverleaf, A., "Design Data for High-Speed, Displacement-type Hulls and a Comparison with Hydrofoil Crafts", 3rd. Symposium on Naval Hydrodynamics, ONR ACR 65, September, 1960.
22. Nordstrom, H.F., "Some Test With Models of Small Vessels", Swedish Tank Publication, No. 19, 195.
23. Numerical Investigation of the Impact of SES-Waterjet Interactions and Flow Non-uniformity on Pump Performance Yin Lu Young, Brant R. Savander and Matthew R. Kramer. 11th International Conference on Fast Sea Transportation FAST 2011, Honolulu, Hawaii, USA, September 2011.
24. Pollard, J. and Dubeout, A., "Theorie du Navire", Vol. IV, 1894, p.201
25. Robert Church, "An Update on SES Design Techniques and Their Application to Repowering the USCG WSES and the USN SES-200" February 1989 Aviation Department Research and Development Report.
26. Svensson, Rolf, "Experience with the KaMeWa waterjet propulsion System," AIAA, Paper No. 89-1440-CP, 1989.
27. T. van Terwisga, "Waterjet hull interaction effect" PhD thesis. Printed by Grafisch Bedrijf Ponsen & Looijen BV, Wageningen 1996.
28. Taggart, R., "Marine propulsion: Principles & Evolution", Gulf publishing company, Houston, Texas, 1969, pp.36-38
29. Todd J. Peltzer P.E "Lifting Body Technology for Transformational Ship Design" 9th naval platform technology seminar 2003.
30. www.austal.com/en/products-and-services/defence-products.aspx, mailinglist@austal.com.

31. www.austal.com/en/products-and-services/commercial-products.aspx, mailinglist@austal.com
32. www.marinekits.com/catalogue.php

Effects of Fibrous Cap Thickness and Stenosis Severity on the Fluid and Structural Behavior in a Model Stenosed Artery

M. Rejaul Haque, M. Emran Hossain Bhuiyan and Dr. A.B.M. Toufique Hasan
Department of Mechanical Engineering
Bangladesh University of Engineering and Technology, Dhaka-1000
E-mail: md.rejaulh@yahoo.com

Abstract

The study of blood flow through a stenosed artery is very important because of the fact that the cause and development of many cardiovascular diseases are related to the nature of blood movement and the mechanical behavior of the blood vessel walls. The interaction between the blood and the plaque may causes the rupture of the plaque. In the present research, study of the blood –plaque interaction using a fluid -structure interaction (FSI) model has been done. The degree of stenosis has been varied from 10% to 70% (by area) and fibrous cap thickness varies from 0.1mm to 2.0mm. Vortex rings are developed at the pre and post stenotic region. Deformation of stenosis, Wall shear stresses (WSS), Peak principle stress and Vonmises stress increases with increasing the degree of stenosis. The peak principle stress found to be maximum (≈ 2000 pa)at the instants of peak velocities of the phasic flow for the case of 70% of stenosis with 0.1mm fibrous cap thickness.

Keywords: stenosis, fibrous cap thickness, rupture, principle stress, fluid-structure interaction

1. Introduction

Blood flow through the artery has the similar behavior with the fluid through a channel. This type of phenomenon can be described by the fluid mechanics engineering. This is known as Hemodynamics. Hemodynamics plays a great role to explain the fluid (Blood) flow behavior through the artery which is inherently unsteady. Structure of the blood vessel includes three layers: Tunica intima (collagen and smooth muscle), Tunica media(elastic fibers, collagen and smooth muscle), and Tunica adventitia (connective tissues consisting of elastic and collagen fibers). There lies a small lumen at the center of artery through which blood flows at a very high pressure. However, due to bad food habit, lacking of physical exercise, oversleeping may cause serious plaque formation in the blood vessels.

The stenosis is defined as a partial constriction of the blood vessel due to the accumulation of cholesterols and fats and the abnormal growth of tissue. Plaque which actually constricts the blood vessel or cause of stenosis consists of Lipid core and fibrous cap. Fibrous cap which covers the lipid core is a thin domain and consists essentially of collagen and smooth muscle cells. The lipid core is formed by fatty composites. The disease caused by this is known as Atherogenesis . Atherosclerotic plaques may rupture without warning under physiological conditions and cause fatal sub sequential diseases such as heart attack and stroke. The exact mechanism causing plaque rupture is not well understood. Stenosis severity has been widely used as a measure of seriousness of stenosis and basis for surgery decision. The stenosis causes the most frequent anomaly in blood circulation .Once the constrictions is formed ,the blood flow is significantly altered and fluid dynamical factors play important roles as the stenosis continues to enlarge leading to the development of cardiovascular diseases such as heart attack and stroke.

The degree of stenosis is quantified by the diametric occlusion in the artery as a percentage of the unobstructed diameter. Pressure losses in stenosed arteries become significant for severe stenosis leads to stroke or infraction, considered as one of the major causes of death and disability in humans. Plaque interacts with the blood flow creating mechanical stresses which can lead to its rupture and which can produce recirculation downstream the plaque. Plaque rupture and recirculation can yield the formation of a thrombus and eventually lead to a heart attack. In this study, development of a FSI model in order to study the interactions between the blood flow and the plaque has been conducted.

In this research, a 2-D simplified model is considered to investigate the several fluid flow and structural behavior such as streamlines, vortex formation, and deformation of plaque, wall shear stress, peak principle stress and vonmises stress for different cap thickness and different degree of stenosis at different time. Both the plaque material is modeled as hyper elastic material guided by Mooney-Rivlin model [1].

In this present study, a plaque with a thin fibrous cap with a moderate Arterial stenosis could also be vulnerable. Therefore, Fibrous cap thickness could be considered as a useful indicator for plaque vulnerability in addition to the traditional measure of stenosis.

2. Modeling Details

The evaluation of the shape of stenosis in real case is not an easy task, as different complex shapes are found which cannot be modeled easily. In order to avoid difficulty 2-D analysis has been considered in the present research. Blood is a non-Newtonian fluid. We have considered it as a Newtonian, homogeneous and incompressible fluid. The apparent viscosity is nearly a constant in large Arteries with diameter ($\approx 5\text{mm}$) and therefore the non-Newtonian effects can be avoided. Here modeled Artery's diameter is 10mm as shown in Fig.1. The Governing equations for fluid domain are 2D Navier strokes equations and for solid domain structural properties are included under the FSI study.

2.1 Fluid Domain

Governing equations are Navier-Stroke equation(1):

$$\frac{\rho \partial V}{\partial t} + \rho(V \cdot \nabla)V = -\nabla P + \mu \nabla^2 V \quad (1)$$

At solid-fluid interface boundary, the condition is governed by equation (2) and equation (3):

$$U_{fluid} = U_w \quad (2)$$

$$U_w = \frac{\partial U_{solid}}{\partial t} \quad (3)$$

A simple model of the artery with one-sided cosine shaped stenosis is considered in the present study. The experimental investigation of Ahmed and Giddens [2] considering pulsatile flow through an axisymmetric smooth stenosis was studied here. The geometry used was similar to theirs with the stenosis shape given by a cosine functioned equation (4). If H is the height of the nonstenotic part of the tube, $S(x)$, gives the shape of the stenosis.

Where S_0 is the % stenosis severity with x_1 and x_2 specifying the position and length of the stenosis.

$$S(x) = \frac{S_0 H}{2} [1 - \cos\{2\pi(x - x_1)/(x_2 - x_1)\}]/2 \quad (4)$$

The Height of the artery H is 10 mm. The viscosity of the blood is taken as $\mu = 3.4 \times 10^{-3} \text{Pa.s}$ with a mass density of $\rho = 1035 \text{ Kg m}^{-3}$. At the inlet boundary the input velocity expression is given by equation (5):

$$v = v_0 \sin\left(\frac{2\pi t}{T}\right) \quad (5)$$

Where, $T = \text{pulse period}, v_0 = 0.12 \text{ m/s}$

(Corresponding to Reynolds number $Re = 366$)

The Womersley parameter ($\alpha = H/2 \times \sqrt{2\pi\rho/T\mu}$), for our investigation is found 8.26. Observation has been made at the point of maximum acceleration, maximum velocity and maximum deceleration. All the Arterial boundaries are given no-slip boundary conditions. In the present study, the simulations are carried out using a available CFD software which FSI is handled by means of the ALE formulation. The entire domain is subdivided into 7000~12424 triangular elements.

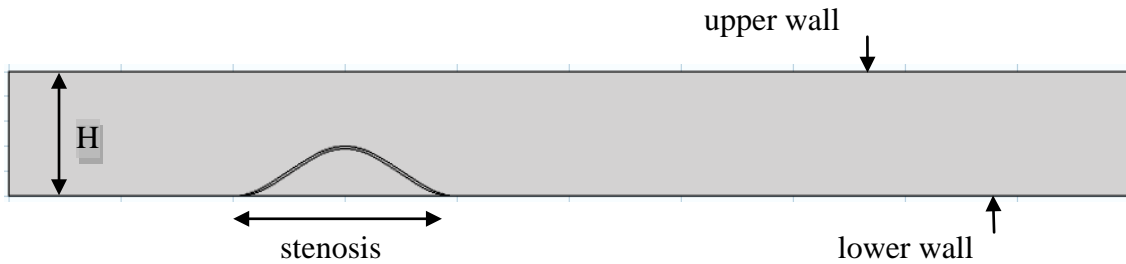


Fig. 1. Schematic of an arterial stenosis

2.2 Solid Domain

The lipid pool and the fibrous cap are modeled as isotropic nearly incompressible hyper elastic materials. For hyper elastic materials, the stress-strain relationship is nonlinear and derives from a strain energy function w . Due to the isotropy of the materials, this function is expressed in terms of invariants of deformation tensors.

For near incompressible material, the energy function w is splitted into distortional and volumetric parts as shown by equation(6):

$$W = w(c) + U(j) \quad (6)$$

In the present study w is defined according to the Mooney-Rivlin model. Hence the energy function is stated by equation (7):

$$W_s = C_{10} (\bar{I}_1 - 3) + C_{01} (\bar{I}_2 - 3) + \frac{1}{2} \kappa (J_{el} - 1)^2 \quad (7)$$

Fibrous cap

$$C_{10}=9200 \text{ Nm}^{-2}$$

$$C_{01}=0 \text{ Nm}^{-2}$$

$$\kappa=3000 \text{ MPa}$$

Lipid deposit

$$C_{10}=500 \text{ Nm}^{-2}$$

$$C_{01}=0 \text{ Nm}^{-2}$$

$$\kappa=200 \text{ MPa}$$

The fibrous cap and lipid deposit densities are taken as 1000 Kgm^{-3}

These data are taken from papers [1].

3. Results and Discussion

The streamline flow pattern is disturbed due to the presence of stenosis. As the flow is sinusoidal time dependent, significant flow variations on the pre and post stenotic region are observed. The features of interests are the recirculations and the stress over the plaque. From Fig. 2. and Fig. 3. it is clearly observed that ,with the increase of percentage of stenosis the vortex rings are seen not only at lower boundary but also affects the upper boundary at the same instant of time due to large area constriction provided by the accumulation of the the fatty decomposites.

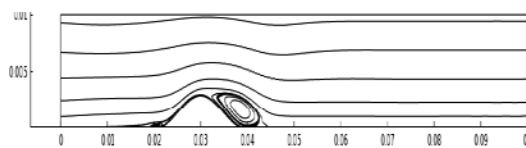


Fig. 2. vortex rings for $S_0 = 30\%$ at $t/T = 0.37$

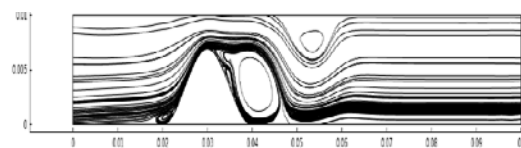


Fig. 3. vortex rings for $S_0 = 70\%$ at $t/T = 0.37$

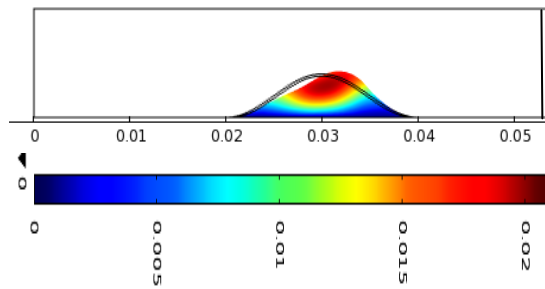


Fig. 4. Displacement field for 30% stenosis and 0.1 mm fibrous cap thickness

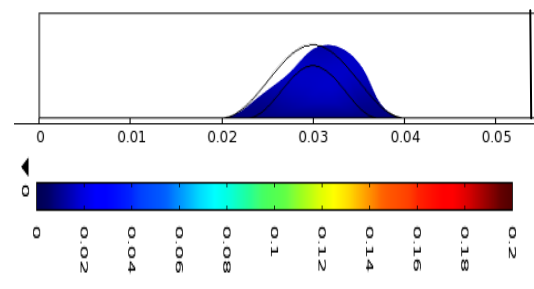


Fig. 5. Displacement field for 70% stenosis and 2 mm fibrous cap thickness

The displacement field have been shown with color range in Fig.4. and Fig.5. In the first figure the red portion shows a displacement value ranging from 0.015-0.02mm while in case of second fig the deep blue portion shows a range of values near to the first one. This clearly implies that, 30% stenosis with 0.1 mm fibrous cap thickness can be considered as the same threat to that of offered by the 70% stenosis with 2mm fibrous cap thickness.

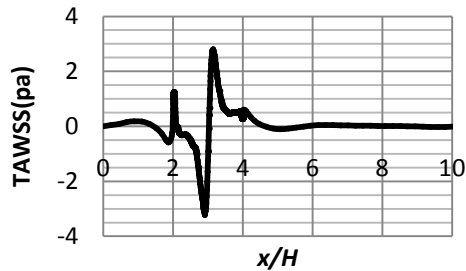


Fig. 6. Time Averaged Wall Shear Stress for 70 % stenosis with 0.1mm fibrous cap thickness at lower boundary

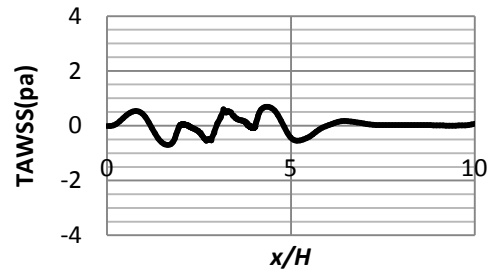


Fig. 7. Time Averaged Wall Shear Stress for 70 % stenosis with 2mm fibrous cap thickness at lower boundary

Fig. 6. and Fig. 7. represent the Time averaged wall shear stress as the wall shear stress varies sinusoidal with the inlet inflow. However, TAWSS are plotted along the length of the stenosis in a dimensionless form and for same degrees of stenosis (70% here), it shows a lower peak with the increase of fibrous cap thickness.

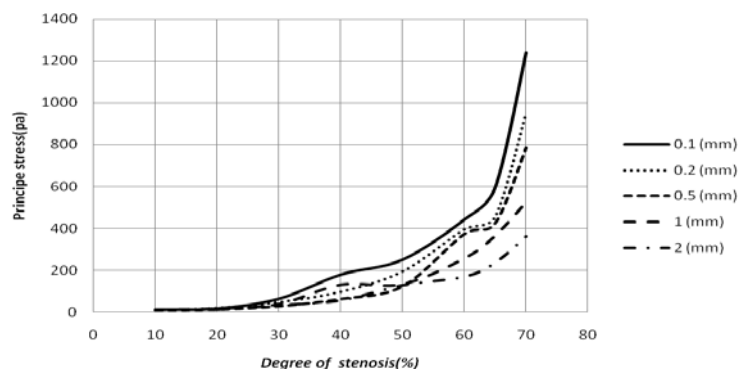


Fig. 8. variations of Principle stress with degree of stenosis for different fibrous cap thickness

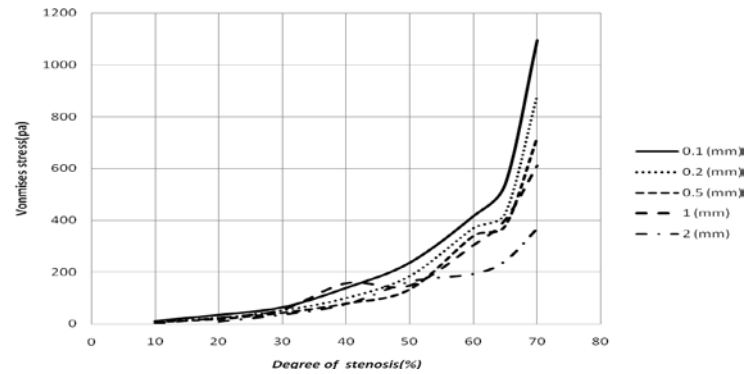


Fig. 9. variations of Vonmises stress with degree of stenosis for different fibrous cap thickness

Variations of principle stress and vonmises stress for different degrees of stenosis and fibrous cap thickness are shown in Fig. 8. and Fig. 9. Fig. 8 implies that 200 Pa principle stress can be occurred within the plaque shoulders for different combinations such as : 1)40% stenosis with 0.1mm fibrous cap thickness 2)50% stenosis with 0.2mm fibrous cap thickness 3) 65 % stenosis with 2 mm fibrous cap thickness. As a result, for determining the rupture risk, all poses the equal amount of threat to the patient's evaluation. So, the main theme of the present research is to examine the patient not only by the presence of degree of stenosis but also by the thickness of fibrous cap thickness which is often be neglected within the moderate range of stenosis (30%-70%). Stenosis higher than 70% actually impose a higher threat to plaque vulnerability whatever the fibrous cap thickness is.

4. Conclusion

This paper is devoted to the study of the fluid-structure interactions between the blood flow and the plaque in a 2D geometry of a modeled Arterial stenosis. The computations show that Plaque stress/strain analysis is important for a better understanding of plaque rupture process. Critical stress/strain conditions are very sensitive to changes in pressure conditions, material properties, plaque structure, lipid pool size, shape and position and various model assumptions. However, to determine the plaque vulnerability Patients in the future may be examined not only by the degree of stenosis but also by the appearance and thickness of fibrous cap thickness.

5. References

- [1] N.El Khatib,S.Genieys,A.M.Jine and V.Volpert, Non-Newtonian effects in a fluid-structure interaction model for atherosclerosis.*Journal of technical physics*.50,55-64.2009
- [2] Ahmed S.A. and Giddens , D.P., Pulsatile post stenotic flow studies with laser Doppler anemometry, *journal of Biomchanics*.17,695-705.1984.
- [3] Dalin Tang, Chun Yang, Shunichi Kobayashi, David N. Ku., Effect of a lipid pool on Stress/Strain distribution in Stenotic Arteries: 3-D Fluid- Structure Interactions (FSI) Models,126,363-370,2004.
- [4] Zhi-Yong Li, Simon P. S. Howarth, Tjun Tang and Jonathan H. Gillard. How critical is fibrous cap thickness to carotid plaque stability?: A flow-plaque interaction model, 37,1195-1199.2006.
- [5] Bathe. M. and Kamm. R. D. A fluid-structure interaction finite element analysis of pulsatile blood flow through a compliant stenotic artery, 121,361-369.1999.
- [6] S. Chakravarty, Effect of stenosis on the flow behavior of blood in an artery, *International journal of engineering science*, 25, 1003-1018.1987.

Experimental Analysis on Minor Head Loss for Flow through Locally Manufactured Ball Valve for Supplying Fluid in Bangladesh

Sadia Haque¹, M. Q. Islam²

¹ Department of Mechanical Engineering, Bangladesh university of engineering & Technology
E-mail: sadia@daffodilvarsity.edu.bd

² Department of Mechanical Engineering, Bangladesh university of engineering & Technology
E-mail: quamrul@me.buet.ac.bd

Abstract

An experimental set up is developed to test the locally manufactured two way ball valve usually used to supply water in different residential, industrial, medical and many other purposes in Bangladesh. Minor loss due to flow through the valve is our prime interest. The well-known Darcy-Weisbach equation is used to calculate the minor loss coefficients. Minor loss coefficients are obtained for three different size valves (3/4,1/2,1 inch diameter) under various opening conditions(20%,40%,60%,80%&100%) and flow rates. From the experiment it is found that the minor loss coefficient decreases with the increase of percentage opening of valve & also with the increase of Reynolds number.

Keywords: Ball valve, Minor loss coefficient, Darcy-Weisbach equation.

1. Introduction

This paper is basically concentrated on the ball valve which is very popular and useful in industrial & medical applications. Various types of fluids can be flowed through ball valve such as compressed air, gases, liquid chemicals, oil, hot and cold water, steam, flammable liquid etc. In Bangladesh these ball valves are available in local market, which are manufactured locally, but relevant data of head loss associated with these locally manufactured ball valves are not available.

The purpose of a valve is to provide a means to regulate the flow rate. This is accomplished by changing the geometry of the system i.e., closing or opening the valve alters the flow pattern through the valve, which in turn alters the losses associated with the flow through the valve. The flow resistance or head loss through the valve may be a significant portion of the resistance in the system. In fact, with the valve closed, the resistance to the flow is infinite - the fluid cannot flow. Such minor losses may be very important indeed. The minor loss coefficient, k varies with a number of factors. These are: type of valve used, flow velocity of fluid through the valve, the percentage valve opening, other fittings associated with the valve, Valve size, geometry. Here the Reynolds number and the percentage opening are considered as most suitable depending parameters.

2. Methodology

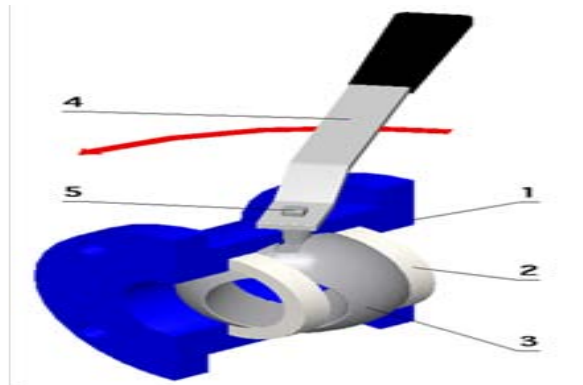
For directing the experimental investigation three size(1/2, 3/4,1 inch diameter) locally manufactured manually operated two way ball valves are taken. For the calculation the main equation used is:

$$H_L = K \frac{V^2}{2g} \quad (1)$$

Where, k = Loss coefficient

V = velocity of flow (m/sec)

$g = \text{gravity (m/sec}^2\text{)}$



1.Body, 2. Seat, 3.Disc (ball), 4.Handle (lever), 5.Stem

Fig. 1: Cut-way view of a simple manual ball valve.

The components used in preparing the experimental setup are reducer, bends (90 degree), U-tube manometer, Mercury & carbon tetra chloride as working fluid in the manometer, weight measuring instruments, nipple joints, thread tape etc. At first the inside diameter of the ball valve and the pipe are measured. Then cross sectional area of the ball valve and pipe are calculated. The valve position for 20, 40, 60, 80 and 100 percent openings were marked on the ball valve. During the experiment, the handle would be placed upon those marks to keep the valve open up to desired percentages. The ball valve is connected between two pipes. Two pipe openings are created on either side of the valve and nipple joints threaded to them. The distances of the openings from the valve are approximately 6 times of the pipe diameter. Flexible tubes are connected to the inlets of the manometer. The other ends of the tubes are connected to the nipple joints threaded to the pipes either side of the valve. Water is allowed to flow inside the pipe which would fill up the manometer with water. The in-flow end of the pipe-valve setup is threaded to the reducer connected to the water supply line. Bends are connected to the out-flow end of the pipe-valve setup so that the full flow of water occurs inside the pipe when water flows out of the setup. Then valve is opened up to 20 percent opening. The valve connected to the supply line is opened very carefully to start water flow. When an observable deflection is found in the manometer the flow rate is kept constant and the deflection is measured. The discharge rate of water also measured. Deflections are measured several times by increasing flow rate. Similarly for each required percentage opening of valve flow rates are changed and the corresponding deflections are measured. Same procedure is performed for each valve.

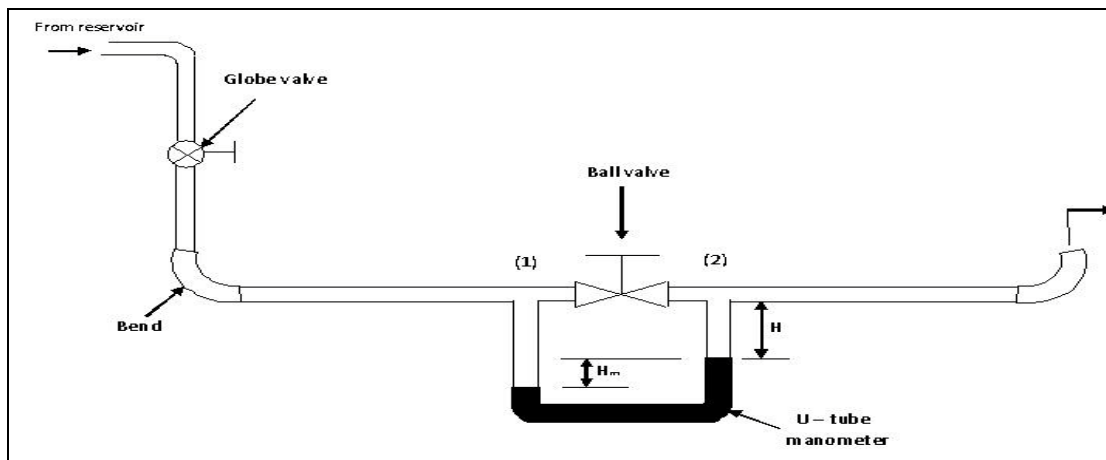


Fig.2: Schematic Diagram of the Experimental Set-up

3. Result and Discussion

For every valve the same trends observed. For a particular pipe-valve system, at a particular percentage opening, the geometrical properties (d), and the fluid properties (ρ and μ) remain constant. So Reynolds number varies with velocity (v) directly. In this experiment it is observed that for a particular percentage opening, when the Reynolds number is increased, the Minor loss coefficient, k decreased. The value of k is observed large at low Reynolds number for smaller openings. Also k decreased sharply for small openings as Reynolds number is increased. For the larger openings (80 and 100 percent), the values of k are lower, k decreased at a lower rate and the pattern is almost linear. The same observations are made for the all three valves. The minor loss coefficient, k decreases as the percentage opening is increased. As the area of the fluid flow increases, the flow becomes more uniform and less turbulent. Minor loss mainly occurs due to change in flow pattern and direction created by the valve. So at large openings the flow is less turbulent and as such the losses are reduced. It is also observed that the minor loss coefficient decreases with the increase of valve size.

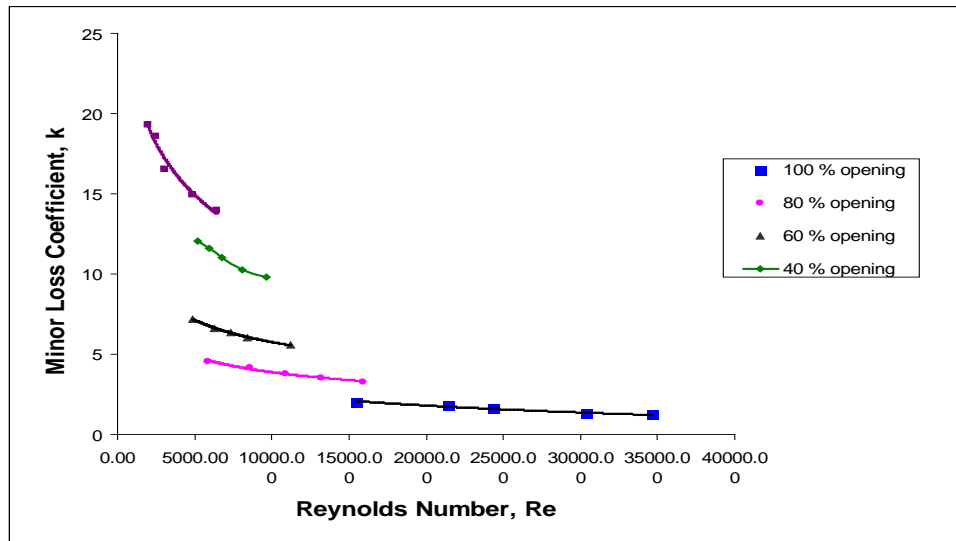


Fig. 3: Minor Loss Coefficient vs. Reynolds Number for 1/2 inch valve

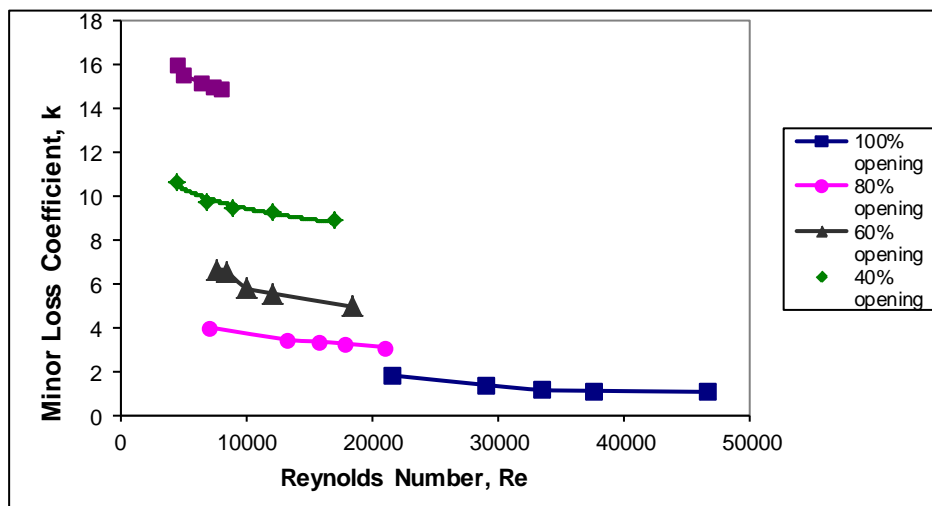


Fig. 4: Minor Loss Coefficient vs. Reynolds Number for 3/4 inch valve

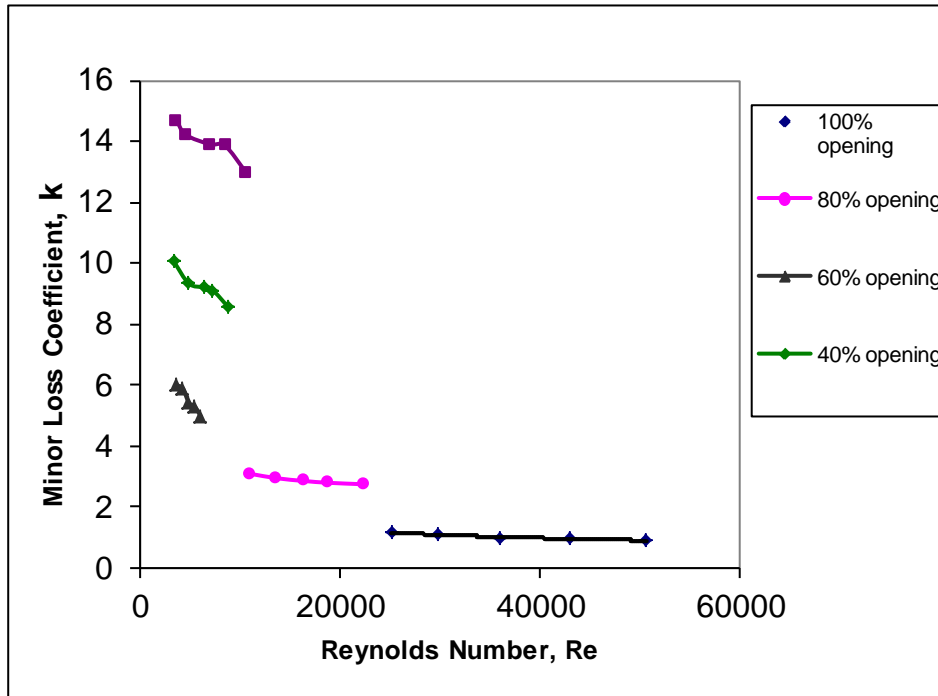


Fig 5: Minor Loss Coefficient (k) vs. Reynolds Number (Re) for 1 inch valve

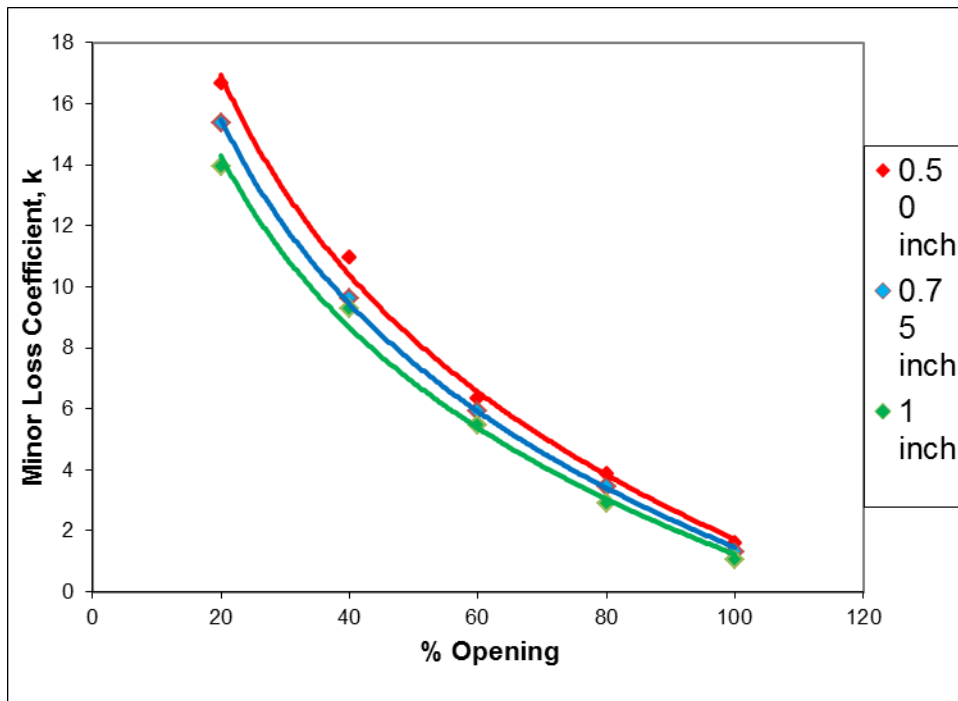


Fig. 6: Minor Loss Coefficient vs. % Opening for 1/2, 3/4 & 1 inch valve

Table 1. Minor Loss Coefficient and Reynolds number for various openings for ½, ¾ and 1 inch valves

Percent Opening	Observation No.	½ inch valve		¾ inch valve		1 inch valve	
		Minor Loss Coefficient k	Reynolds Number, Re _D	Minor Loss Coefficient	Reynolds Number Re _D	Minor Loss Coefficient	Reynolds Number, Re _D
100	1	2.01	15475.83	1.83	21596.90	1.28	25158.49
	2	1.82	21451.65	1.39	29098.98	1.1	29705.21
	3	1.62	24362.94	1.17	33418.36	0.98	36070.61
	4	1.31	30338.76	1.13	37510.40	0.96	43042.24
	5	1.19	34629.09	1.08	46603.83	0.93	50620.1
80	1	4.56	5822.59	4.03	7047.41	3.1	13640.15
	2	4.18	8580.66	3.47	13185.47	2.95	16974.4
	3	3.8	10879.05	3.83	15686.17	2.86	20308.66
	4	3.52	13177.44	3.29	17732.19	2.8	23946.03
60	5	3.29	15935.51	3.13	20914.89	2.75	27889.52
	1	7.21	4903.23	6.68	7789.42	6.55	3334.26
	2	6.6	6282.27	6.59	8411.42	5.78	4243.6
	3	6.32	7354.85	5.83	10002.77	5.46	4546.72
	4	6.05	8427.43	5.58	12048.80	5.02	5456.03
40	5	5.57	11185.5	4.97	18414.2	4.49	6365.4
	1	12.08	5209.68	10.68	4546.72	10.08	3335.26
	2	11.58	5975.82	9.78	6820.07	9.54	4546.72
	3	11.01	6741.95	9.45	8866.10	9.15	6366.4
	4	10.25	8120.98	9.30	12048.8	8.86	7577.86
20	5	9.78	9653.24	8.89	17050.18	8.67	8790.32
	1	19.28	1991.94	16.03	4546.72	15.33	3637.37
	2	18.61	2451.62	15.57	5001.39	14.64	4546.72
	3	16.54	3064.52	15.23	6365.40	13.66	6971.63
	4	14.95	4903.24	15.01	7274.74	13.24	8487.2
	5	13.97	6435.49	14.96	7956.75	12.78	10609

Table 2. Average Minor Loss Coefficient for various openings for ½, ¾ and 1 inch valves

% Opening	Average Minor Loss Coefficient, k		
	½ inch valve	¾ inch valve	1 inch valve
20	16.67	15.36	13.93
40	10.94	9.62	9.26
60	6.35	5.93	5.46
80	3.87	3.46	2.89
100	1.59	1.32	1.05

4. Conclusion

- Minor loss coefficient depends on percentage opening of valve, Reynolds number and size of valves significantly.
- In this study only metallic valves were used. Locally manufactured valves constructed of other materials, namely plastic, should also be included in the study.
- Minor loss phenomena are also prevalent in other valves used in piping system. Further studies should be undertaken including different valves.
- Due to constrain in resources minor loss coefficients are obtained for a small number of Reynolds number flows. Studies should be carried out for other Reynolds number flows also.

5. References:

- [1] V. L. Streeter, E. Benjamin Wylie, Fluid Mechanics. First SI Metric Edition, McGraw-Hill Book Co., Singapore.
- [2] P.N. Modi, S.M. Seth, Hydraulic and Fluid Mechanics Including Hydraulic Machines. Fourteenth edition 2002, Standard Book House.
- [3] Md. Quamrul Islam, A.K.M Sadrul Islam, Fluid Mechanics Laboratory Practice, World University Service Press, ISBN 984-518-000-0.
- [4] Md. Ashiqur Rahman, Md Faisal Haider, Md. Farhadul Haque, "Study of Different types of valves and Determination of minor head loss for various openings of locally available plastic valves". BUET, March 2009.
- [5] Md. Yahya Hussain, S.M. Golam Mourtuzza, Md. Azimussan Abbasi, "Minor Head loss for various openings of locally available plastic valves". BUET, January 2008.

Flow topology around two square cylinders in side-by-side arrangement

Md. Mahbub Alam^{1,*} and Y. Zhou^{1,2}

¹ Institute for Turbulence-Noise-Vibration Interaction and Control, Shenzhen Graduate School, Harbin Institute of Technology, Shenzhen, China

² Department of Mechanical Engineering, The Hong Kong Polytechnic University
Hung Hom, Kowloon, Hong Kong

E-mail: alamm28@yahoo.com

Abstract

The wake of two side-by-side square cylinders is experimentally investigated in details at a Reynolds number of 300 to explore its intrinsic features, including the gap vortices, flow switch, stability, merging of two streets into one, etc. The cylinder center-to-center spacing ratio T^* ($= T/W$, W is the cylinder width) is varied from 1.0 to 5.0. Four flow regimes are identified: (i) the single bluff body regime ($T^* < 1.2$), (ii) the narrow and wide street regime ($1.2 < T^* < 2.1$), (iii) the transition regime ($2.1 < T^* < 2.4$), and (iv) the coupled-street regime ($T^* > 2.4$). At Regimes (ii) and (iii), the two opposite-signed vortices separated from the gap side of the cylinders behave like a conjoined twin and tend to move together. Their movement direction depends on the phase lag between them. Two streets formed immediately behind the cylinders merge to a single street at a downstream location x_c^* that depends on T^* . A larger T^* corresponds to a larger x_c^* . Regime (iv) is characterized by two streets either inphased or antiphased. The antiphased streets are more stable than the inphased.

Keywords: flow topology, bistable flow, square cylinders, side-by-side arrangement.

1. Introduction

The wake of two side-by-side cylinders has attracted a great deal of attention in the literature because of its fundamental importance in understanding many industrial flows, for example, flows around high-rise buildings, chimney stacks, tubes in heat exchangers, overhead power-line bundles, bridge piers, stays, masts, chemical-reaction towers and offshore platforms, etc. The vortex shedding process, gap flow switch, vortex and street interactions are the key features of this flow, which are complicated and fascinating. These phenomena are strongly dependent upon the cylinder center-to-center spacing ratio T^* . Superscript ‘*’ denotes normalization by the cylinder width W . They are further linked to the downstream evolution of vortex frequencies and dramatic change in forces and pressure distributions on each cylinder [1, 2].

In spite of its great relevance to engineering, the flow around two square cylinders has received much less attention than that around two circular cylinders. Sakamoto and Haniu [3] investigated aerodynamic forces, Strouhal number (St) and cross-correlation between fluctuating pressures on two side-by-side square cylinders, with an aspect ratio of 3, immersed in a thick turbulent boundary layer. They failed to observe the bistable phenomenon of the gap flow. Using a two-component laser Doppler velocimeter, Kolar et al.

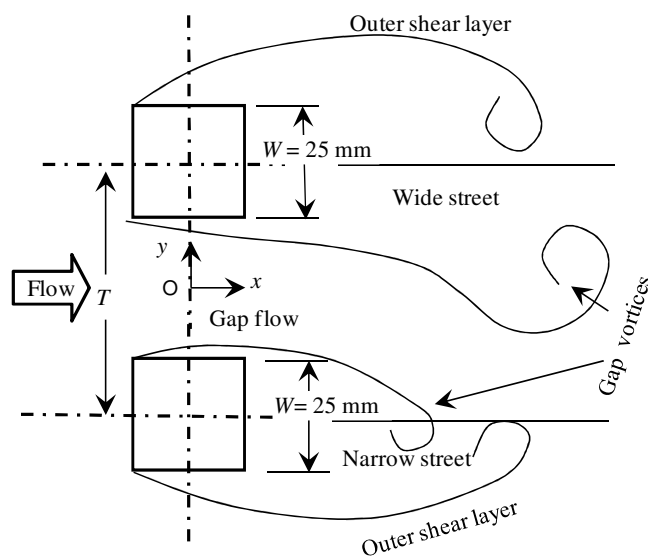


Fig. 1. Schematic of cylinders and definitions of symbols

[4] measured the wake of two side-by-side square cylinders at a Reynolds number (Re) of 2.3×10^4 over $x^* = 1 \sim 9$, where x is the streamwise distance from the cylinder centers (Fig. 1). The flow was studied in detail only at $T^* = 3$, providing no information on flow in other T^* . Agarwal et al. [5] investigated the laminar wake ($Re = 73$) of two side-by-side square cylinders at $T^* = 1.7$ and 3 numerically using a lattice Boltzmann method. They observed coupled vortex shedding from the two cylinders at $T^* = 3$, and a biased gap flow at $T^* = 1.7$. The gap flow could switch randomly from one side to the other, forming narrow and wide streets behind the cylinders. The two streets are connected to different vortex shedding frequencies.

The flow structure in the narrow and wide streets is complicated by the gap flow switch, which may have a timescale of several orders of magnitude longer than those of vortex shedding and shear layer instability. The two streets, generated by the two cylinders, respectively, merge into one single large-scale street (Fig. 2). The flow physics behind the merging has yet to be completely understood. It is expected that the downstream position where the two streets merge should be dependent on T^* in addition to other parameters such as Re , turbulent intensity, etc. However there is no quantitative information available in relation to this aspect. Other aspects of the flow are also interesting. For example, why is the gap flow biased? Under what condition does the deflected gap flow switch to the other side? What kind of vortex interactions is associated with the gap flow switch? How do the two streets evolve into a single one? The issues raised above motivate this work. In order to capture the flow structure details of interest, the present investigation is conducted at a low Re of 300 for $T^* = 1.0 \sim 5.0$ based on laser-induced fluorescence flow visualization. Various aspects of the flow are carefully examined, including vigorous interactions between gap vortices, non-stationary gap flow switching, downstream flow evolution and changeover from the antiphased to inphased coupled streets or vice versa

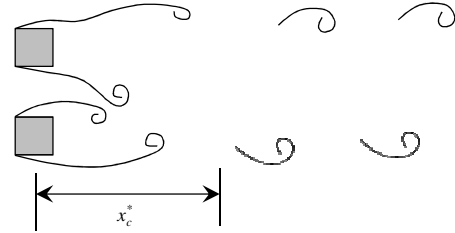


Fig. 2. Two streets merge into one.

2. Experimental details

Figure 1 presents the schematic of the cylinder arrangement, along with the definitions of symbols. The Cartesian coordinate system is defined such that the origin is at the midpoint between the two cylinders, with the x - and y -axis along the streamwise and lateral directions, respectively. Flow visualization experiments were conducted in a water tunnel in the Department of Mechanical Engineering at The Hong Kong Polytechnic University. The test section is rectangular, 0.3 m in width, 0.6 m in height, and 2.0 m in length. Two square cylinders of $W = 25$ mm were arranged side-by-side and mounted vertically across the height of the tunnel. Flow visualization was performed at the free-stream velocity $U_\infty = 0.012$ m/s, corresponding to $Re = 300$. Dye (Rhodamine 6G 99%) was introduced into flow from the midspan of the cylinders through three pinholes (spaced 2 mm) at each leading edge. A thin laser sheet, generated by laser beam sweeping, provided illumination in the vertical plane through the mid-span of the cylinders. A Spectra-Physics Stabilite 2017 Argon Ion laser (4 watts) was used to generate the laser beam. A digital video camera was used to record the dye-marked vortex street at a framing rate of 25 frames per second. Experiments were done for $T^* = 1.0, 1.1, 1.3, 1.5, 1.75, 2.0, 2.25, 2.5, 2.75, 3.0, 3.5, 4.0,$ and 5.0.

3. Results and discussion

3.1. Flow structure and its downstream evolution

Figure 3 presents the flow structure and its downstream evolution for various T^* . There is no flow through the gap at $T^* = 1.0$ (Fig. 3a) and the gap bleeding is hardly discernible at $T^* = 1.1$ (Fig. 3b). In both cases, a single street of vortices forms, characterized by alternate vortex shedding from the free-stream sides of the cylinders. The corresponding St is about one half of that in an isolated cylinder wake, as the effective bluff-body width is doubled. As T^* is increased to 1.3, the gap flow grows to a strength enough to split the wake into two streets (Fig. 3c). Nonetheless, with insufficient momentum, the gap flow swerves aside, forming one narrow and one wide street (Fig. 3c). The gap flow rolls up, forming two oppositely signed vortices; both running into the narrow street. The narrow street has a smaller vortex formation length than the wide one. The two streets have their identities at $x^* < 3.8$, though merging into one street at the critical distance $x_c^* = 3.8$ for $T^* = 1.3$ and displaying only two rows of vortices. For larger T^* , up to $T^* = 2.0$ (Fig. 3d-f), the gap flow grows in momentum and becomes gradually less biased, the difference in width between the narrow and wide streets diminishing. However, the two streets merge into one in the downstream. It may be concluded that a single bluff-body wake occurs at $T^* < 1.2$ but one narrow and one wide street are generated for $1.2 < T^* < 2.1$.

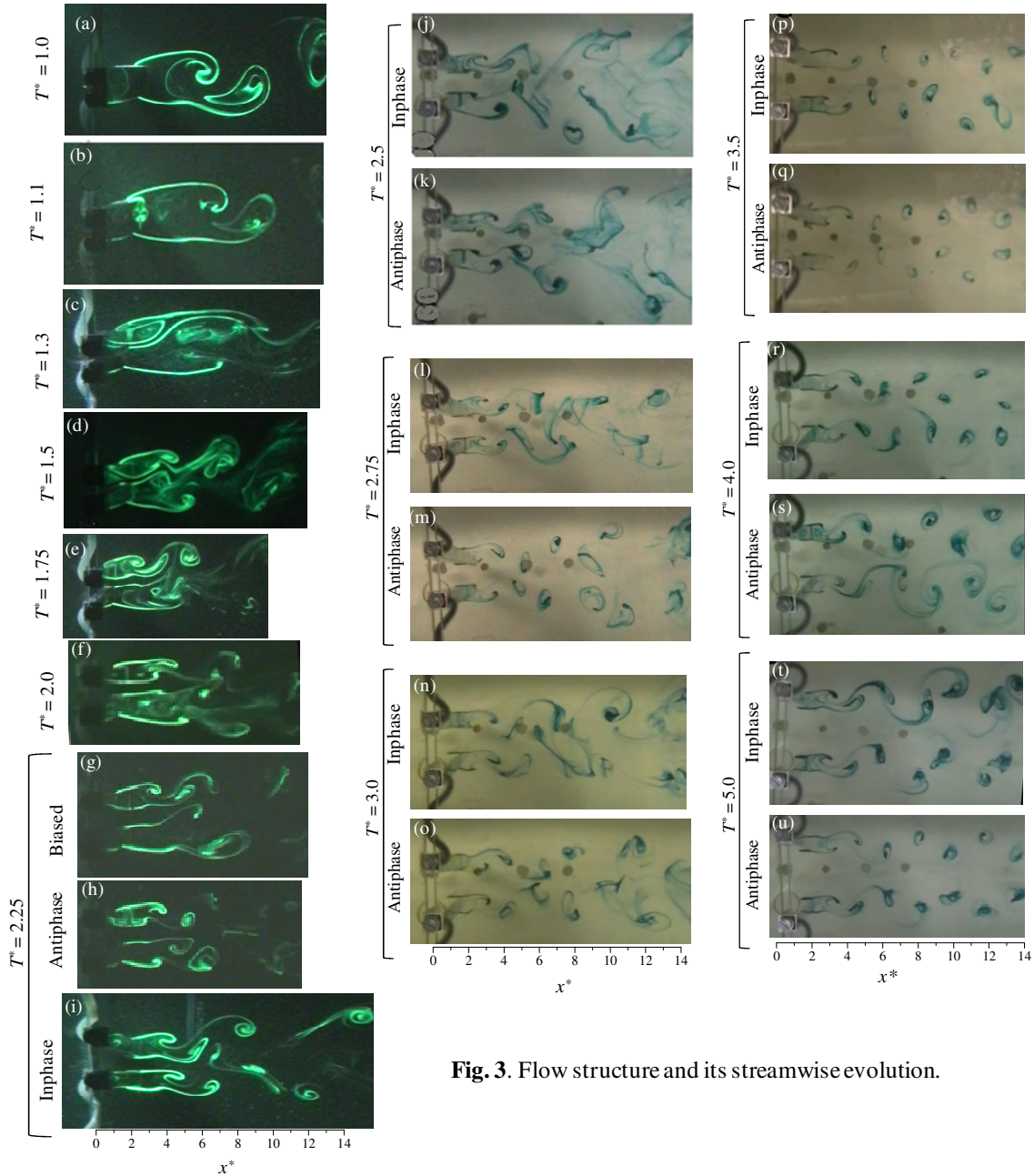


Fig. 3. Flow structure and its streamwise evolution.

At $2.1 < T^* < 2.4$, four distinct flow structures are identified, viz., with the gap flow biased downward (Fig. 3g), biased upward (not shown) and unbiased that may form antiphased and inphased vortex streets (Fig. 3h-i), respectively. Furthermore, they may switch from one to another. While the inphased or antiphased vortex shedding occurs only for a few cycles, the biased gap flow comes into view mostly with a switch of the gap flow in every cycle. At $T^* = 2.4 \sim 3.25$, both inphased and antiphased flow structures are observed (Fig. 3j-o). Two symmetric or anti-symmetric streets (four rows of vortices) may merge into one single street (two rows of vortices) in the downstream. The observation implies that the four rows of vortices are not yet stable at this T^* range, probably because of appreciable interactions between vortices, especially between the two inner rows. It is noted that x_c^* increases for larger T^* . In other words, the stability of the streets is enhanced at large T^* . This is reasonable in view of the weakened interaction between the streets at larger T^* . Another notable feature is that the antiphased streets are stable for a longer x_c^* than the inphased. For example, the two inphased streets at $T^* =$

2.5, 2.75, and 3.0 persist up to $x_c^* = 6.23, 8.0, \text{ and } 11.2$, respectively, but the antiphased only up to $x_c^* = 9.13, 10.5, 12.6$, respectively (see Fig. 3j-o). These x_c^* values have been estimated based on an average of more than 20 flow images for each T^* . With a further increase in T^* up to 5.0, inphased or antiphased shedding occurs and persists for the entire x^* range of the image. That is, the two streets are stable at least up to $x^* = 14$. Figure 4 shows how x_c^* varies with T^* . It is noted that x_c^* increases rapidly with T^* for $T^* > 2.2$, where the two streets are initially either inphased or antiphased, but slowly for $T^* < 2.2$, where the narrow and wide streets are generated. The inflection point occurs at $T^* = 2.2$ that nestles in the transition regime. An inflection point is mathematically a point where curvature changes from positive to negative or vice versa. In other words, the variation of x_c^* with T^* follows a third order polynomial, viz.

$$x_c^* = -38.18 + 59.50T^* - 26.82T^{*2} + 4.21T^{*3}, \quad (T^* > 1.2). \quad (1)$$

Eq. (1) is obtained by curve fitting to the data in Fig 4. The inflection point of Eq. (1) occurs at $T^* = 2.15$, which is very close to $T^* = 2.2$ observed physically.

The results and discussion presented above lead to the classification of flow into four regimes: (i) the single bluff body regime ($T^* < 1.2$) where flow through the gap is feeble to split the wake into two streets, (ii) the asymmetric wake regime ($1.2 < T^* < 2.1$) where the gap flow splits the wake into one narrow and one wide street, (iii) the transition regime ($2.1 < T^* < 2.4$) where both the asymmetric wake and the coupled streets in an inphase or antiphase mode occur, and (iv) the coupled-street regime ($T^* > 2.4$) where the streets are inphase- or antiphase-coupled. The inflection point at $T^* = 2.2$ in the transition regime separates the asymmetric wake and the coupled-street regimes.

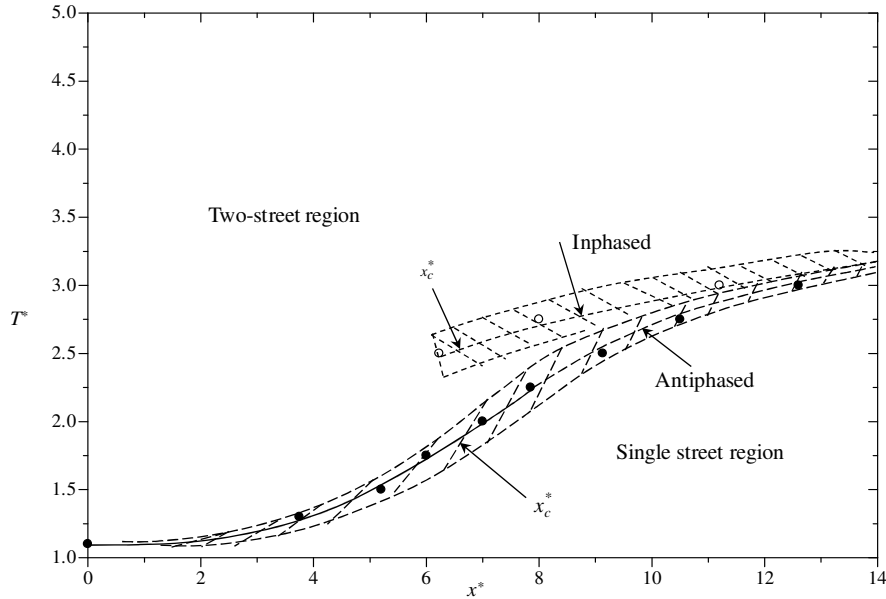


Fig. 4. Dependence of the critical x_c^* on T^* , at which the two streets merge into one.

3.2. Mechanism of the gap flow bias

The gap flow separates from the inner side of the cylinders and rolls up to form two counter-rotating vortices E and F , respectively (Fig. 5a). Assume the two cylinders are symmetrically arranged with respect to approaching flow in the working section. Vortices E and F should go to the upper and lower streets, respectively. That does not happen of course. Both vortices behave like a conjoined twin and tend to move together. Why? Since the two vortices shed from the gap, the initial lateral distance between them depends on T^* . The larger the T^* , the greater is the lateral spacing between them. At sufficiently small T^* , the two opposite-signed vortices (Fig. 5b) are adequately close, and the flow between them accelerates because of the same-signed velocities, resulting in a low pressure region between. As such, the two vortices attract each other when advected and tend to move together. The low pressure between them is a tie between the conjoined twin. Couder and Basdevant [6] examined experimentally and numerically the convective behaviors of two coupled vortices of opposite sign and

two of the same sign. They found that the coupled vortices of opposite sign moved faster than those of the same sign. Furthermore, the flow velocity across the gap is highest at the centerline, which also contributes to the low pressure between the gap vortices. Presumably, both streets have the same pressure, then the direction the twin move is crucial. As sketched in Fig. 5(b), their resultant direction will be that of the velocity at their interface, which is dependent on the phase difference between the vortices. The resultant direction will be inclined downward if E leads F , and upward if E lags F . The leading and lagging may happen naturally or may be governed by the pressure difference between the streets.

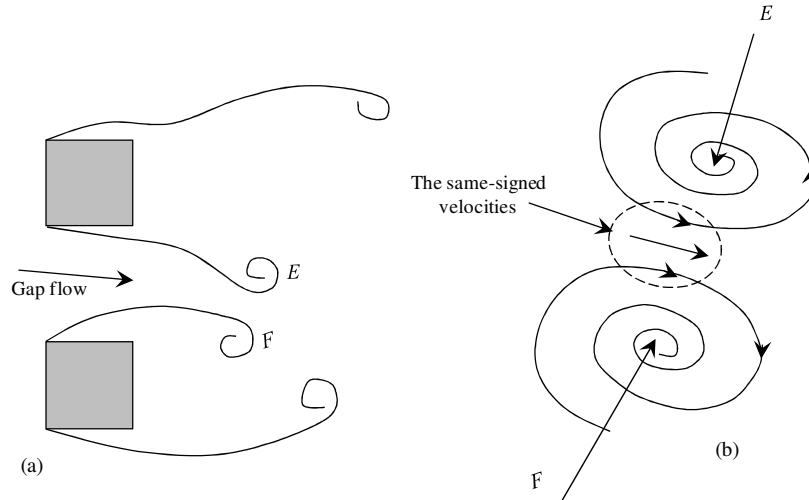


Fig. 5. (a) Counter-rotating gap vortices. (b) Generation of larger velocities and lower pressure between two counter-rotating vortices.

3.3. Evolution of two streets into one

The merge of the wide and narrow streets into one has been shown in Fig. 3(a-f). It is of great interest to understand how two inphase- or antiphase-coupled streets evolve to a single street. Figure 6 shows typical sequential photographs and corresponding sketches to illustrate the process. The real time index (minute : second : frame-number) is shown on the upper left corner of each plate. Two separate streets are initially generated, each consisting of two rows of vortices. As the vortices are advected downstream, the upper inner vortex E trips to the lower street and comes close to F (Fig. 6b). It has been discussed earlier that the two vortices separated from the gap tend to stay together because of the low pressure region between them. Vortex E , which leads F , wanders toward the lower street. Once coming close, they accelerate and their speeds increase, catching up with vortex G . With the same sense of rotation, E and G merge first and keep F in abreast (Fig. 6c). Eventually, E , F and G amalgamate, forming a big anti-clockwise vortex. This vortex and clockwise vortex D in the initial upper street form a stable single street.

4. Conclusions

A detailed study has been conducted of the flow structure, gap flow switch and stability in the wake of two side-by-side square cylinders at $Re = 300$ based on flow visualization data. The examined T^* is from 1.0 to 5.0.

Four flow regimes are identified, namely (i) single bluff body regime ($T^* < 1.2$) where the gap flow momentum is feeble to split the wake into two streets, (ii) asymmetric wake regime ($1.2 < T^* < 2.1$) where the gap flow having sufficient momentum splits the wake into one narrow and one wide street, (iii) transition regime ($2.1 < T^* < 2.4$) where both the asymmetric wake and the coupled streets in an inphase or antiphase mode presist, and (iv) coupled-street regime ($T^* > 2.4$) where the two streets are inphase- or antiphase-coupled.

One explanation is provided on why the flow through the gap is biased in the asymmetric wake regime, forming the narrow and wide streets. The two oppositely signed gap vortices behave like a conjoined twin and tend to move together. A low pressure region is generated due to the same signed and hence larger velocities between the vortices, which acts to maintain the two vortices together and even closer during their advection. The phase lag between the gap vortices holds the key for the destination street the two gap vortices will join. The two

streets always merge to one at x_c^* , which depends on T^* , viz.

$$x_c^* = -38.18 + 59.50T^* - 26.82T^{*2} + 4.21T^{*3} \quad (T^* > 1.2).$$

The inflection point of this curve occurs at $T^* = 2.2$, which separates the asymmetric wake and the coupled-street regime.

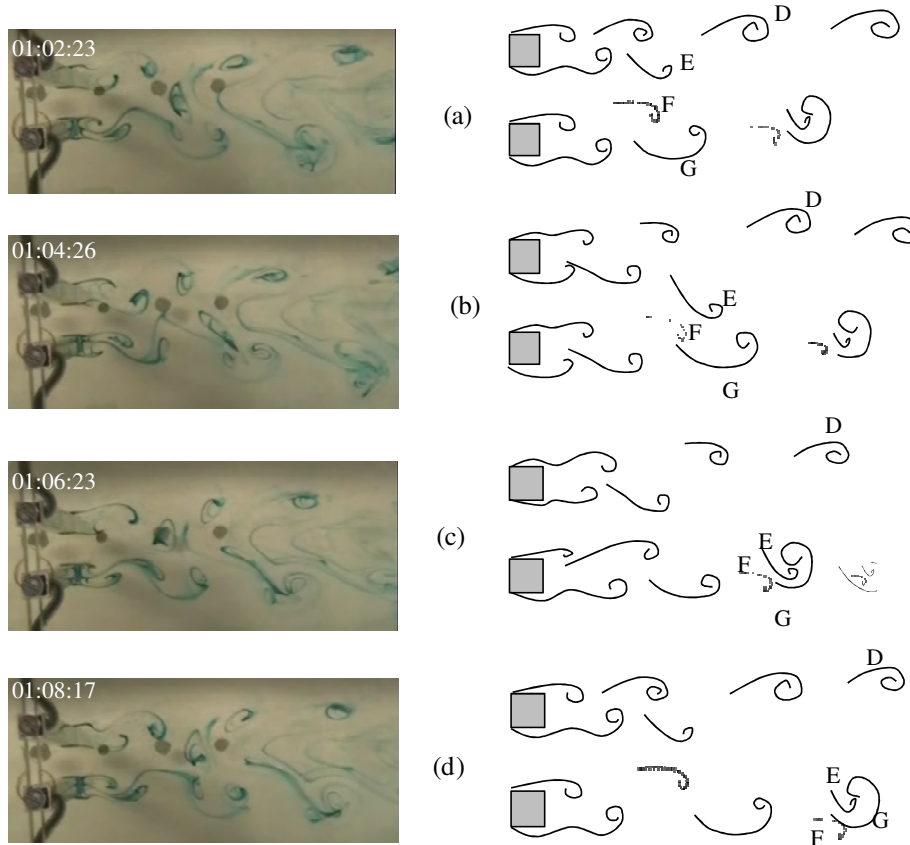


Fig. 6. Photographs and sketches showing the merge of two coupled streets into one. $T^* = 2.75$.

5. Acknowledgement

Alam wishes to acknowledge supports given to him from Shenzhen Government through grant CB24405004 and from China Govt through ‘1000-young-talent-program’.

6. References

- [1] M. Kiya, M. Arie, and H. Mori, “Vortex Shedding from Two Circular cylinders in Staggered Arrangement”, *ASME Journal of Fluids Engineering*, Vol. 102, 166-173, 1980.
- [2] M.M. Alam, Y. Zhou, and X.W. Wang, “The Wake of Two Side-by-Side Square Cylinders”, *Journal of Fluid Mechanics*, Vol. 669, 432-471, 2011.
- [3] H. Sakamoto, and H. Haniu, “Effect of Free Stream Turbulence on Characteristics of Fluctuating Forces Acting on Two Square Prisms in Tandem Arrangement,” *ASME Journal of Fluids Engineering*, Vol. 110, 140-146, 1988.
- [4] V. Kolář, D.A. Lyn, and W. Rodi, “Ensemble-Averaged Measurements in the Turbulent Near Wake of Two Side-by-Side Square Cylinders,” *Journal of Fluid Mechanics*, Vol. 346, 201-237, 1997.
- [5] A. Agarwal, L. Djenidi, and R.A. Antonia, “Investigation of Flow Around a Pair of Side-by-Side Square Cylinders using the Lattice Boltzmann Method,” *Computer and Fluids*, Vol. 35, 1093-1107, 2006.
- [6] Y. Couder, and C.B. Basdevant, C. B., “Experimental and Numerical Study of Vortex Couples in Two-Dimensional Flows,” *Journal of Fluid Mechanics*, Vol. 173, 225-251, 1986.

Reduction of Fuel Consumption of a Car by Aerodynamic Drag Reduction

Mohammad Mashud¹, Abdullah Al Bari¹ and Md. Shahadot Hoshen¹

¹Department of Mechanical Engineering

¹Khulna University of Engineering & Technology,

Khulna-9203, Bangladesh

E-mail: shahadot_hoshen@yahoo.com

Abstract

One of the main causes of aerodynamic drag for sedan vehicles is the separation of flow near the vehicle's rear end. To delay flow separation, bump-shaped vortex generators are tested on for application to the roof end of a sedan. Commonly used on aircraft to prevent flow separation, vortex generators themselves create drag, but they also reduce drag by preventing flow separation at downstream. The overall effect of vortex generators can be calculated by totaling the positive and negative effects. Since this effect depends on the shape and size of vortex generators, those on the vehicle roof are optimized. This paper presents the optimization result for reduction of aerodynamics drag as well as fuel consumption reduction by showing the effect of vortex generators in the flow field and the mechanism by which these effects take place.

Key words: Body, Aerodynamics, Aerodynamic Devices, Flow Visualization, Computational Fluid Dynamics (CFD)

1. Introduction

To save energy and to protect the global environment, fuel consumption reduction is primary concern of automotive development (i.e. vehicle body development). Reduction of drag is essential for improving fuel consumption and driving performance, and if an aero- dynamically refined body is also aesthetically attractive, it will contribute much to increase the vehicle's appeal to potential customers. However, as the passenger car must have enough capacity to accommodate passengers and baggage in addition to minimum necessary space for its engine and other components, it is extremely difficult to realize an aerodynamically ideal body shape. The car is, therefore, obliged to have a body shape that is rather aero- dynamically bluff, not an ideal streamline shape as seen on fish and birds. Such a body shape is inevitably accompanied by flow separation at the rear end. The passenger car body's aerodynamic bluntness, when expressed by the drag coefficient (CD), is generally between 0.2 and 0.5, while that of more bluff cubic objects is greater than 1.0 and that of the least bluff bullets is less than 0.1. Two elements that have major influence on the drag coefficient of a bluff object are the roundness of its front corners and the degree of taper at its rear end. The importance of the influence of the rear taper in passenger cars can be described as follows: Fig. 1 schematically shows the flow around a sedan. Because of the presence of a trunk at the rear, the flow separates at the roof end and then spreads downward. As a result, the flow around the car is similar to that around a streamline-shaped object with a taper at the rear. For this reason, a sedan with a trunk tends to have smaller drag coefficient value than a wagon-type car. For example, a reduction of the aerodynamic drag coefficient from 0.60 to 0.30 would lead to a decrease of fuel consumption of approximately 30%. [5]

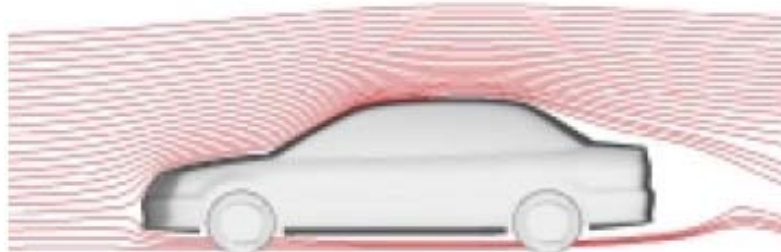


FIG. 1. Flow around a sedan

In other words, taper at the rear has the effect of delaying flow separation (or shifting the flow separation point downstream). A well-known example for intensifying the flow separation delaying effect is utilizing a dimple (like the ones on golf balls)(1). Adding dimple-shaped pieces can lower the CD to a fraction of its original value. This is because dimples cause a change in the critical Reynolds numbers (the Reynolds number at which a transition from laminar to turbulent flow begins in the boundary layer).

2. Mechanism of flow separation and objectives of adding vortex generators

Fig. 2 shows a schematic of flow velocity profile on the vehicle's centerline plane near the roof end. Since

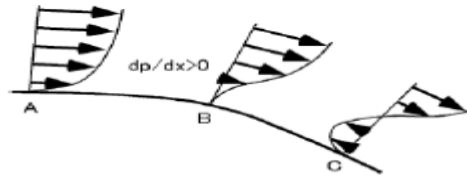


Fig.2. Schematics of velocity profile around rear end

purpose of using VGs is to control flow separation at the roof end of a sedan, it is so similar to the purpose of using VGs on aircraft. To determine the shape of sedan VGs, the data on aircraft VGs are referred to(2) the vehicle height in this section becomes progressively lower as the flow moves downstream, an expanded airflow is formed there. This causes the downstream pressure to rise, which in turn creates reverse force acting against the main flow and generates reverse flow at downstream Point C. No reverse flow occurs at Point A located further upstream of Point C because the momentum of the boundary layer is prevailing over the pressure gradient (dp/dx). Between Points A and C, there is separation Point B, where the pressure gradient and the momentum of the boundary layer are balanced. As shown in Fig. 2, in the lower zone close to the vehicle's surface within the boundary layer, the airflow quickly loses momentum as it moves downstream due to the viscosity of air. The purpose of adding VGs is to supply the momentum from higher region where has large momentum to lower region where has small momentum by stream wise vortices generated from VGs located just before the separation point, as shown in Fig. 3. This allows the separation point to shift further downstream. Shifting the separation point downstream enables the expanded airflow to persist proportionately longer, the flow velocity at the separation point to become slower, and consequently the static pressure to become higher. The static pressure at the separation point governs over all pressures in the entire flow separation region. It works to reduce drag by increasing the back pressure. Shifting the separation point downstream, therefore, provides dual advantages in drag reduction:-one is to narrow the separation region in which low pressure constitutes the cause of drag; another is to raise the pressure of the flow separation region. A combination of these two effects reduces the drag acting on the vehicle. However, the VGs that are installed for generating streamwise vortices bring drag by itself. The actual effectiveness of installing VGs is therefore deduced by subtracting the amount of drag by itself from the amount of drag reduction that is yielded by shifting the separation point downstream.

Larger-sized VGs increase both the effect of delaying the flow separation and the drag by itself. The effect of delaying the flow separation point, however, saturates at a certain level, which suggests that there must be an optimum size for VGs.

3. Experimental methods

Evaluation of the effectiveness of VGs and optimization were conducted using subsonic wind tunnel. The test section was closed and the main flow velocity was set at 5 m/s. Mitsubishi LANCER EVOLUTION VIII model car was used as the test vehicle. To evaluate the effectiveness of VGs, six component forces of the vehicle were measured and VGs' optimum shape and size were examined. Furthermore, in order to clarify the factors contributing to the effect provided by VGs, the total pressure distribution of the wake flow was measured with pitot rake, the velocity distribution was measured by the particle image velocimetry (PIV) method and the flow field was analyzed in detail using computational fluid dynamics (CFD).

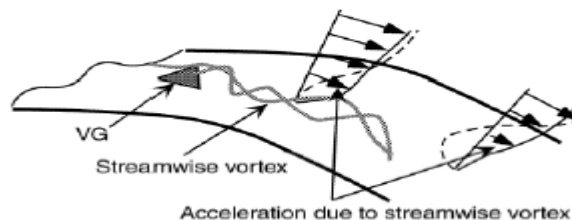


Fig. 3. Schematics of flow around vortex generator

4. Finding the optimum VG's

To select appropriate shape and size of the VG which generates streamwise vortex the most efficiently (with the least drag by itself) is important to achieve objectives.

In connection with the size, the thickness of the boundary layer is measured based on the assumption that the optimum height of the VG would be nearly equal to the boundary layer thickness. Fig. 4 shows the velocity profile on the sedan's roof. From this figure, the boundary layer thickness at the roof end immediately in front of the separation point is about 30 mm. Consequently, the optimum height for the VG is estimated to be up to approximately 30 mm. As to the shape, a bump-shaped piece with a rear slope angle of 25 to 30° is selected. This is based on the fact that a strong streamwise vortex is generated on a hatchback-type car with such rear window angle(4). A half-span delta wing shape is also recommended for the VG. This shape is inferred from an aircraft's delta wing that generates a strong streamwise vortex at its leading edge(2).

As to the location of VGs, a point immediately upstream of the flow separation point was assumed to be optimum, and a point 100 mm in front of the roof end was selected as shown in Fig. 5. The effects of bump-shaped VGs mounted at this point are presented in Fig.6. The front half contour of the bump-shaped VG was smoothly curved to minimize drag and its rear half was cut in a straight line to an angle of approximately 27° for maximum generation of a streamwise vortex. As shown in Fig. 6, three bump-shaped VGs that were similar in shape but different in height (15 mm, 20 mm, and 25 mm) are examined. The graph in Fig. 6 shows that the drag coefficient was smallest at the height of 20 to 25 mm, so a height in this range was considered optimum for the VG. However, a taller VG might cause a

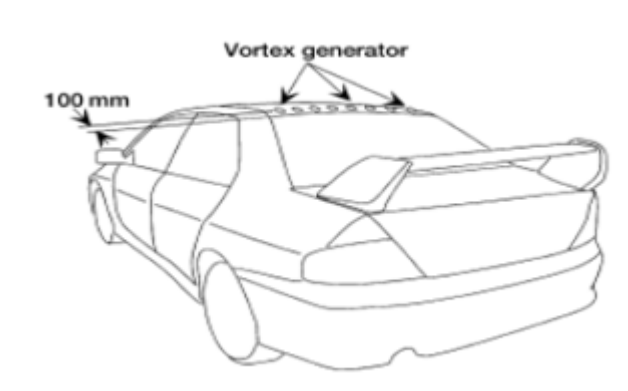
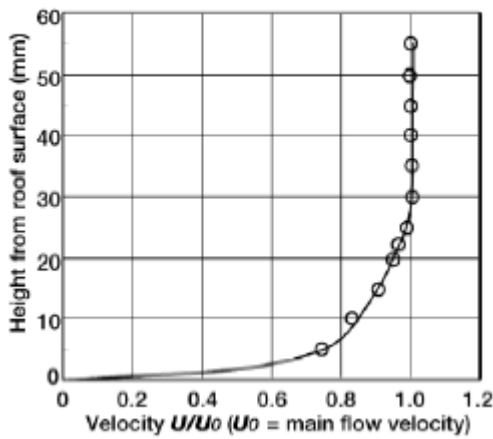


Fig. 4. Velocity profile on roof (100 mm upstream from rear end)

Fig. 5. Location of vortex generators

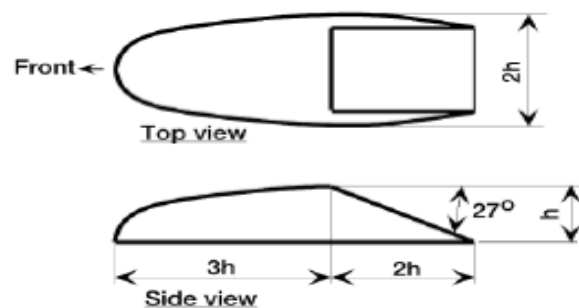
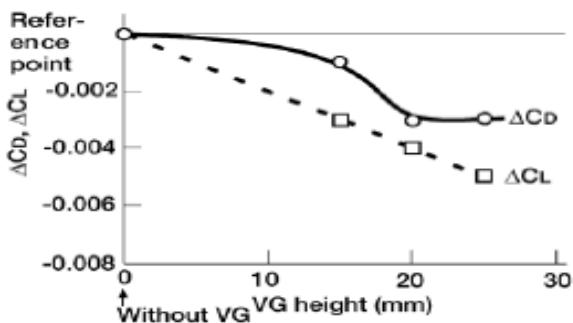


Fig. 6. Effects of bump-shaped vortex generators

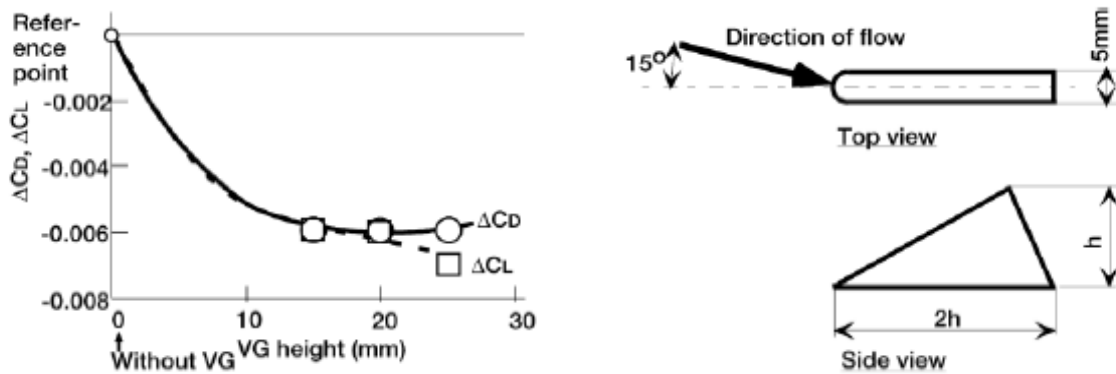


Fig. 7. Effects of delta-wing-shaped vortex generators

decrease in the lift. The rather small change in drag coefficient resulting from change in height can be accounted for as follows. As mentioned before, an increase in height of the VG simultaneously causes two effects: one is reduced drag resulting from delayed flow separation and the other is increased drag by the VG itself. These two effects are balanced when the VG's height is between 20 and 25 mm. From these results, a reduction of C_D is 0.003 with this bump-shaped VG when the shape and size are optimized. The effectiveness of the delta-wing-shaped VG is also examined. The recommended shape of the delta-wing-shaped VG is defined by the following (2): Length/height = 2, Yaw angle = 15°, Interval/height = 6. Based on this data, delta-wing-shaped VGs are created with the following specifications:

Length/height = 2, Height = 15 mm, 20 mm and 25 mm (three types) Thickness = 5 mm

The delta-wing-shaped VGs should be installed at a yaw angle of 15° to the airflow direction. In order to meet this condition, the direction of airflow at the roof end was investigated by oil flow measurement. Airflow direction was found to be different between sideways positions on the roof. The airflow is aligned directly with the backward direction at center of a car, but it increasingly deviates toward the center as the measurement point shifts away from the central position. For this reason, the delta-wing-shaped VGs must be installed at an angle of 15° against the vehicle center-line for the central position, whereas they must be installed at an angle near 0° for outermost positions. The results of these tests are shown in Fig. 7. Delta-wing-shaped VGs were found to be less sensitive to change in height than bump-shaped VGs; the drag reduction effects for the VGs of three different heights

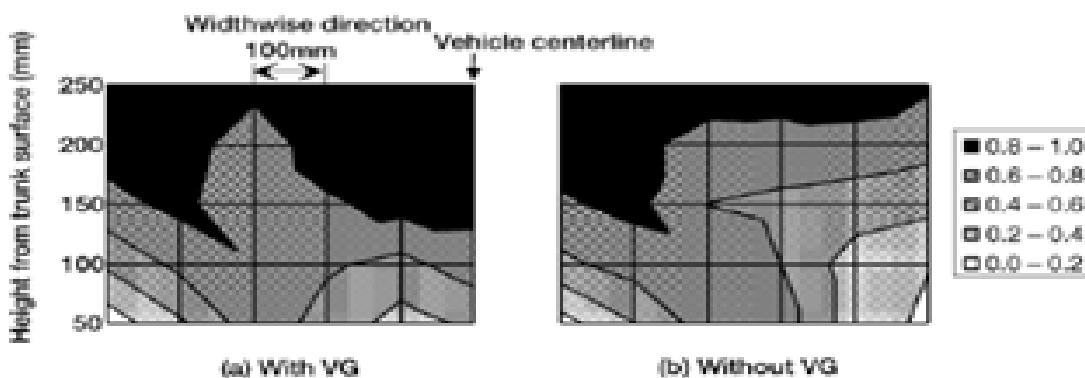


Fig. 8 Total pressure distribution (upstream of rear spoiler)

Fig. 8. Total pressure distribution (upstream of rear spoiler)

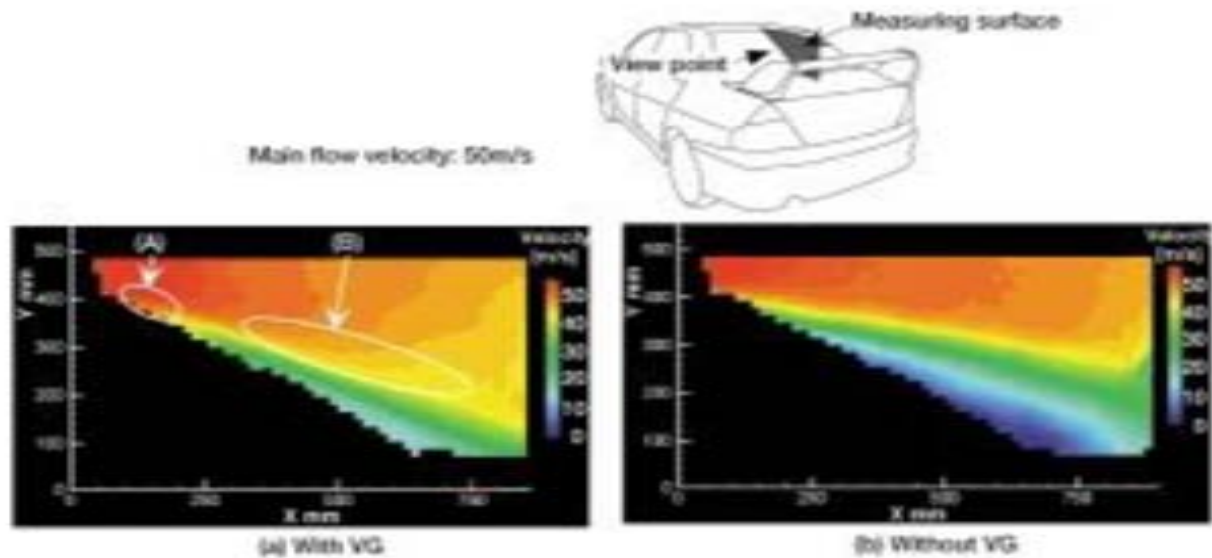


Fig. 9. Velocity distribution by PIV measurement

(15 mm, 20 mm and 25 mm) were all equivalent to -0.006 . The effect of lift reduction increased only slightly with the height. The drag reduction also differed only slightly with changes in the number of VGs and their positions. The number and positions of the tested VGs seems to be in their optimum ranges. From these results, delta-wing-shaped VGs were capable of reducing drag by -0.006 . The reason for why delta-wing-shaped VGs are more effective than bump-shaped VGs can be explained as follows: Delta-wing-shaped VGs have a smaller frontal projection area, which means that they themselves create smaller drag. Moreover, the vortex generated at the edge of a delta-wing-shaped VG keeps its strength in the flow downstream of the edge since it barely interferes with the VG itself because of the VG's platform. With bump-shaped VGs, on the other hand, the vortex is generated at a point close to the downstream edge of the bump, which causes the vortex to interfere with the bump and lose its strength.

5. Verification of VG's mechanism

In Section 2 above, the effect of VGs is estimated that the separation point is shifted to downstream, which in turn narrows the flow separation region. The flow field was thus investigated in order to verify the correctness of this estimation. Fig. 8 shows total pressure distribution in the wake flow immediately upstream of the rear spoiler for both cases with and without VGs. High total pressure regions correspond to high velocity regions. As the figure shows, the high velocity region is expanded downward by addition of VGs, signifying that the flow separation region is narrowed. Fig. 9 shows the results of velocity distribution using the PIV method. The PIV laser light sheet was illuminated from above on the center plane of the vehicle body and the measuring surface was photographed from the side (as indicated by the viewpoint arrow in Fig. 9) to calculate the two-dimensional velocity distribution. Fig.9 (a) shows the velocity distribution for the case with VGs, and Fig. 9 (b) shows the velocity distribution for the case without VGs. As evident from the figure, the case with VGs shows an increase in velocity on the surface of the body (rear window) just behind the VG (Zone A in the figure) and extension of the high velocity zone downward (Zone B in the figure). This supports our estimation in the previous section that VGs cause air-flows above the rear window to attach to the surfaces of the body.

This phenomenon was examined in detail using CFD analysis. Star-CD was used as the solver and RNG $k-\epsilon$ model as the turbulence model in this analysis. In order to detect flow separation at the rear window, a prism cell was inserted in the vicinity of the vehicle, and the "y+" value of computational grid is arranged to become an appropriate value between 20 and 50 near the separation point. Fig. 10 shows the calculation results for the case with VGs and the case without VGs. These results show good agreement with the experimental results using the PIV method, and clearly show that the

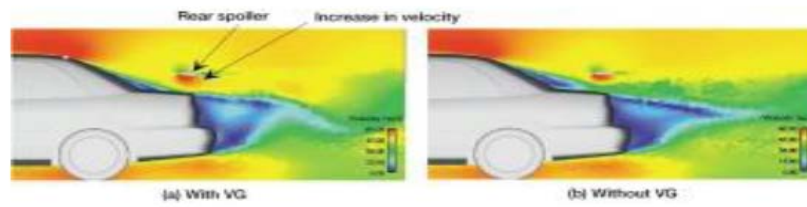


Fig. 10. Velocity Distribution by CFD

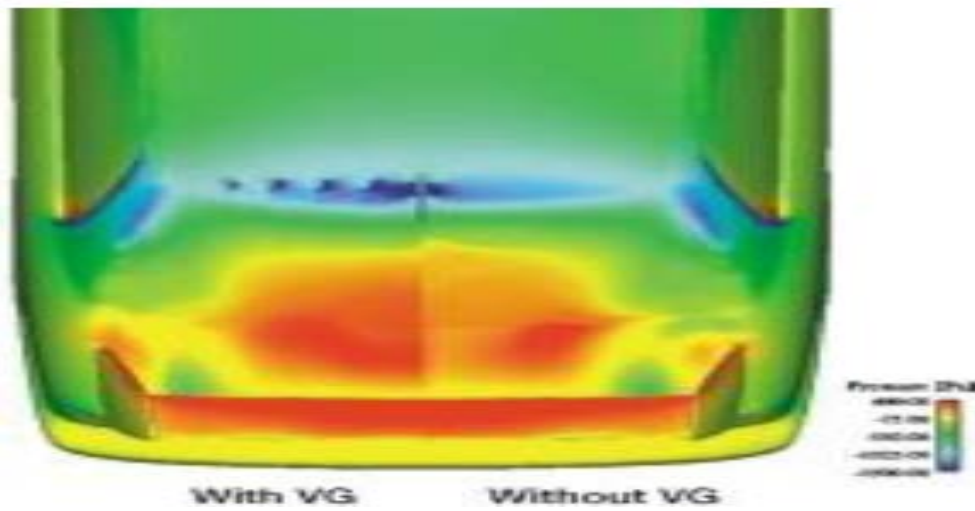


Fig. 11. Pressure Distribution of Vehicle (CFD) LOW VELOCITY REGION IS NARROWED BY THE ADDITION OF VGs. THE CHANGES IN DRAG AND LIFT CALCULATED BY CFD SHOWN BELOW ARE ALMOST AGREE WITH THE EXPERIMENTAL RESULTS (FIG. 7). $\Delta CD = -0.004$ $\Delta CL = -0.013$

The CFD calculation, therefore, could simulate the actual phenomenon. CFD results in Fig. 10 also show that the velocity of the airflow along the bottom surface of the rear spoiler increases by addition of VGs, which reveals that a decrease in lift (an increase in down-force) did occur. These results also show that the flow separation region (low velocity region) at the rear portion of the trunk is slightly narrowed. Fig. 11 shows the pressure distribution on the vehicle body surface. The addition of VGs gives the effect of increasing the surface pressure over a wide area ranging from the rear window to the trunk and this in turn reduces the drag. However, negative pressure region around the VGs indicate that VGs themselves cause drag. Such changes in airflow can be attributed to VGs that work to suppress flow separation at the rear window. To verify this mechanism, the airflow was studied in further detail. Fig. 12 shows vorticity distribution behind the VGs. Streamwise vortices are generated behind the VGs. Our estimation that the streamwise vortex causes

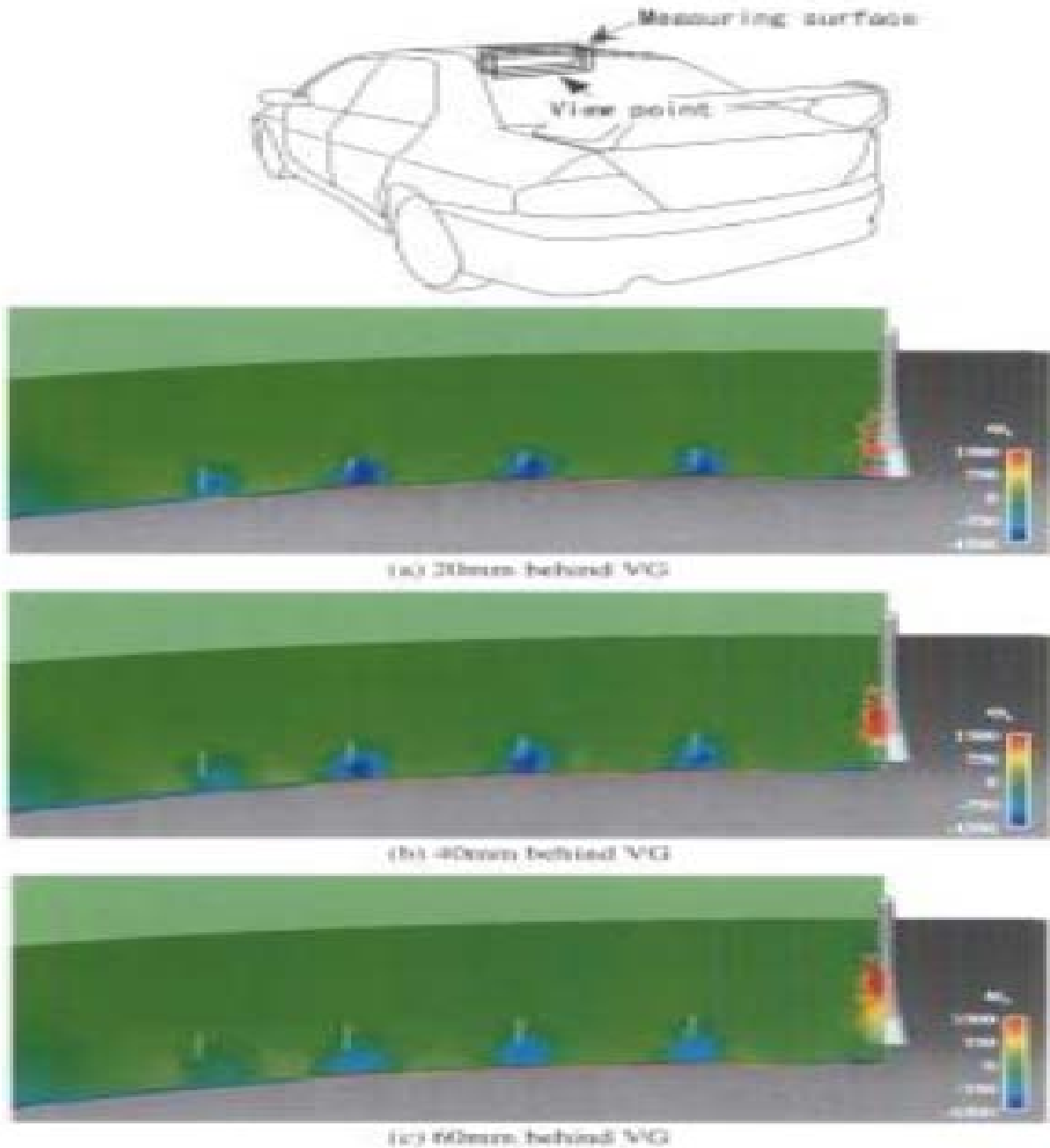


Fig. 12. Vorticity distribution behind vortex generators (CFD)

the separation point to shift downstream is confirmed by CFD results. Fig. 13 shows close-up views of the flow field near the separation point. The case with VGs shows flow separation occurring further downstream than in the case without VGs.

6. Conclusions

The conclusions of this research can be summarized into the following points:

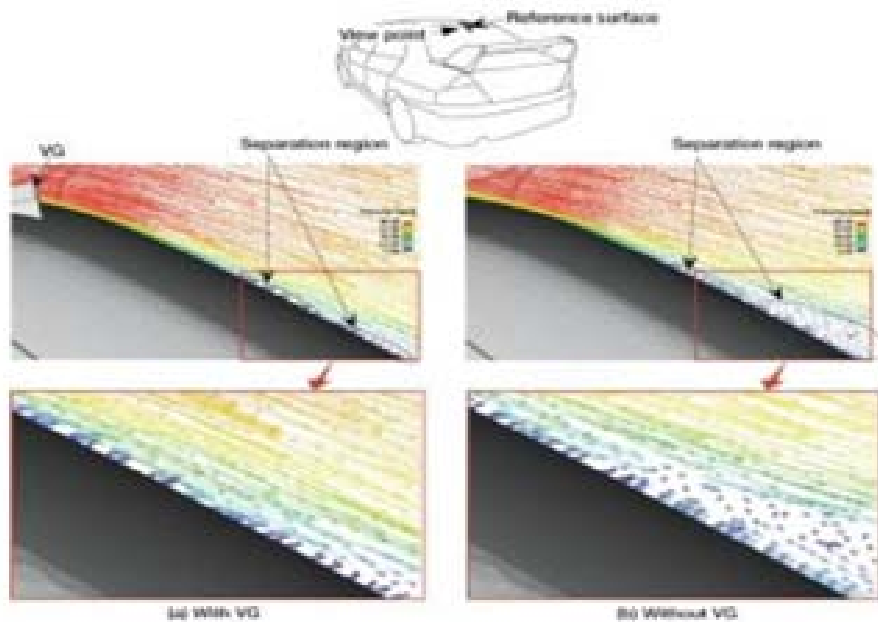


Fig. 13. Velocity vectors around separation point (CFD)

(1) Vortex generators (VGs) were studied to install immediately upstream of the flow separation point in order to control separation of airflow above the sedan's rear window and improve the aerodynamic characteristics. It was found that the optimum height of the VGs is almost equivalent to the thickness of the boundary layer (15 to 25 mm) and the optimum method of placement is to arrange them in a row in the lateral direction 100 mm upstream of the roof end at intervals of 100 mm. The VGs are not highly sensitive to these parameters and their optimum value ranges are wide. Better effects are obtained from delta-wing-shaped VGs than from bump-shaped VGs. By controlling separation of airflow above the sedan's rear window and improving the aerodynamic characteristics, aerodynamics drag will reduce that the same time fuel consumption will reduce.

(2) Application of the VGs of the optimum shape determined through the abovementioned analyses to the Mitsubishi LANCER EVOLUTION showed a 0.006 reduction in both the drag coefficient and lift coefficient.

(3) Factors contributing to the effect of VGs were verified by conducting measurement of total pressure, velocity distribution and CFD. As a result of the verifications, it is confirmed that VGs create streamwise vortices, the vortices mix higher and lower layers of boundary layer and the mixture causes the flow separation point to shift downstream, consequently separation region is narrowed. From this, we could predict that VGs cause the pressure of the vehicle's entire rear surface to increase therefore decreasing drag, also the velocity around the rear spoiler to increase, and the lift to decrease. The delta-wing-shaped VG, which demonstrated high effectiveness in this research, is planned for commercialization as an accessory for sedans after slight modifications to the shape with respect to design, legal conformance and practicality.

7. References

- [1] Hoerner, S. F., Fluid-dynamic Drag, Published by the author, 1958
- [2] Hoerner, S. F., Fluid-dynamic Lift, Published by the author, 1985
- [3] Shibata, H., MMC's Vehicle Wind Tunnel, Automobile Research Review (JARI) Vol. 5, No. 9, 1983
- [4] Hucho, W.H., Aerodynamics of Road Vehicles, Fourth Edition, SAE International 1998
- [5] Hamsten, B., Stangl, G., Uttenthaler, J., Neuentwicklungen bei Omnibussen von MAN und Neoplan, Automobil-Technische Zeitschrift, ATZ 9/2002, Jahrgang 104, 2002.
- [6] Kopp, S., Schönberg, S., Koos, H., Design und Aerodynamik bei Nutzfahrzeugen, Automobil-Technische Zeitschrift, ATZ 07-08/2009, Jahrgang 111, 2009.

Analysis of Flow in Complex Pipe System

Abdul Mohaimen Safi

Department of Mechanical Engineering, BUET, Dhaka- 1000, Bangladesh

E-mail: mohaimensafi@gmail.com

Abstract

In hydraulic engineering the analysis of water flow through a closed, pressurized piping system is a common task. This paper presents an analysis of flow in complex pipe system using finite element method. A computer model has been developed. The plot of velocity profile within the pipe and the graph of variation of velocity of the outlet pipe have been studied. This model is good opportunity to study variety of practical design situations including farm irrigation pipe networks and municipal water systems. This model is flexible in its ability to handle different design problems including branched and multi-looped complex pipe networks.

Keywords: hydraulic engineering, complex pipe system, finite element method.

1. Introduction

Pipe network analysis is a calculation of fluid flows and pressure drops in complex piping systems. Analysis of piping systems is important for public utilities supplying water to consumers, natural gas distribution planning, or any system of piping where consistent delivery pressures and flow rates are important. The efficiency of the system to minimize the losses in a network is as important as saving money these days. The researchers all over the world are working hard to find a solution to minimize these head losses (energy), total length of the network and pipe diameters. When a real fluid flows through a pipe, a part of its energy is converted into thermal energy due to internal friction and turbulence. This leads to the expression of energy loss in terms of the fluid height known as head loss [1]. Head losses are divided into two main categories, “major losses” associated with per length of the pipe and “minor losses” associated with minor appurtenance and accessories like bend, fittings, valves etc. These accessories cause change in magnitude, direction and distribution of the flow. For relatively short pipe systems, with a relatively large number of accessories like bends and fittings, minor losses can easily exceed major losses. Pipe network analysis uses iterative method regardless of the fluid being delivered. The importance and complexity of these calculations increases as a pipe network grows, and customers expect uninterrupted delivery [2]. Velocity and pressure drops can be measured experimentally, but laboratory measurements do not always translate well to real-world systems of overlapping loops, many delivery points and a constantly changing pipe network. Analytical solution for every problem is not possible for complex shape and boundary condition. Hence, numerical method had become popular with the researcher in the last few decades. Analysis of flow in a complex pipe system requires solution of partial differential equations. In this present paper for the solution of these partial differential equations Finite Element Method (FEM) has used. A finite element model of a problem gives a piece wise approximation to the governing equations. Since these elements can be put together in a variety of ways, they can be used to represent exceedingly complex shapes. In the present paper numerical simulation for flow in a complex pipe system has been investigated using ANSYS one of the most popular finite element method software.

2. Description of the problem

The geometry of the problem is shown in Fig 1. A two dimensional analysis has been performed assuming the fluid to be incompressible, and constant property of fluid throughout the pipe. In all the simulation water of density $\rho = 1000 \text{ kg/m}^3$ and viscosity $\mu = 1 \text{ kg/m-s}$ at a reference temperature of 25°C have been taken. Uniform velocity distribution is assumed for the inlets shown in Fig 1. A stationary no-slip boundary condition is imposed on the walls of the pipe system. At outlet pressure outlet boundary condition is used and diffusion fluxes for the variables in the exit direction are set to zero.

3. Governing equations

The details of the governing equations and the treatment of the interface are obtained from ANSYS user guide [3].

Continuity equation:

$$\frac{\partial(\rho)}{\partial t} + \nabla \cdot (\rho U) = \sum_q S_q \quad (1)$$

Where, ρ , U , t , S are density, velocity, time and mass source, respectively. In the present case S is zero.

Momentum equation:

The single momentum equation is solved in the computational domain and the resulting velocity field is shared amongst the phases. The general momentum equation can be written as:

$$\frac{\partial(\rho U)}{\partial t} + \nabla \cdot (\rho U \cdot U) = -\nabla P + \nabla \cdot [\mu(\nabla U + \nabla U^T)] + (\rho g) + F \quad (2)$$

Where P , g , F , μ are pressure in the flow field, acceleration due to gravity, body force acting on the system and viscosity of the flowing fluid respectively.

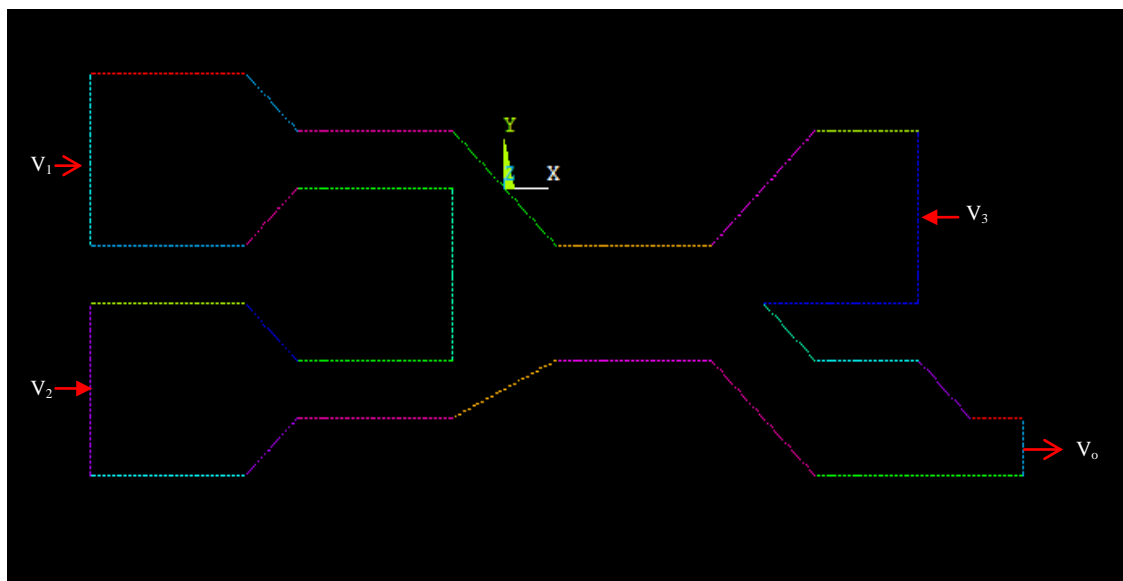


Fig. 1. Model geometry

4. Solution methodology

For the analysis FLOTRAN element FLUID141 has been used as FLUID141 efficiently handle transient or steady state fluid/thermal systems that involve fluid and/or non-fluid regions. The FLUID141 element has these characteristics: 1) Dimensions: 2-D, 2) Shape: Quadrilateral, four nodes or triangle, three nodes 3) Degrees of freedom: Fluid velocity, pressure, temperature, turbulent kinetic energy, turbulent energy dissipation, multiple species mass fractions for up to six fluids. The conservation equations for viscous fluid flow and energy are solved in the fluid region, while only the energy equation is solved in the non-fluid region. For the FLOTRAN CFD elements, the velocities are obtained from the conservation of momentum principle and the pressure is obtained from the conservation of mass principle. The temperature if required is obtained from the law of conservation of element discretization of the governing equation for each degree of freedom is solved separately [3]. The commonly used κ - ϵ turbulent model was applied in the simulation. This model is based on the concept that turbulence consists of small eddies which are continuously forming and dissipating. This model is numerically more robust than the Reynolds stress turbulent model in terms of convergence and stability. Even though the Reynolds numbers in the simulations are low however, it was thought that the flows are generally turbulent due to regular disturbances. The Ansys software package offers various mesh types. For this study the fine mesh option was used in order to obtain simulated results of high accuracy. The maximum grid length was

set to 0.0001m. The maximum number of iterations was set to 1000 and the target relative residual was set to 0.0001. The blend factor was specified to 2nd order. These settings were determined based on many trial simulations. Intel Core 2 Duo, 2.0 MHz processing machine has been used for the entire computation.

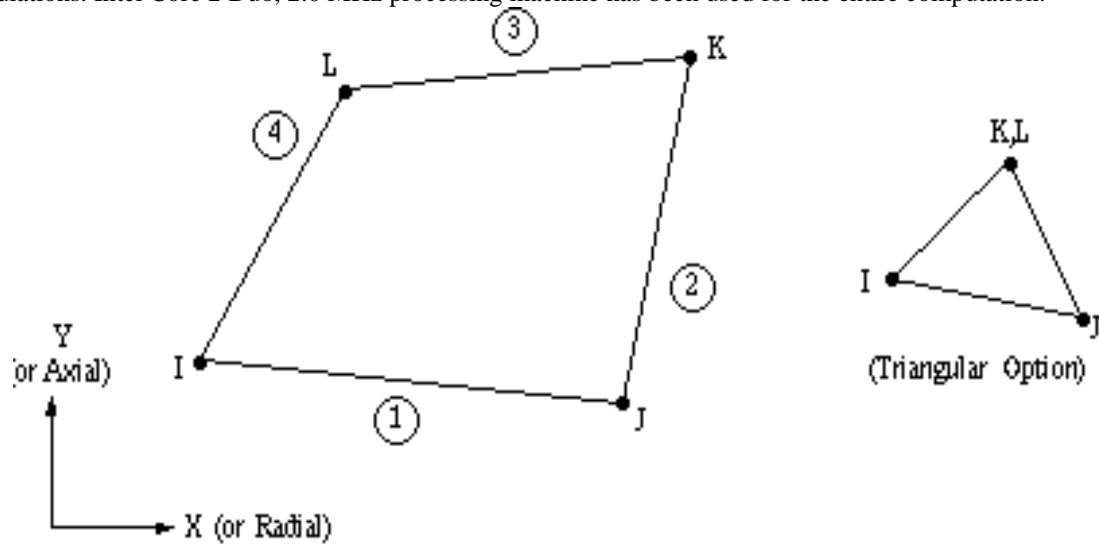


Fig. 2. FLOTRAN element FLUID141

5. Results and discussions

The solution velocity and pressure for each nodal point within the tolerance limit 0.0001 has been obtained. The variations of values of outlet velocity V_o with the change of non-dimensional ratio of inlet velocities V_3/V_1 were plotted for outlet section (designated by yellow arrow). The selected section is shown in Fig. 3.

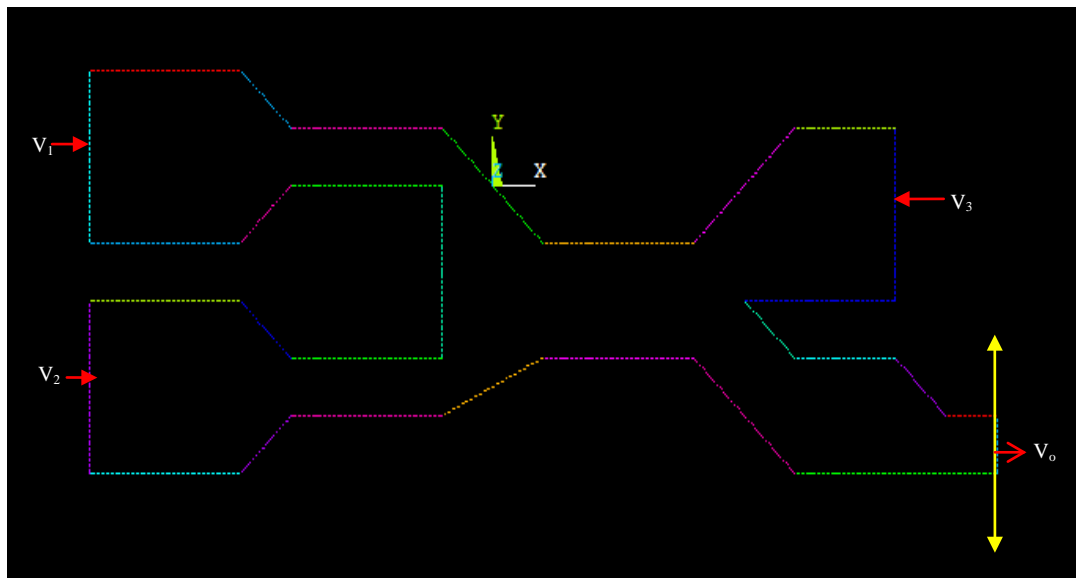


Fig. 3. Selected section chosen for studying designated by yellow arrow

In Fig. 4(a) Variation of outlet velocity with respect to different V_3/V_1 ratio has been presented. For constant dimensionless distant Y/D_o along the radius of the pipe. The result for $V_3/V_1 = 0.18$ shown in Fig. 4(a) shows that outlet velocity profile changes with respect to V_2/V_1 . For V_2/V_1 ratio upto 1 the velocity profile remain somewhat parabolic then with the increase of V_2/V_1 ratio the profile changes. Also it appears that for constant value of Y/D_o the maximum value of V_o/V_1 is found at the midpoint along the radius of the pipe. The result for $V_3/V_1 = 0.8$ is shown in Fig. 4(b). Here again we see that V_2/V_1 ratio controls the outlet velocity profile. From the results of $V_3/V_1 = 1$ and $V_3/V_1 = 5$ are shown in Fig. 4(c) and 4(d). It can be seen that also for $V_3/V_1 =$ ratio upto 1 the velocity profile remains same and after that it changes drastically. Also it can be seen that for V_3/V_1

ratio greater than 1, V_o/V_1 ratio is maximum between approximately $Y/D_o = 0.2$ to $Y/D_o = 0.8$. So it can be concluded that for both V_3/V_1 and V_2/V_1 ratio less than 1 flow become smooth and ordered which indicate the characteristics of laminar flow.

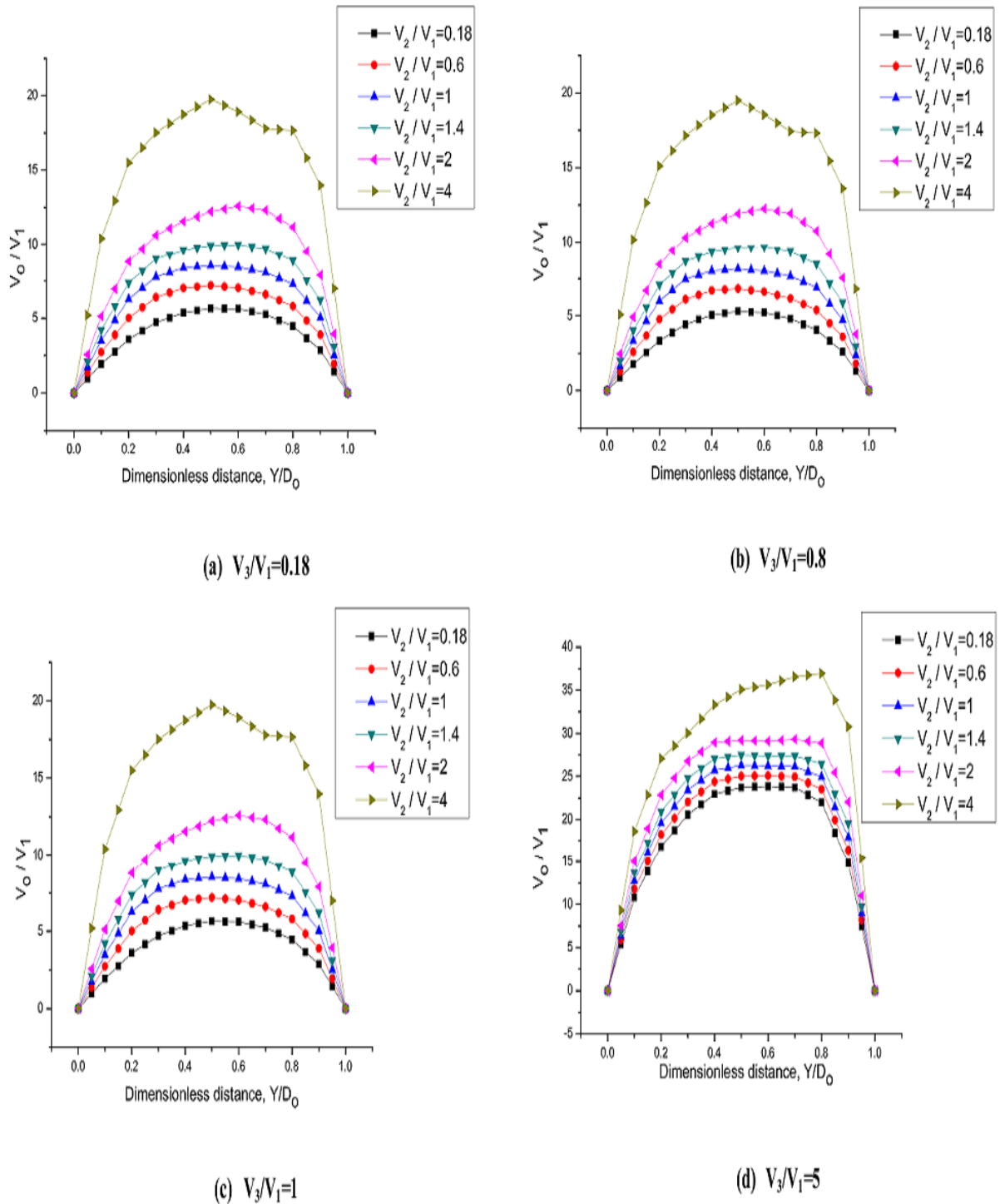


Fig. 4. Variation of outlet velocity for different V_3/V_1 ratio

The vector plot of velocity distribution inside the pipe model has been presented for different V_3/V_1 ratios with respect to $V_2/V_1 = 1$ in Fig. 5. The vector plot for $V_3/V_1 = 0.18$ shown in Fig. 5(a) shows that for V_3/V_1 ratio less than V_2/V_1 ratio flow is dominated by V_2/V_1 ratio and losses in the pipe appears to be small. When inlet pipes velocity is same i.e. when $V_3/V_1 = 1$ and $V_2/V_1 = 1$ shown Fig. 5(b) velocity profile throughout the pipe started to change this may be because of the effects sudden enlargement and sudden contraction presence at various position in the pipe becomes dominant.. From the vector plot for $V_3/V_1 = 1.6$ shown in Fig. 5(c) it

appears that for V_3/V_1 ratio larger than V_3/V_1 flow aberrates from the smooth and ordered characteristics and higher the V_3/V_1 ratio becomes higher the aberration which can be clearly seen from the Fig. 5(d).

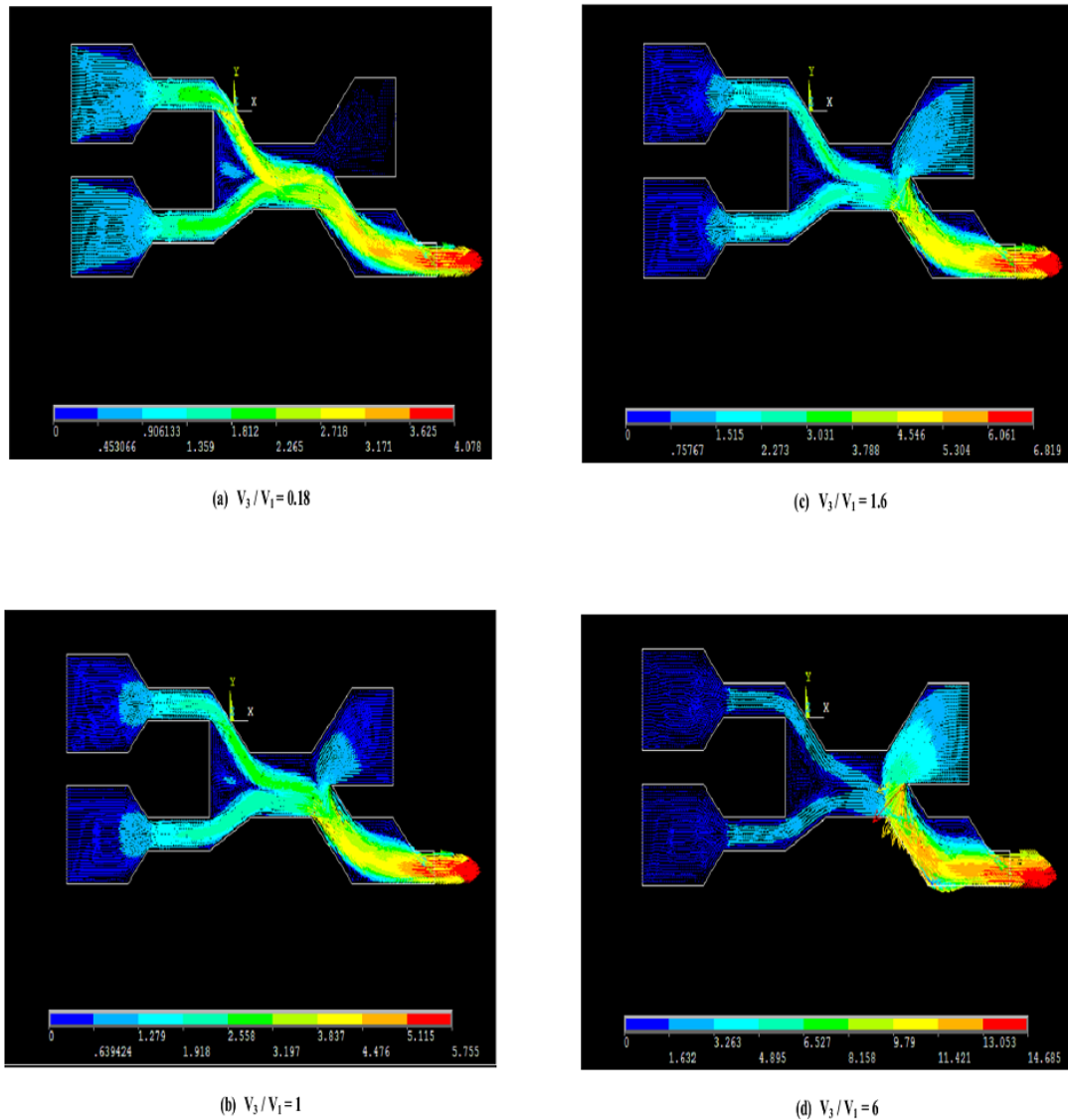


Fig. 5. Vector plot of velocity distribution inside the pipe for $V_2 / V_1 = 1$

6. Conclusions

The present study provides the solution for velocity and the pattern of flow in a complex pipe system using finite element approach. Both quantitative and qualitative results of pressure vessel obtained which establish the soundness and appropriateness of the present finite element approach. This solution technique is valid for any complex system of pipe.

7. References

- [1] Navtej Singh, Suneev Anil Bansal, N.K Batra, "Visualization of Flow Behavior and Its Effected Contour in Sudden Contraction, Sudden Enlargement and Sudden Elbow By ANSYS", International Journal of Engineering and Research Applications (IJERA), Vol.2, ISSUE 5, ISSN: 2249-3905, 2012.
- [2] D Rohitendra K Singh, "A Study of Air Flow in a Network of Pipes Used in Aspirated Smoke Detectors", M.Sc. Thesis, Victoria University, Australia, 2009.
- [3] "ANSYS" Theory Manual and Expanded ANSYS Workbook.

Numerical Study of Laminar Boundary Layer Using Navier-Stokes Equation and Finite Volume Method

Toukir Islam¹, Md.Minal Nahin² & Md. Abu Abrar³

^{1,2,3}Bangladesh University of Engineering and Technology, Bangladesh. E-mail: ¹toukir.buet07@gmail.com, ²neon.nahin@gmail.com & ³abrar.me07.buet@gmail.com

Abstract

The boundary layer is known as the distance from the surface to a particular point perpendicular to the direction of flow where the flow velocity has retained 99% of the free stream velocity providing 'no-slip' condition at the surface. It can be laminar or turbulent and there is a zone of 'transition' from laminar to turbulent depending on Reynolds number. In this paper the properties of laminar boundary layer such as development of velocity profile along the flow direction, boundary layer thickness, displacement thickness, momentum thickness, shape factor, wall shear stress, friction coefficient, drag coefficient etc. for 5 m/s flow over a smooth flat plate of 1 meter are studied by exact solution of Blasius's equation and compared with computer-aided CFD solution using Navier-Stokes equations and Finite Volume method. It is found that different boundary layer thicknesses are direct function of local Reynolds number and these thicknesses increase as the flow travels further downstream. Moreover the shear stress and subsequently, the local skin friction reduce as the flow travels in downstream direction. The shape factor is found to be 2.590361 which is close the value obtained from Blasius's solution.

Keywords: Blasius's equation, boundary layer thickness, displacement thickness, momentum thickness, shape factor, friction coefficient.

1. Introduction

At the interface between a fluid and a surface in relative motion, a condition known as 'no slip' dictates an equivalence between fluid and surface velocities. Away from the surface, the fluid velocity rapidly increases; the zone in which this occurs is known as the boundary layer. The boundary layer is the thin region of flow adjacent to a surface, where the flow is retarded by the influence of friction between a solid surface and fluid. Although the boundary layer occupies geometrically only a small portion of flow field, its influence on different aerodynamic and heat transfer phenomena to the body is immense as Prandtl described as 'marked results' [1]. Smooth thin flat plate has long been considered to be simplest form to describe boundary layer as there is no pressure gradient involved and it was probably the first example illustrating the application of Prandtl's boundary layer theory.

Shear stress acts as a pivotal parameter for the existence of boundary layer. The shear stress on the smooth surface is a direct function of the velocity gradient at the surface of the plate. This shear stress acting at the plate surface sets up a shear force which opposes the fluid motion and fluid close to the wall is decelerated. If the flow travels further along the surface, at zero pressure gradients, the shear force is effectively increased due to the increased plate surface wetted area. More and more of fluid retarded and the thickness of the fluid layer increases. Reynolds number (Re) can be considered as the measure-stick for behavior of the boundary layer. If the Re; calculated locally is low, the fluid flow close to the wall may be categorized as laminar. For smooth, polished plates the transition from laminar to turbulent may be delayed until Re 500000 i.e. below this Re the flow can be considered as laminar. However, for rough plates or for turbulent approach flows, transition may occur at much lower values.

There are number of intriguing properties of boundary layer which are decisive for analyzing different flow phenomena like drag or shear stress. These properties can be expressed through mathematical expressions which are direct function of local Re and distance of the point under consideration on the plate from the leading edge. Boundary layer thickness δ is the distance from the surface of the plate in perpendicular direction up to a point where the velocity of the flow is 99% of the free stream velocity. Displacement thickness δ^* can be considered

as missing mass flow which is the difference between actual mass flow and hypothetical mass flow through the boundary layer if the boundary layers were not present. Another boundary layer property of importance is the momentum thickness θ , which is an index that is proportional to the decrement in momentum flow due to the presence of the boundary layer. It is the height of a hypothetical streamtube which is carrying the missing momentum flow at free stream conditions. Shape factor H of velocity profile is the ratio of the displacement thickness to the momentum thickness which increases in an adverse pressure gradient. For laminar flow with zero pressure gradient (such as a flat plate), it is 2.59 and it reaches to 3.5 at separation. Local friction coefficient $C_{f,x}$ is the dimensionless number defined as the ratio of wall shear stress to dynamic pressure.

Blasius [2] was the first one to illustrate Prandtl's boundary layer theory through the application of flow over a flat plate. He provided the legendary equation known as 'Blasius's equation'. Bairstow [3], Goldstein [4] solved it through analytical procedure while Töpfer [5] solved it using Runge-Kutta numerical method. Howarth [6] solved the equation with greater accuracy using numerical procedure. Steinheuer [7] published a systematic review of the solutions to Blasius's equation. Filobello-Nino et. al. [8] provided with an approximate solution of Blasius's equation by using HPM (Homotopy Perturbation Method) and described the behavior of a two-dimensional viscous laminar flow over flat plate. Aminikhah [9] persuaded analytical approximation to the solution of non-linear Blasius's viscous flow equation by LTNHPM (Laplace Transform and New Homotopy Perturbation Method). In this paper the laminar boundary layer properties are illustrated using exact solution of Blasius's equation and these properties are analyzed using flow over one side of a smooth flat plate with no pressure gradient by solving the Navier-Stokes equation set using the Finite Volume Method.

2. Mathematical Model

Incompressible, two dimensional flows over a thin flat plate at 0° angle of incidence is simplest example used in the first place to describe Prandtl's boundary layer theory. For such flow the density and viscosity are constant and the pressure gradient is zero as inviscid flow over the smooth flat plate at 0° angle of attack yields constant pressure over the surface. Thus the Navier-Stokes equations reduce to:

$$\frac{\partial u}{\partial x} + \frac{\partial v}{\partial y} = 0 \quad (1)$$

$$u \frac{\partial u}{\partial x} + v \frac{\partial v}{\partial y} = \nu \frac{\partial^2 u}{\partial y^2} \quad (2)$$

$$\frac{\partial p}{\partial y} = 0 \quad (3)$$

Here ν is the kinematic viscosity defined as $\nu = \mu/\rho$. The exact solution is described by Blasius [2]; a student of Prandtl in his doctor's thesis at Goettingen. The independent variable (x, y) are then transformed into (ξ, η) as $\xi = x$ and $\eta = y \sqrt{\frac{V_\infty}{\nu x}}$ and the stream function is considered to be $\psi = f(\eta) \times \sqrt{x \nu V_\infty}$ [10], [11], [12] where f is strictly a function of η . Blasius concluded with a legendary equation known as Blasius's Equation' as form of

$$2f''' + ff'' = 0 \quad (4)$$

Where the function $f(\eta)$ has the property that is f' is described as $\frac{u}{V_\infty}$. This is a third order non-linear differential equation which requires three boundary conditions to solve which are: at $\eta = 0 : f = 0, f' = 0$ and $\eta = \infty : f' = 1$. The equation was solved by Blasius using a series of approach. The properties of boundary layer are defined as in Table 1.

Table 1. Properties of laminar boundary layer over flat plate

Boundary layer property	Mathematical expression
Boundary layer thickness (δ)	$5x/\sqrt{Re_x}$
Displacement thickness (δ^*)	$1.72x/\sqrt{Re_x}$
Momentum thickness (θ)	$0.664x/\sqrt{Re_x}$
Shape factor (H)	δ^*/θ
Friction coefficient ($C_{f,x}$)	$0.664/\sqrt{Re_x}$
Drag coefficient (C_D)	$1.328/\sqrt{Re_L}$

Here Re_x refers to be local Reynolds number and Re_L is the overall Reynolds number. To calculate the Re_x , the distance is measured from the leading edge of the flat plate. In case of Re_L , the distance is the total length of the plate. The length of the plate is kept 1 m because the development of laminar boundary layer is expected to be completed within this length. Longer plate length would increase the size of computational domain thus more computational time would be required.

3. Numerical Procedure

Equation set consisting equation no (1), (2) and (3) are solved using 'Finite Volume' method. The cell-centered finite volume (FV) method is used to obtain conservative approximations of the governing equations on the locally refined rectangular mesh. The governing equations are integrated over a control volume which is a grid cell, and then approximated with the cell-centered values of the basic variables. The integral conservation laws may be represented in the form of the cell volume and surface integral equation:

$$\frac{\partial}{\partial t} \int \mathbf{U} dv + \oint F \cdot ds = \int Q dv, \text{ which is replaced by } \frac{\partial}{\partial t} (Uv) + \sum_{cell\ faces} F \cdot s = Qv$$

The second-order upwind approximations of fluxes are based on the implicitly treated modified Leonard's QUICK approximations [13] and the Total Variation Diminishing (TVD) method [14]. The rectangular computational domain is constructed, so it encloses the solid body and has the boundary planes orthogonal to the specified axes of the Cartesian coordinate system. Then, the computational mesh is constructed in the following several stages. First of all, a basic mesh is constructed. For that, the computational domain is divided into slices by the basic mesh planes, which are evidently orthogonal to the axes of the Cartesian coordinate system. The basic mesh is determined solely by the computational domain and does not depend on the solid/fluid interfaces. Then, the basic mesh cells intersecting with the solid/fluid interface are split uniformly into smaller cells in order to capture the solid/fluid interface with mesh cells of the specified size i.e. with respect to the basic mesh cells. The following procedure is employed: each of the basic mesh cells intersecting with the solid/fluid interface is split uniformly into 8 child cells; each of the child cells intersecting with the interface is in turn split into 8 cells of next level, and so on, until the specified cell size is attained. At the next stage of meshing, the mesh obtained at the solid/fluid interface with the previous procedure is refined (i.e. the cells are split further or probably merged) in accordance with the solid/fluid interface curvature. The criterion to be satisfied is established as follows: the maximum angle between the normals to the surface inside one cell should not exceed certain threshold; otherwise the cell is split into 8 cells. As a result of all these meshing procedures, a locally refined rectangular computational mesh is obtained and used then for solving the governing equations on it.

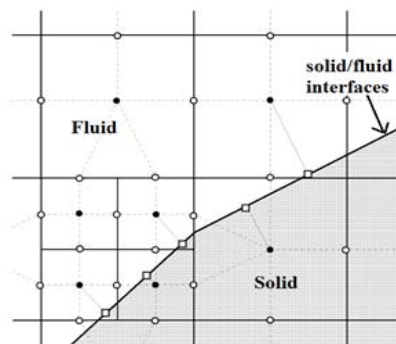


Fig. 1. Computational mesh type

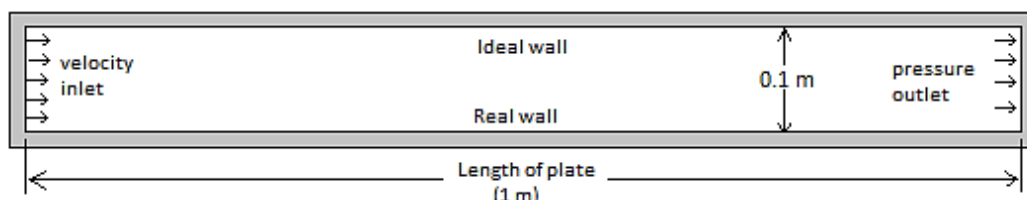


Fig. 2. Computational design set-up

The 'inlet velocity' of air is 5 m/s at 293.2 K and 101325 Pa conditions. 'Pressure opening' at the outlet is at 101325 Pa. Upper wall of the design is 'Ideal Wall' while the lower wall of 1 m length is 'Real Wall' i.e. 'no-slip' condition is applied. Needless to say that the lower wall is considered as the smooth flat plate.

4. Results and Discussion

For air flow over a smooth flat plate of 1 meter length without any pressure gradient and heat transfer, the local Re never crossed the critical Re (500000) that could cause transition of laminar flow to turbulent flow. So the boundary layer generated at the vicinity of the lower wall of the computational design can be considered as laminar boundary layer. At the area closer to the leading edge of the plate, the boundary layer thickens rapidly (Fig. 3 and Fig. 4 (a), (b), (c)). As the flow travels further downstream the rate of thickening of the boundary layer decreases and at some points around 70-90% of the plate length, the thickening effect becomes more obscure (Fig. 4(e)). With increasing distance from leading edge, the point at which the local velocity of the flow becomes almost equal to the free stream velocity; travels more to the perpendicular direction of the plate i.e. y direction. Both from Fig. 3 and Fig. 5 it is evident that the thickness of the boundary layer δ increases as the flow travels more downstream because more and more fluid particles pile up due to increase of wall shear stress at that direction.

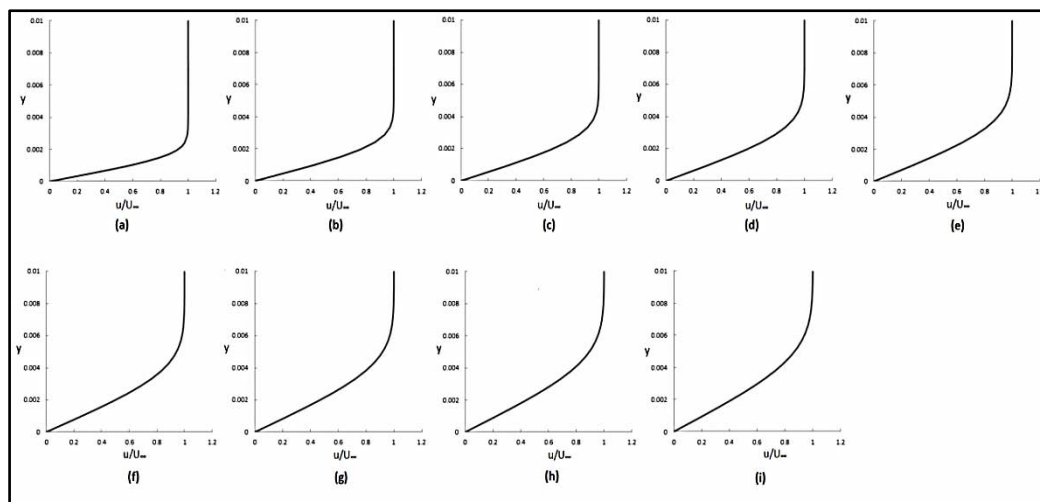


Fig. 3. Velocity profile at (a) $x=0.1\text{m}$, (b) $x=0.2\text{m}$, (c) $x=0.3\text{m}$, (d) $x=0.4\text{m}$, (e) $x=0.5\text{m}$, (f) $x=0.6\text{m}$, (g) $x=0.7\text{m}$, (h) $x=0.8\text{m}$, (i) $x=0.9\text{m}$. The perpendicular distance from the plate (y- axis) is in 'm'.

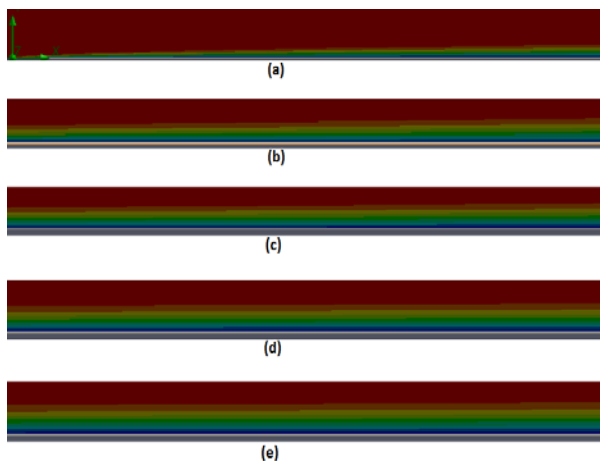


Fig. 4. Development of boundary layer at (a) $x=0.0$ to 0.1, (b) $x=0.1$ to 0.2, (c) $x=0.2$ to 0.3, (d) $x=0.4$ to 0.5 and (e) $x=0.7$ to 0.8.

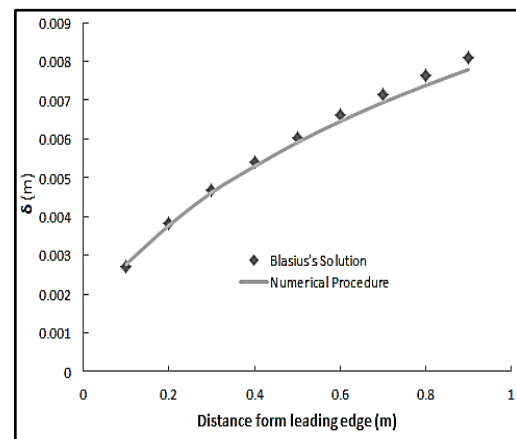


Fig. 5. Boundary layer thickness (δ) at different position of the plate.

Boundary layer thickness is so far referred to only in physical terms. It is however, possible to define boundary layer thickness in terms of the effect on the flow. Displacement thickness is defined as the ‘distance’ the surface would have to move in the y direction to reduce the flow passing by a volume equivalent to the real effect of the boundary layer. Displacement thickness δ^* for the boundary layer increases with increasing distance from the leading edge of the plate (Fig.6). With increasing distance from the leading edge of the plate, δ^* increases due to the same reason as δ increases. That means the plate would have to move further in y direction in case there is no boundary layer to compensate the flow reduction due to boundary layer. Similar outcome is found for momentum thickness, θ as decrement in momentum flow due to the boundary layer increases as the flow travels further downstream (Fig.7).

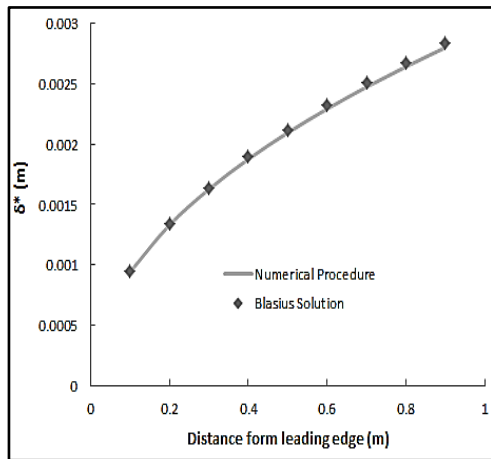


Fig. 6. Displacement thickness (δ^*) at different position of the plate.

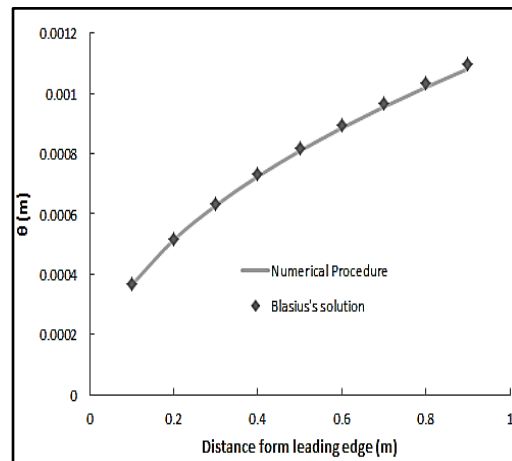


Fig. 7. Momentum thickness (θ) at different position of the plate.

The shape factor from Blasius’s calculation [2] is 2.59 for the flat plate while from present calculation, it is 2.590361 and as this value would be around 3.5 at separation [15], it can be concluded that separation of flow from the plate surface did not occur. The shear stress on a smooth plate is a direct function of the velocity gradient at the surface of the plate and this velocity gradient exists in a direction perpendicular to the surface. In immediate neighborhood of the body in which the velocity gradient normal to the wall is very large and the very small viscosity of the fluid exerts an essential influence that results in larger shear stress (Fig. 8). As we travel further upward from the plate, the influence of viscosity becomes trivial and flow at this region can be considered frictionless.

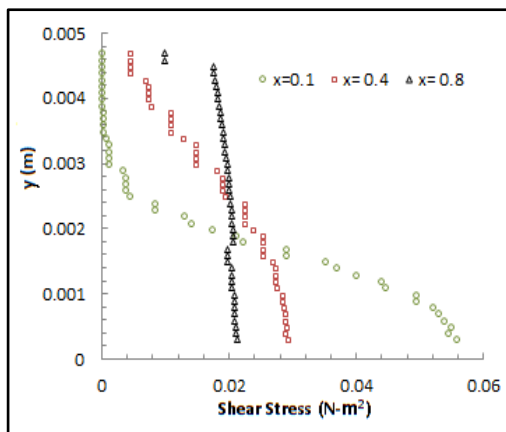


Fig. 8. Shear stress distribution in perpendicular direction of the plate.

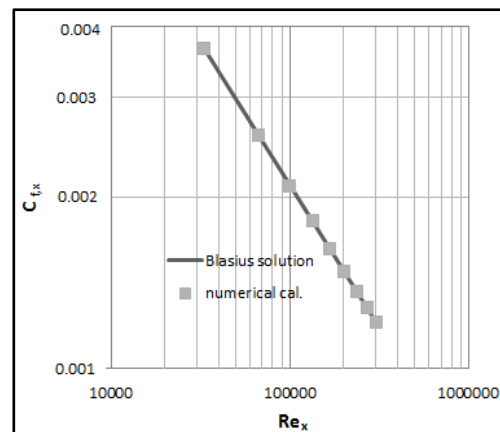


Fig.9. Friction coefficient ($C_{f,x}$) at different Re_x

As flow travels further downstream from the leading edge, Re increases and the velocity gradient decreases (in laminar boundary layer region) and thus the shear stress decreases. As the friction coefficient is directly proportional to the shear stress, it also decreases as the flow travels towards the downstream (Fig. 9). The skin friction drag for the smooth flat plate is found to be 0.002297 from Blasius's solution.

5. Conclusion

Different laminar boundary layer properties for air flow over a flat smooth plate is studied by Blasius's solution and Finite Volume Method of solving the Navier-Stokes equations and it is evident that the Finite Volume Method serves well in determining the behavior of laminar boundary layer. Different boundary layer thicknesses are direct function of local Re i.e. the distance from the leading edge of the plate and these thicknesses increases as the flow travels further downstream. Moreover the shear stress and subsequently, the local skin friction reduce as the flow travels further downstream. This analysis is limited for only one side of a smooth flat plate without any pressure gradient and heat generation or transfer phenomena and most importantly, when the flow is devoid of any turbulence.

6. References

- [1] J.D. Anderson Jr., *Fundamental of Aerodynamics [SI Units]*, *Tata McGraw Hill*, fifth edition, 2010.
- [2] H. Blasius, "Grenzschichten in Flüssigkeiten mit kleiner Reibung", *Zeit. Math. Phys.*, Vol.56, pp.1-37 (English translation), 1908.
- [3] L. Baird, "Skin Friction", *Journal of Royal Aeronautical Society*, Vol.19, No.3, pp.3-23, 1925.
- [4] S. Goldstein, "Concerning some Solutions of the Boundary Layer Equations in Hydrodynamics", *Proc. Cambridge Philos. Soc.*, Vol.26, pp.1-30, 1930.
- [5] C. Töpfer, "Bemerkung zum Aufsatz von H. Blasius: Grenzschichten in Flüssigkeiten mit kleiner Reibung", *Z. Math. Phys.*, Vol.60, pp. 397–398, 1912.
- [6] L. Howarth, "On the Solution of the Laminar Boundary Layer Equations", *Proc. Roy. Soc. London A*, Vol.164, pp.547–579, 1938.
- [7] J. Steinheuer, "Lösungen der Blasius'schen Grenzschichtdifferentialgleichung", *Proc. Wiss. Ges. Braunschweig*, Vol.20, pp. 96-125, 1968.
- [8] U. Filobello-Nino, H. Vazquez-Leal, R. Castaneda-Sheissa, A. Yildirim, L. Hernandez-Martinez, D. Pereyra-Diaz, A. Perez-Sesma, and C. Hoyos-Reyes, "An Approximate Solution of Blasius Equation by Using HPM Method", *Asian Journal of Mathematics and Statistics*, Vol.5, No.2, pp.50-59, 2012.
- [9] H. Aminikhah, "Analytical Approximation to the Solution of Nonlinear Blasius' Viscous Flow Equation by LTHPM", *ISRN Mathematical Analysis*, Vol. 2012, Article ID 957473, 2012.
- [10] W.F. Huges, and J.A. Brighton, *Dinamika De Los Fluidos*. *McGraw Hill*, *Sao Paulo*, 1967.
- [11] R. Resnick, and D. Halliday, *Physics*. Vol.1, *John Wiley and Sons Inc.*, *USA*, 1977.
- [12] L.D. Landau, and E.M. Lifshitz, *Fluid Mechanics*, *Pergamon Press*, *UK*, Second Edition, 1987.
- [13] P.J. Roache, *Technical Reference of Computational Fluid Dynamics*, *Hermosa Publishers*, *Albuquerque, New Mexico, USA*, 1998.
- [14] C. Hirsch, *Numerical computation of internal and external flows*, *John Wiley and Sons*, *Chichester*, 1988.
- [15] R.W. Fox, A.T. McDonald, and P.J. Pritchard, *Introduction to Fluid Mechanics*, *John Wiley and Sons Inc.*, Sixth Edition, pp. 441-442, 2009.

Numerical Simulation and aerodynamic characteristic analysis of a Paraboloid-tip Bullet

Md. Tarique Hasan Khan¹

¹Student, Bangladesh University of Engineering and Technology (BUET), Bangladesh
E-mail: tanim89@gmail.com

Fahim Ahmed

Student, Bangladesh University of Engineering and Technology (BUET), Bangladesh
E-mail: manushfahim@gmail.com

Abstract

A bullet is a projectile and all projectiles moving through a reservoir of gas or liquid create a fluid boundary film between the surface of the projectile and the free flowing fluid through which it travels. When a bullet is fired, strong shock wave is generated on the bullet which results in flow separation and thus low pressure drag. This paper intends to investigate the aerodynamics characteristics of a definite dimension paraboloid-tip bullet that is fired from a .38 super automatic pistol cartridge. Bullet surface is constructed and various aerodynamic constrains are simulated using CFD and CAD tool. Besides, boundary layer is simulated numerically using pressure contour and velocity contour.

Keywords: Bullet, Computational Simulation, numerical analysis, aerodynamics.

1. Introduction

A bullet is a projectile propelled by a firearm, sling, or air gun. A bullet does not contain explosives, but damages the intended target by its impact or penetration. The word "bullet" is sometimes used to refer to ammunition generally, or to a cartridge, which is a combination of the bullet, casing/shell, powder, and primer. What happens to a bullet inside the bore is termed internal ballistics. Once it leaves the barrel, it is governed by external ballistics. Here, the bullet's shape is important for aerodynamics, as is the rotation imparted by the rifling. Rotational forces stabilize the bullet gyroscopically as well as aerodynamically. Any asymmetry in the bullet is largely canceled as it spins. With smooth-bore firearms, a spherical shape was optimum because no matter how it was oriented, it presented a uniform front. These unstable bullets tumbled erratically, but the aerodynamic shape changed little giving moderate accuracy. Generally, bullet shapes are a compromise between aerodynamics, interior ballistics necessities, and terminal ballistics requirements. This paper is primarily on the numerical aerodynamic characteristics analysis on a bullet surface as well as its surroundings it is dashing through.

2. Bullet Specification and geometry

During preprocessing, 2D model is drawn on CAD software with proper dimensions of a 9x19mm Paraboloid (abbreviated 9mm, 9x19mm or 9x19) is also known as a paraboloid-tip bullet.

The specifications for the bullet are as follows:

Bullet Diameter, $d = 9.03$ mm,

Bullet length, $l = 10.54$ mm.

When the trigger is pulled, the bullet is rammed violently and lunges forward leaving the cartridge behind. That's why our interest lies here only into the leading part of the bullet of fig.1 which experiences various aerodynamic properties while dashing forward.

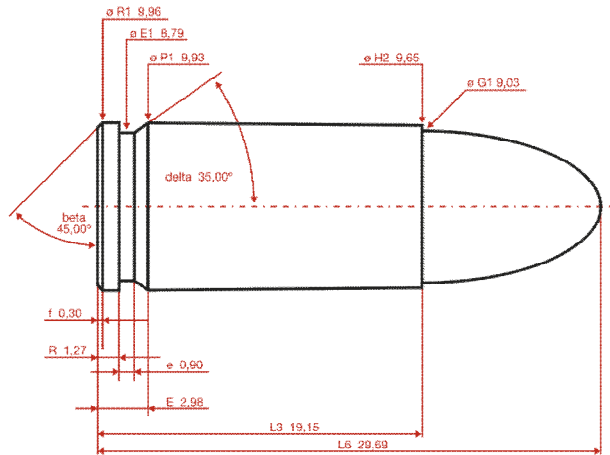


Fig.1: 9x19mm Paraboloid-tip maximum C.I.P. cartridge dimensions

3. Numerical Methodology

We have created a large area encompassing the bullet which is the selected contour for analyzing. The area occupied by the fluid is divided into discrete cells (the mesh). Quadrilateral meshing type was used for meshing the area. (Fig.2, Fig.3) The physical modeling is defined. Boundary conditions are defined as wall, pressure far field and pressure inlet. This involves specifying the fluid behavior and properties at the boundaries of the problem. The inlet boundary defined as PRESSUR_INLET is set at 101325 Pa because atmospheric pressure is assumed outside and 300K was the temperature at outside. Moreover the maximum velocity of bullet was specified as inlet velocity to resemble actual flight of bullet, which was about 1350ft/s (Mach number 1.21). Since the flow is supersonic compressible, a density-based algorithm was used for numerical solution. The flow was assumed to be steady and inviscid for supersonic speed. For compressibility effect, energy equation was coupled with continuity and momentum equations. Courant number was taken less than but close to One (1) for stability of the solution and accuracy of the result. Finally a postprocessor is used for the analysis and visualization of the solution.

2D model of the desired bullet is simulated on CFD software on the later part of the drawing and meshing. Pressure and velocity contours, Velocity vector are obtained from the simulation software.

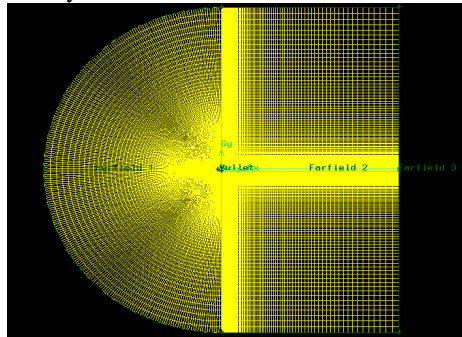


Fig.2: Meshing of total contour

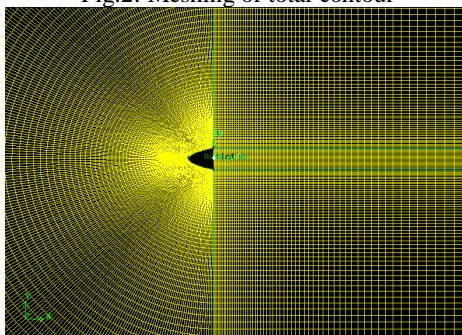


Fig.3: Meshing of total contour with bullet (closer view)

4. Post-processing analysis and Result

The figures attached represent the flow behavioral pattern across a paraboloid-tip bullet along with its enclosure during its travel through the air.

The pressure and velocity contour (Fig.4, Fig.5) shows the stagnation pressure (243000 Pa approx.) and zero velocity (due to no slip condition) at the blunt nose of the bullet. The density and entropy of the region also exceeds the normal value that creates disturbance. Moreover a detached bow shock wave is seen ahead of the nose at supersonic velocity (around 1.2059 Mach number). Reflecting the shock wave theory, abrupt high pressure as well as low velocity is observed along the shock area.

In case of supersonic flow, viscous effect is negligible. The flow has high moment of inertia and no positive pressure gradient develop. So, there is no flow separation along the parabolic surface of bullet.

When a supersonic flow encounters a convex corner, it turns around the corner by Prandtl Mayer Expansion Fan process. Across the fan the flow accelerates and Mach number increases, while the static pressure, temperature and density decrease. This expansion fan limits the maximum angle through which the flow can turn. Beyond this turn angle, there is a jump in temperature. In this case, the convex angle between the parabolic surface and the vertical rear edge of the bullet exceeds this maximum angle, which was calculated using Prandtl-Mayer Function. In fig.4, it can be seen that the air flowing past the convex corners experience a dramatic reduction in pressure through a certain angle, while in fig.5 and fig.6, this flow accelerates in the same direction and through the same angle. This is the angle through which the flow has turned by expansion fan process. Beyond this turn, there is a rise in temperature (fig.7).

While looking across the streamline velocity along the leading and trailing edge of the bullet (Fig.6, Fig.7) it is conversant that a vortex is formed. Due to wake formation, pressure decreases to about 30000 Pa and velocity rises to about 300 to 380 m/s. It is notable that, because of the expansion fan process, both the airflows passing the convex corners have turned towards each other, so the wake area has not been large. By numerical analysis, the total drag coefficient was found to be 0.0111, which indicates low-pressure drag due to small wake area. No lift was observed since the bullet profile was uniform, no spin was assumed, the trajectory was horizontal, and gravitational force was neglected.

If the analysis of graphs is taken into account, it shows clearly justified results of gradually decreasing pressure and increasing velocity along the bullet surface (Fig.8, Fig.9). Because of the curvature of the surface, the area between the streamlines near the surface constricts. For conservation of mass, the velocity increases along the surface (fig.11). From Bernoulli's principle, since the velocity is increasing, the pressure decreases along the surface.

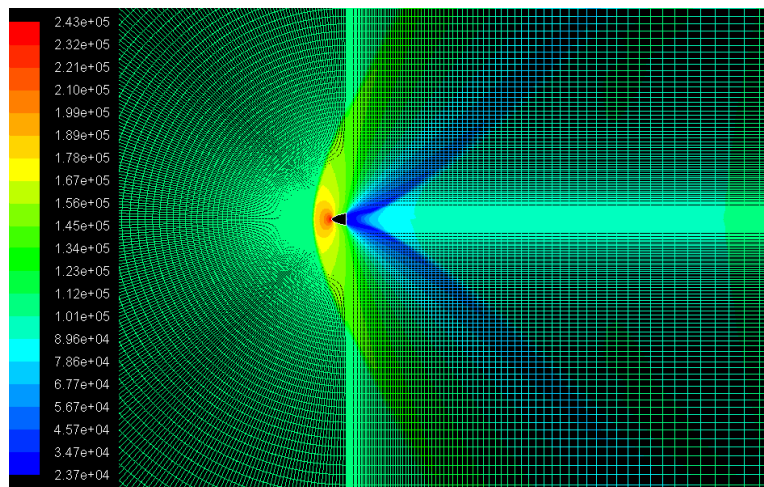


Fig.4: Pressure contour of the continuum and bullet

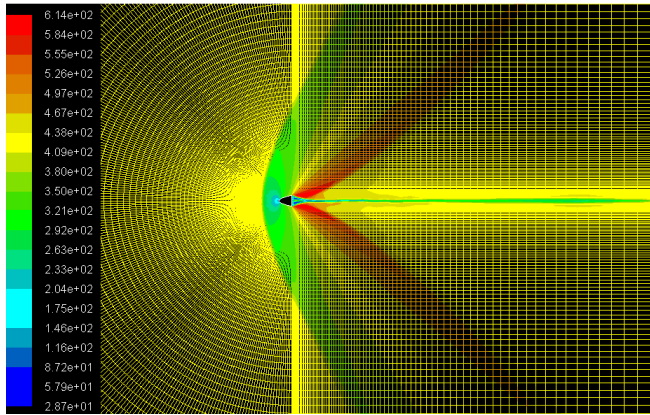


Fig.5: Velocity contour of the continuum and bullet

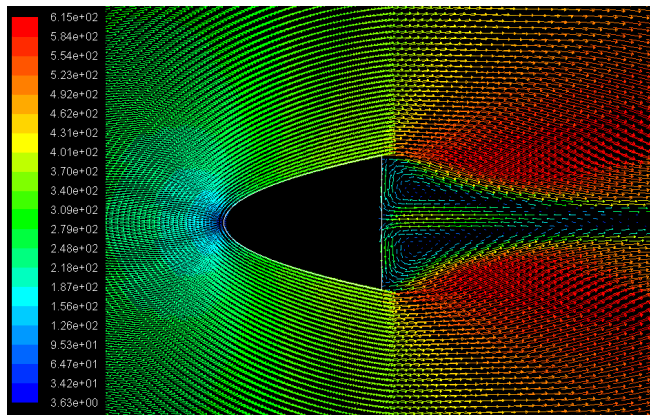


Fig.6: Velocity vector past the bullet profile

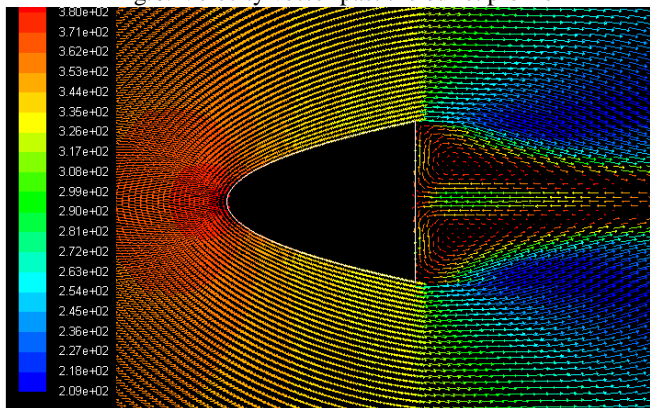


Fig. 7: Static Temperature of flow past the bullet profile

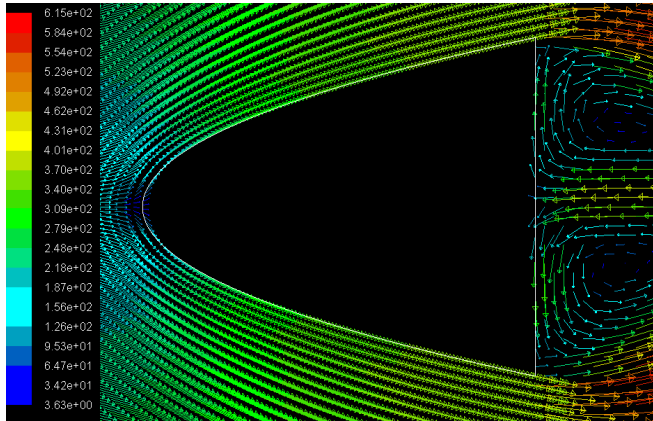


Fig.8: Streamline across the bullet (closer view)

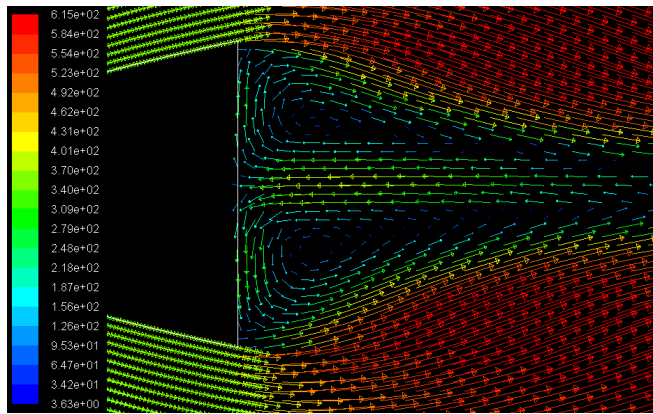


Fig.9: Vortex formation along the trailing edge of bullet

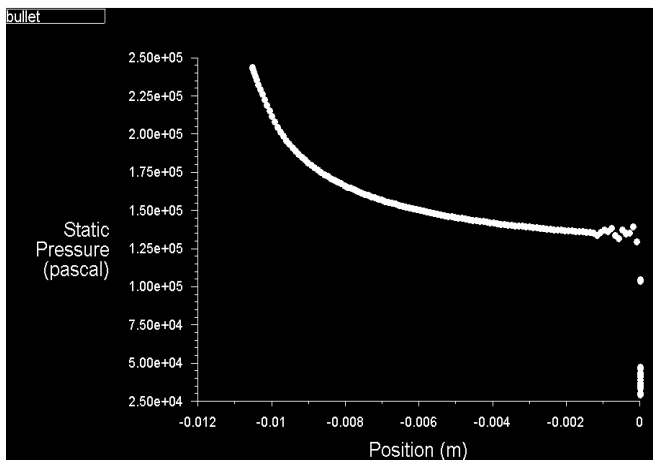


Fig.10: Static pressure distribution on bullet surface

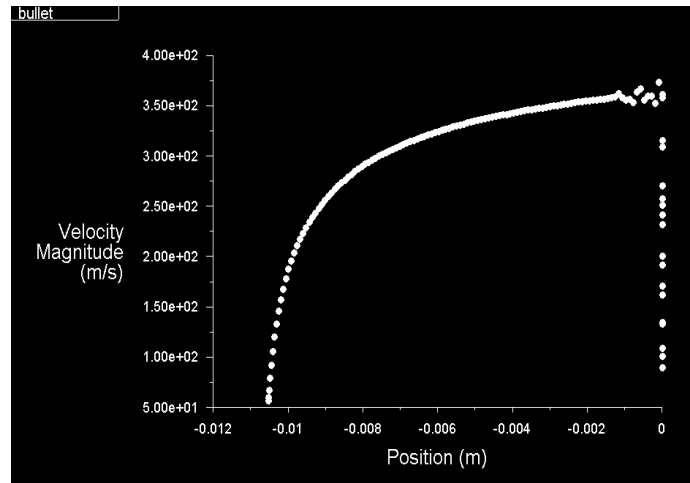


Fig.11: Velocity distribution across the bullet surface

5. Conclusions and Recommendation

Bow shock wave is desirable because a huge amount of air is trapped inside the shock area adjacent to the bullet surface, which prevents high temperatures and heat to generate. Thus metal deformation is restrained.

1. No gravity effect was considered simulating the bullet.
2. Viscosity was neglected. No matter how fast the airflow is, there is always a viscosity effect. So, the results may be a little deviated from the actual one.

As we know that there are bullet of different tip geometry, so further research possible where bullet geometry is different like as sharp-tip bullet or spherical shape bullet and their aerodynamic characteristics can be analyzed by the same procedure described above.

6. References

- [1] M. Tamail, Z. Wang, G. Rajagopalan and H. H. Aerodynamic. "Performance of a Corrugated Dragonfly Airfoil Compared with Smooth Airfoils at Low Reynolds Numbers"(45th AIAA Aerospace Sciences Meeting and Exhibit Jan 8 – 11, 2007, Reno, Nevada AIAA-2007-0483
- [2] D. W. Holder, "The interaction of a reflected shock with C. ht. Stuart and the contact surface and boundary layer in a shock tube".A.R.C.22 091. September, 1961.
- [3] Mangler, K. W."The inoculation of the flow field between a blunt body and the bow wave" *Proceedings of the Hypersonics ColstonSymposium, Bristol, 7959. Publishedby Butterworths Scientific Publications,1960.*
- [4] Seshimo, Y., and Fujii, M., "The supersonic blunt body problem -review and extension." *Journal Aero/Space Sciences, 25,pp.485-494. August, 1958*
- [5] Osborn, W.K. ,Crane J.F.W "Measurement of the sonic line, bow shockwave shape and stand-off distance for blunt-nosed bodies at M = 6.8".*MINISTRY OF AVIATIONAERONAUTICAL RESEARCH COUNCIL*
- [6] R. A. McCoy "Aerodynamic characteristics of a caliber .22 long rifle match ammunition" *Memorandum Report, BRL-MR 3877*
- [7] AJ Pejsa "Expanding ballistic projectile" *US Patent 4,776,279, 1988*
- [8] ZRCSC Longbo, KJWPT Junjie "THE THREE DIMENSION NUMERICAL SIMULATION OF AERODYNAMICS OF MORTAR BULLET"*JOURNAL OF BALLISTICS, 1999*
- [9] D Shough, OY Kwon, DF Leary "High-speed interferometric measurement of aerodynamic phenomena" *OELASE'90*
- [10] MA Sylvester, WF Braun "The Influence of Helical Serrations and Bullet Engraving on the Aerodynamic and Stability Properties of a Body on Revolution with Spin" 1970 - *DTIC Document*

Flow Separation Control on a NACA 0015 airfoil using Plasma Vortex Generator

C. W. Wong*, L. J. Wang, Z. Wu, C. H. Li, Q. Sun, M. M. Alam and Y. Zhou
Institute of Turbulence-Noise-Vibration Interactions and Control, Shenzhen Graduate School
Harbin Institute of Technology, Shenzhen, 518055, China
E-mail: cwwong@hitsz.edu.cn

Abstract

Experimental study has been conducted to determine the effect of plasma vortex generator (PVG) on a NACA 0015 airfoil for flow separation control. The novel design of the PVG consists of an arrangement of two serrated electrodes, with sharp peaks on each electrode facing opposite each other, horizontally separated by a dielectric material. In order to understand the characteristics of the vortex originated from the PVG, measurements including the longitudinal velocity and the spanwise vorticity of the induced flow structure, were conducted in the absence of free airstream using Pitot tube and PIV, respectively. The mechanisms of vorticity generation for PVG are discussed. Lift and drag measurements on the airfoil were conducted at low Reynolds number (7.7×10^4). The PVG showed effective control authority by generating counter-rotating vortices pairs, and it was found to lead to stall delay by 5 degrees and increase in lift coefficient by about 6%.

Keywords: plasma, vortex generator, flow control

1. Introduction

In the last decade, application of dielectric barrier discharge (DBD) becomes attractive in the field of flow control from low to moderate Reynolds number Re range. DBD plasma actuator is efficient for imparting momentum to the flow much like blowing or suction but without the mass injection. The simplest arrangement of DBD plasma actuator typically consists of a pair of electrodes horizontally separated by dielectric material. An alternating voltage is applied across the electrodes resulting in the generation of plasma in the vicinity of the electrodes. The voltage difference applied between the electrodes can vary from 1 kV to as high as 5 kV, and the frequency of the driving voltage is typically from 1 to 10 kHz [1,2]. The underlying physics, in terms of the plasma morphology and the geometric effects, of DBD plasma actuator was described by Enloe et al. [3,4]. For example, Enloe et al. [4] indicated that the dimensions of the exposed electrode strongly determine the performance of the actuator, and the expansion of the plasma, which is governed in part by the geometry of the lower, insulated electrode, has as considerable an impact on the performance of the actuator as the geometry at the exposed electrode edge. Nevertheless, DBD plasma actuators are commonly studied in asymmetric arrangement such that forcing is produced in longitudinal direction only. Moreau [5] provided comprehensive overview among the worldwide works on the electrical and mechanical characterization of plasma actuators in the absence of free air stream, and the application of plasma actuators for airflow control.

Flow control involves active [6,7,] or passive devices [8,9] with useful end results including lift augmentation, drag reduction, mixing augmentation, and flow-induced noise suppression. The DBD plasma actuators is an important type of active flow control device dedicated to the manipulation of low speed flows [10] and have been successfully applied in numerous flow control applications. These include lift augmentation on a wing section [11], low-pressure turbine blade separation control [12], airfoil flow separation control [13,14], and plasma flaps and slats [15]. In particular, Reference [14] demonstrated that the plasma actuators were found to lead to reattachment for angles of attack that were 8 degrees past the stall angle on a NACA 66₃-018 airfoil section at Re ranging from 77×10^3 to 333×10^3 . Their experimental results were remarkable, and it showed up to a 400% increase in the lift-to-drag ratio. Reference [15] also indicated that the leading-edge separation control using plasma actuators can achieve the increase of lift-to-drag improvement of as much as 340% at two different Re (2.17×10^5 and 3.07×10^5). Recent progress on flow control using DBD plasma actuators can also be found in Reference [16,17].

It is well understood that DBD actuator properties, such as size of the plasma region and generated airflow velocity depend on electrode configuration [4,5,18], dielectric material properties [18,19] and applied voltage [5]. However, other shapes of electrodes, for example, electrode with a serrated edge consisting of triangular patterns in series [18,20-23], were also used to improve airflow and more importantly, to generate the three-dimensional flow topology which could be useful for aerodynamics control applications [23,24]. Jousot *et al.* [24] demonstrated that the serrated plasma actuator configuration, which had an exposed electrode with a sawtooth edge, generated vorticity between each tip and root, and propagated downstream. However, the transverse velocity levels remain low in comparison with the longitudinal velocity and no well-established counter-rotating vortices were formed. Other geometric shapes of electrodes have also been studied, including the serpentine and square [23, 25], in order to promote a three-dimensional ionic wind. In particular, Wang *et al.* [23] observed the three-dimensional effects such as pinching and spreading the neighboring fluid for serpentine and square actuators. Also, a maximum jet angle at the trough of the square actuator was numerically predicted to be 36 degrees, whereas the jet angle of 35 degrees was experimentally demonstrated for a serpentine actuator.

In this study, the novel design of DBD plasma actuator with sawtooth edge on both exposed and grounded electrodes (plasma vortex generator) is considered, within which the sharp peaks of the serrated electrodes are carefully arranged to facing opposite each other. This serrated design was used in order to induce a three-dimensional ionic wind and more importantly, to increase the vorticity in the same way as yawed DBD actuators dedicated for flow separation control by vortex generation [26]. Firstly, the plasma vortex generator has been characterized by the measurements of longitudinal velocity and spanwise vorticity of the flow structure in the absence of free air stream using Pitot tube and particle image velocimetry, respectively. Secondly, we demonstrate the effect of a spanwise-oriented plasma vortex generator on a NACA 0015 airfoil based on force measurement from which we could determine the improved stall angle and lift coefficient. Details of the plasma vortex generator PVG and the experimental setup are summarized in Sec. 2. The results showing time-averaged velocity profiles, streamwise vorticity generated by the PVG, and the lift and drag coefficients of the airfoil are discussed in Sec. 3. Finally, conclusions and future works are drawn in Sec. 4.

2. Experimental Details

2.1 Actuator Design

The design of DBD plasma actuator has a sawtooth edge on both exposed and grounded electrodes, and is called the plasma vortex generator (PVG) in this study. The PVG consists of two metallic electrodes made out of adhesive copper foil tape separated by a thin PMMA material of 1 mm thickness. In order to investigate the characteristics of the ionic wind and the streamwise vortical structures originated from the PVG, a prototype of PVG has six sawtooth distributed uniformly along an edge of each serrated electrode is constructed (Fig. 1). The height h and width w of each sawtooth is 1.5 mm and 17.0 mm, respectively. The overall dimension of each exposed and grounded electrode is 140 mm in length, 15 mm wide, and 0.15 mm thick. The exposed electrode is connected to an AC power supply, that the output voltage is controlled by a signal generator (Rigol DG 4062). Thus, it could deliver sine voltage V_p of 8–20 kV in amplitude with a frequency of about 5000–15000 Hz. The grounded electrode is connected to the earth terminal of the AC power supply, and is encapsulated with an insulating tape to avoid plasma formation on this side. The electrical parameters are visualized with an oscilloscope (Rigol DS2072). The voltage is measured with a high voltage probe (Tektronix P6015A), whereas the current is measured by using a current probe (Tektronix P6021) in series with the discharge setup, placed between the ground and the grounded electrode (Fig. 2).

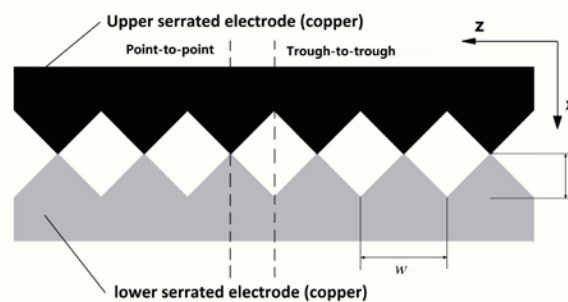


Fig. 1. Illustration of the prototype of plasma vortex generator

2.2 Characterization of the PVG

Firstly, the flow generated by the PVG is measured by using a Pitot tube, giving a time-averaged velocity of the ionic wind. The Pitot tube is a glass tube having an inner diameter of 0.5 mm, which resulting an accuracy of

a few μm in x - and y - directions. The glass tube is connected to a Furness FCO510 micromanometer (0–20 mmH_2O , 0–18 m/s) by a Tygon tube of about 0.5 m long. The glass tube can be travelled along 3 axes above the actuator with the three-component traverse, which has 0.02 mm displacement accuracy, controlled by a computer. The analog output of the micromanometer is connected to the FCS487 Data logger. For each measure, 450 samples at 5 Hz are recorded in order to seek the convergence of the time-averaged velocity value.

Secondly, the induced vorticity is examined by using the particle image velocimetry (PIV). The PVG is operated in a quiescent environment in an Acrylic glass box (500 mm length \times 500 mm width \times 800 mm height), which is seeded using a TSI 9307-6 particles generator. The particle droplets are on average 1 μm in diameter, and are generated from olive oil. The PIV system consists of a dual beam laser system (Litron LDY304-PIV, Nd:YLF), a CCD camera and a PC. A laser sheet of about 2 mm thickness is formed above the PVG. The time between pulses is 150 μs , and the trigger rate is 727 Hz for double frame mode. The PIV data presented in this paper are the average of 200 image pairs within which 200 vector fields are recorded. The images are recorded using a Vision Research high-speed camera (Phantom V641) with a 4-megapixel sensors and 2560 pixels \times 1600 pixels resolution. The viewing area used for the calculations of the vector fields is 102 mm \times 37 mm. Post-processing of the velocity data is conducted using Tecplot. Figure 2 shows the schematic of experimental setup for the PIV measurements.

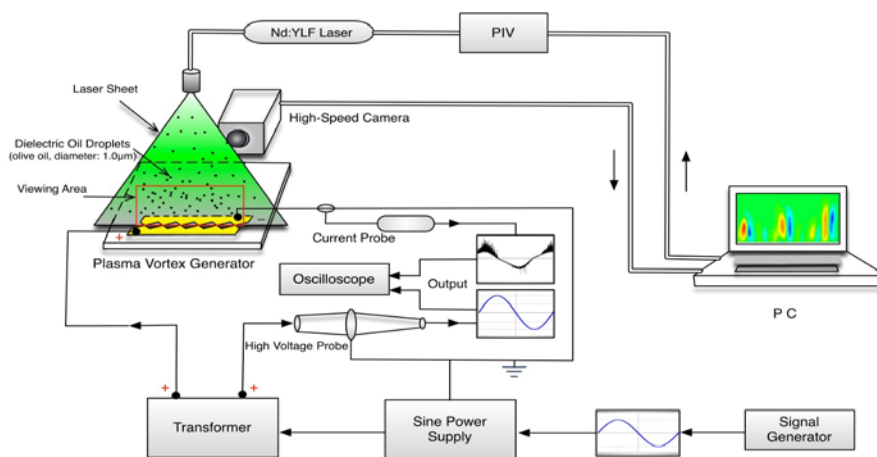


Fig. 2. Schematic of experimental setup for the PIV measurements

2.3 Force Measurement

Force measurements were performed in a closed circuit wind tunnel with a working section of $L \times W \times H = 3.0 \text{ m} \times 0.8 \text{ m} \times 1.0 \text{ m}$. The non-uniformity of the flow in the test section was no more than 0.5% and the free-stream longitudinal turbulence intensity was approximately 0.4% for the Re examined. The freestream velocity was measured using a Pitot–static tube connected to a Furness micromanometer, with an uncertainty of less than 2.0%. A NACA 0015 airfoil model with the span of 300 mm and the chord length of 200 mm was investigated at a freestream velocity U_∞ of 6 m/s , which results in chord Re of 7.7×10^4 . No boundary-layer trips were employed. The PVG consisting of 10 pairs of sharp peaks, covering the central 60% of airfoil span, was installed at 2% downstream from the leading-edge and on the suction side of the airfoil. The airfoil model was vertically suspended between two false walls in the test section, and the lift and drag forces were measured using a three component load cell (LSM-B-SA1, 10 N). The load cell has a rated output of 0.5 mV/V , and the hysteresis is $\pm 0.5\%$. The time-averaged aerodynamic forces were measured with a moderate sampling rate of 1.0 kHz, and a 500 Hz filter was used in the data acquisition system. The accuracy of the lift and drag measurements is approximately $\pm 0.05\%$. Aerodynamic forces were normalized by the freestream dynamic pressure and airfoil area. Note that the angle of attack α of the airfoil section is set by a rotary table, and the uncertainty on the angle of attack is approximately 0.25.

3. Results and Discussions

The time-averaged velocity profile [Figs. 3(a) and (b)] were recorded at the peak-to-peak location (Fig. 1) and along the X - Y plane. Figure 3(a) shows the corresponding velocity profile, captured using Pitot tube, for a given X position. At a voltage V_p of 11 kV and frequency f of 11 kHz, the maximum velocity of about 2.64 m/s is obtained at $X = 5 \text{ mm}$ and $Y = 0.3 \text{ mm}$. Indeed, each maximum velocity is found close to the wall with Y ranging from 0.3 to 0.7 mm. The velocity gradually decreases with increasing Y due to the momentum diffusion from the plasma to the surrounding air. It is noteworthy that the momentum delivered to the surrounding air by the charged species at the peak-to-peak location is much greater than that of the trough-to-trough location, thus,

resulting an approximately two-dimensional induced flow in the X - Y plane. The effect of the applied voltage is investigated and presented in Fig. 3(b). It can be seen that the velocity increases from 0.96 to 3.33 m/s with the applied voltage ranging from 11 to 15 kV.

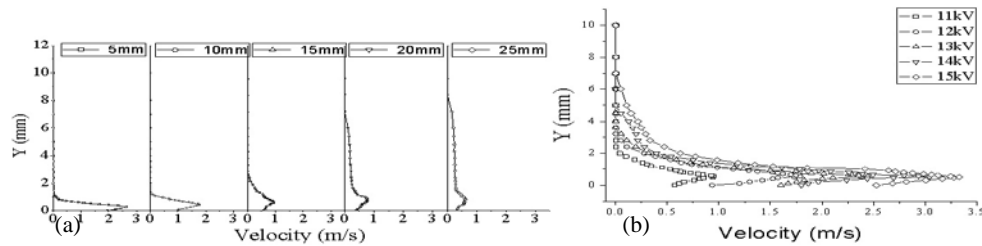


Fig. 3. (a) Velocity profiles at different X positions ($f = 11$ kHz, $V_p = 11$ kV); (b) Velocity profiles for different voltage amplitudes, at $X = 15$ mm ($f = 11$ kHz)

The PIV tests were conducted to observe the evolution of the vortex structures that originated from the PVG upon actuation. Figure 4 shows that the streamwise vortices are uniformly generated in Z direction. This is due to the serrated electrodes which locally varied the electric field, that vortices are generated on either side of each sharp peak. Based on the cross-correlation analysis, the maxima of ω_x of about ± 6201 s⁻¹ (not shown) was achieved at $X = 15$ mm. The presently identified streamwise vortices do not collide together, which differs from Refs. [21] and [24], thus avoiding substantial interactions between vortices, and the vortices could persist longer in the downstream locations. One can observe that the vortices lift away from the wall at X between 30 and 50 mm. This is attributed to the vortices from one pair begin to interact with the vortices from adjacent pairs, thus creating common-flow up configurations as seen in at $X = 50$ mm (Fig. 4).

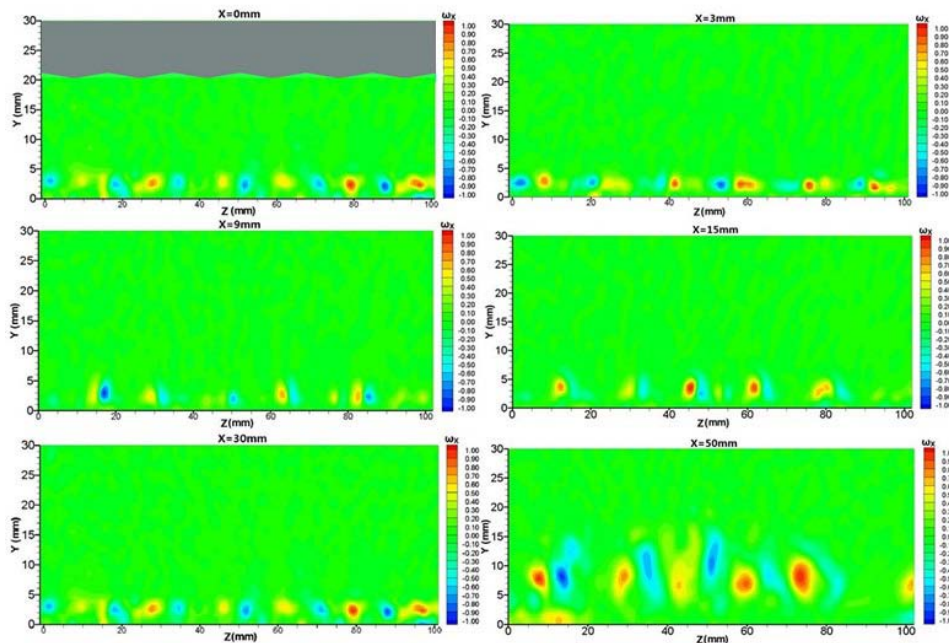


Fig. 4. Vorticity contours in the spanwise direction at different X positions ($f = 11$ kHz, $V_p = 11$ kV, $X = 0, 3, 9, 15, 30$ and 50 mm)

Due to the unique electric field between the serrated electrodes, the interaction exists between the streamwise vortices ejected out near the sharp peak of the electrode and the flow structure at the sharp peak location, thus forming small vortices close to the wall at the peak [Fig 5(a)]. On the other hand, the directed vortices at the trough show a maximum inducement angle of about 26° [Fig 5(b)]. One can observe clearly that the trains of vortices close to the wall, from $X = 20$ mm to 70 mm, are due to the Kelvin–Helmholtz (K - H) instability

generated by the directed vortices. It should be noted that the strength of the *K-H* instability is in an order similar, but opposite, to that of the directed vortices.

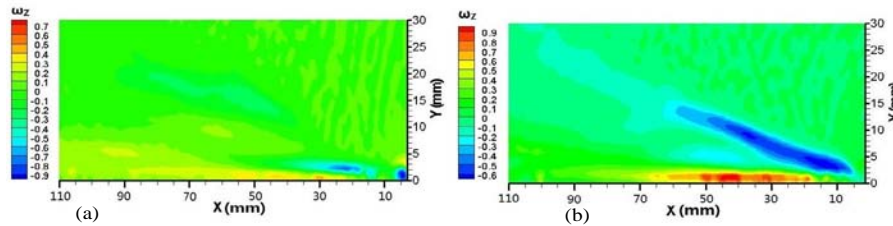


Fig. 5. Vorticity contours in the longitudinal direction ($f = 11$ kHz, $V_p = 11$ kV); (a) at the tip location; (b) at the trough location

The effect of the plasma vortex generator is shown in Fig. 6, in which lift and drag coefficients of the airfoil with actuation (i.e. V_p varies between 11 and 15 kV) are compared with those of the baseline airfoil (i.e. applied voltage V_p is zero). It is noteworthy that the slope in the lift drop determines the flow regime as discussed in Ref. [27], and by the reason thereof, the naturally developed boundary layer on the suction side of the NACA 0015 airfoil (i.e. baseline, $V_p = 0$) progresses from laminar to local separation then to turbulent reattachment (i.e. the laminar separation bubble) and finally to turbulent separation as confirmed by the lift coefficient C_l vs. angle-of-attack α curve in Fig. 6(a). It is evident that the PVG has a beneficial effect on the lift coefficient (Fig. 6a). The data indicated that the spanwise-orientated PVG along the span of the airfoil improves the lifting performance, reflected in the delay of stall angle and increase in the maximum lift coefficient of about 5 degrees and 6%, respectively. This is attributed to the mixing of high-momentum freestream fluid, induced by the counter-rotating vortex pairs, takes place toward the near wall region, and thus reattaches the flow. The C_l - α curve for the case of $V_p = 15$ kV demonstrates that the boundary layer changes from laminar to transition to turbulent, then separates at $\alpha = 18$ degrees. Note that the decrease in drag coefficient is significant for the case of $V_p = 15$ kV as revealed in Fig. 6(b). The result also suggests only small considerable benefits could be achieved at α less than the stall angle for V_p is between 11 kV and 13 kV. The cause of this could be related to the elimination of laminar separation bubble caused by the induced counter-rotating vortex pairs of the PVG, and as a result, the drag coefficient is reduced accordingly (Fig. 6b).

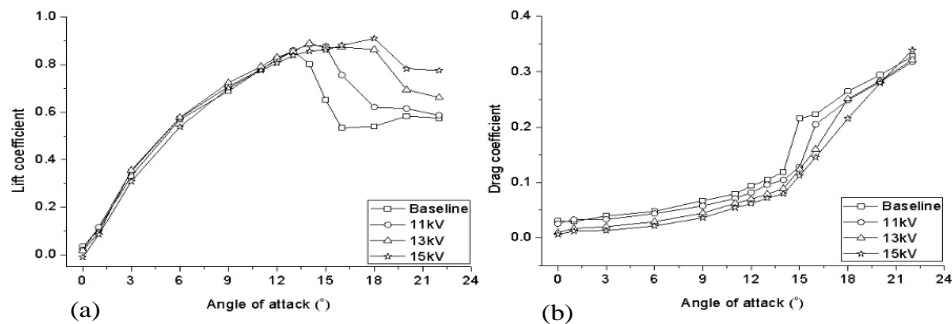


Fig. 6. (a) Lift coefficient versus angle-of-attack (V_p ranging from 11 to 15 kV); (b) Drag coefficient versus angle-of-attack (V_p ranging from 11 to 15 kV)

4. Conclusions

This paper focused on the study of plasma vortex generator PVG, which consists of two serrated electrodes, with the sharp peaks on each electrode facing opposite each other, and horizontally separated by a dielectric material, as well, the aerodynamics effect of a NACA 0015 airfoil with actuation and at $Re = 7.7 \times 10^4$.

In the absence of a free air stream, it can be clearly seen that the counter-rotating vortices are uniformly created in the spanwise direction. In addition, the streamwise vortices do not collide together, thus avoiding substantial interactions between vortices, and the vortices could persist longer in the downstream locations.

The results from the force measurements indicate that the spanwise-oriented plasma vortex generator brings high momentum fluid into the wall region in such a way that the maximum lift coefficient was increased by about 6%, while, at the same time, the stall angle was postponed from 13 to 18 degrees. Further experiments will be carried out in order to examine the flow structure of streamwise vortices and vortex pairs on the suction

side of the airfoil, which may be useful to improve the PVG design for flow separation control.

5. Acknowledgement

This work was supported by Natural Scientific Research Innovation Foundation in Harbin Institute of Technology (Grant No. HIT.NSRIF.2013098), and Shenzhen Government (Grant No. JC201105160543A).

6. References

- [1] G.I. Font, "Boundary Layer Control with Atmospheric Plasma Discharges", *AIAA Journal*, Vol. 44, No. 7, pp. 1572-1578, 2006.
- [2] T.N. Jukes, K.S. Choi, G.A. Johnson, and S.J. Scott, "Characterization of Surface Plasma-Induced Wall Flows Through Velocity and Temperature Measurements", *AIAA Journal*, Vol. 44, No. 4, pp. 764-771, 2006.
- [3] C.L. Enloe, T.E. McLaughlin, R.D. VanDyken, K.D. Kachner, E.J. Jumper, and T.C. Corke, "Mechanisms and Responses of a Single Dielectric Barrier Plasma Actuator: Plasma Morphology", *AIAA Journal*, Vol. 42, No. 3, pp. 589-594, 2004a
- [4] C.L. Enloe, T.E. McLaughlin, R.D. VanDyken, K.D. Kachner, E.J. Jumper, and T.C. Corke, "Mechanisms and Responses of a Single Dielectric Barrier Plasma Actuator: Geometric Effects", *AIAA Journal*, Vol. 42, No. 3, pp. 595-605, 2004b.
- [5] E. Moreau, "Airflow Control by Non-thermal Plasma Actuators", *Journal of Physics D: Applied Physics*, Vol. 40, No. 3, pp. 605-636, 2007.
- [6] C. Wong, and K. Kontis, "Flow Control by Spanwise Blowing on a NACA 0012", *Journal of Aircraft*, Vol. 44, No. 1, pp. 337-340, 2007.
- [7] C. Wong, and K. Kontis, "Pneumatic Flow Control Studies Using Steady Blowing on a Supercritical Aerofoil", *The Aeronautical Journal*, Vol. 113, No. 139, pp. 53-63, 2009.
- [8] M.B. Bragg, and G.M. Gregorek, "Experimental Study of Airfoil Performance with Vortex Generators", *Journal of Aircraft*, Vol. 24, No. 5, pp. 305-312, 1987.
- [9] K. Rinoie, M. Okuno, and Y. Sunada, "Airfoil Stall Suppression by Use of a Bubble Burst Control Plate", *AIAA Journal*, Vol. 47, No. 2, pp. 322-330, 2009.
- [10] J.R. Roth, D.M. Sherman, and S.P. Wilkinson, "Boundary Layer Flow Control with a One Atmosphere Uniform Glow Discharge Surface Plasma", AIAA Paper 98-0328, 1998.
- [11] T. Corke, E. Jumper, M.L. Post, D. Orlov, and T. McLaughlin, "Application of Weakly-Ionized Plasmas as Wing Flow-Control Devices", AIAA Paper 02-0350, 2002.
- [12] J. Huang, T. Corke, and F. Thomas, "Plasma Actuators for Separation Control of Low Pressure Turbine Blades," AIAA Paper 03-1027, 2003.
- [13] M.L. Post, and T. Corke, "Separation Control on High Angle of Attack Airfoil Using Plasma Actuators," *AIAA Journal*, Vol. 42, No. 11, pp. 2177-2184, 2004.
- [14] B. Goeksel, I. Rechenberg, D. Greenblatt, and C.O. Paschereit, "Steady and Unsteady Plasma Wall Jets for Separation and Circulation Control," AIAA Paper 06-3686, 2006.
- [15] H. Chuan, T.C. Corke, and M.P. Patel, "Plasma Flaps and Slats: An Application of Weakly Ionized Plasma Actuators", *Journal of Aircraft*, Vol. 46, No. 3, pp. 864-873, 2009.
- [16] T.C. Corke, M.L. Post, and D.M. Orlov, "SDBD Plasma Enhanced Aerodynamics: Concepts, Optimization and Applications", *Progress in Aerospace Sciences*, Vol. 43, Nos. 7-8, pp. 193-217, 2007.
- [17] T.C. Corke, C.L. Enloe, and S.P. Wilkinson, "Dielectric Barrier Discharge Plasma Actuators for Flow Control," *Annual Review of Fluid Mechanics*, Vol. 42, pp. 505-529, 2010.
- [18] F.O. Thomas, T.C. Corke, M. Iqbal, A. Kozlov, and D. Schatzman, "Optimization of Dielectric Barrier Discharge Plasma Actuators for Active Aerodynamic Flow Control", *AIAA Journal*, Vol. 47, No. 9, pp. 2169-2178, 2009.
- [19] M. Forte, J. Jolibois, J. Pons, E. Moreau, G. Touchard, and M. Cazalens, "Optimization of a Dielectric Barrier Discharge Actuator by Stationary and Non-Stationary Measurements of the Induced Flow Velocity: Application to Airflow Control", *Experiments in Fluids*, Vol. 43, No. 6, pp. 917-928, 2007.
- [20] A. Berendt, J. Podliński, and J. Mizeraczyk, "Comparison of Airflow Patterns produced by DBD Actuators with Smooth or Saw-Like Discharge Electrode", *Journal of Physics: Conference Series*, Vol. 301, 012018, 2011.
- [21] Z. Liu, L. Wang, and S. Fu, "Study of Flow Induced by Sine Wave and Saw Tooth Plasma Actuators", *Science China: Physics, Mechanics and Astronomy*, Vol. 54, No. 11, pp. 2033-2039, 2011.
- [22] N. Balcon, N. Benard, Y. Lagmich, J.P. Boeuf, G. Touchard, and E. Moreau, "Positive and Negative Sawtooth Signals applied to a DBD Plasma Actuator - Influence on the Electric Wind", *Journal of Electrostatics*, Vol. 67, No. 2-3, pp. 140-145, 2009.
- [23] C.C. Wang, R. Durscher, and S. Roy, "Three-Dimensional Effects of Curved Plasma Actuators in Quiescent Air", *Journal of Applied Physics*, Vol. 109, 083305, 2011.
- [24] R. Joussot, A. Leroy, R. Weber, H. Rabat, S. Loyer and D. Hong, "Plasma Morphology and Induced Airflow Characterization of a DBD Actuator with Serrated Electrode" *Journal of Physics D: Applied Physics*, Vol. 46, 125204, 2013.
- [25] R. Durscher, and S. Roy, "Three-Dimensional Flow Measurements Induced from Serpentine Plasma Actuators in Quiescent Air", *Journal of Physics D: Applied Physics*, Vol. 45, 035202, 2012.
- [26] T.N. Jukes, and K.S. Choi, "Dielectric-Barrier-Discharge Vortex Generators: Characterisation and Optimisation for Flow Separation Control, *Experiments in Fluids*, Vol. 52, pp. 329-345, 2012.
- [27] M.P. Patel, Z.H. Sowle, T.C. Corke, and C. He, "Autonomous Sensing and Control of Wing Stall using a Smart Plasma Slat", *Journal of Aircraft*, Vol. 44, No. 2, pp. 516-527, 2007.

Hydrodynamic analysis of wave impact forces and overturning moment on monopile foundations of offshore wind turbines

Md. Shahidul Islam¹ and Gazi Md. Khalil¹

¹Department of Naval Architecture and Marine Engineering
Bangladesh University of Engineering and Technology, Dhaka-1000
E-mail: shahid777@name.buet.ac.bd

Abstract

Renewable energy is that form of energy which is extracted from nature. Sunlight, wind, ocean waves etc. are the sources of renewable energy. The term renewable is used as this energy is naturally replenished. For this very reason, in recent times renewable energy has attracted a great deal of attention among academicians, industrialists and governments all over the world. Wind energy is at present the fastest growing renewable energy worldwide. Wind turbines are used to extract energy from wind. As offshore winds are less turbulent and they tend to flow at higher speeds than onshore winds, the offshore turbines produce more electricity. These turbines are supported by monopile foundations. As these structures are under constant wave action, the finding out of the wave impact loads and overturning moments on these structures is very important for proper design and installation of the same. In this paper the small amplitude wave theory is used to analyze the wave impact forces acting on a monopile foundation of an offshore wind turbine. Based on the aforesaid analysis a computer program has been developed in order to compute the drag force, the inertia force, the total force and total moment on a typical monopile foundation.

Keywords: Monopile, Offshore Wind Turbine, Linear Wave Theory, Drag Force, Inertia Force.

1. Introduction

Wind has been established in modern times as a source of renewable energy to generate electricity free from pollution through the use of wind turbines. A wind turbine (Fig. 1) can be compared to a fan operating in reverse. Rather than using electricity to produce wind, the turbine uses the wind to generate electricity. Wind flows over the airfoil-shaped blades of wind turbines and generates lift force which makes the turbine blades to turn. The blades are connected to a shaft that turns an electric generator to produce electricity. Wind turbines are used to harness the kinetic energy of the moving air over the oceans and convert it to electricity.



Fig. 1. Offshore wind turbines (Source: University of Cambridge)

In 2010 the wind power capacity increased more than 24% relative to 2009, with total global capacity nearing 198 GW by year's end. At least 52 countries increased their total existing capacity during 2010, and 83

countries now use wind power on a commercial basis. Over the period from end-2005 to end-2010, annual growth rates of cumulative wind power capacity averaged 27% [1].

Offshore winds are less turbulent and they tend to flow at higher speeds than onshore winds, thus allowing turbines to produce more electricity. Offshore wind turbines are usually supported by monopiles. Monopile structures provide the benefit of simplicity in fabrication and installation. It is a single column structure, consisting of a vertical circular cylinder. Such a structure is sometimes also used in offshore engineering to host some simple facilities such as a loading terminal and a light or radio instruments for navigation.

If one encounters a random offshore wind turbine there is a two-third probability that it will be supported by a monopile. The giant steel pipe is by far the most popular support structure in the world. At the dawn of 2011, 889 of the world's 1318 offshore wind turbines used monopiles for support.

However, the simple shape also calls for a large diameter of the monopile – ranging from 3.5 to 6.0 meters. As a result, the structure invites high hydrodynamic loads from the water waves – the water pushes and pulls the monopile and this affects the structure much more than for instance a jacket constructed out of smaller tubes. That is why the wave load analysis of these structures is very important.

A number of researchers have worked on wave impact loads on slender circular structure used for supporting the wind turbines. Goda [2] proposed a model for the impact force by considering the breaking wave as a vertical wall of water hitting the cylinder with wave celerity. Wienke *et al.* [3] developed theoretical formulae for the load due to breaking wave impact on slender piles based on large scale experiments. The load distribution in time and space was given by the proposed theoretical three dimensional impact model. The formulae were applied to calculate the impact force on a support tower of a wind turbine subjected to breaking wave. Corte and Grilli [4] studied the impact on cylindrical piles of extreme waves (freak waves), generated by directional wave focusing. Waves were numerically modeled based on a boundary element discretization of fully nonlinear potential flow equations with free surface evolution. Higher-order boundary elements were used for the spatial discretization, and a higher-order time integration scheme based on the Taylor series expansion was applied. Finally, the full loading on a cylindrical tower structure, due to a freak wave, was determined. Some other contributory researchers in this field are Ferro and Mansour [5], Arai and Matsunaga [6], Basco and Niedzwecki [7], Matthies *et al.* [8] etc.

In this paper the small amplitude wave theory is used to analyze the wave impact forces acting on a monopile foundation of an offshore wind turbine. Based on the aforesaid analysis a computer program has been developed in order to compute the drag force, the inertia force and the total force on a typical monopile foundation. The computational results are plotted and physically interpreted.

2. Mathematical formulation

This section presents a theoretical analysis of the wave forces acting on a monopile foundation of an offshore wind turbine. The analysis is based on the linear wave theory.

Fig. 2 shows a model of a cylinder, in this case, a monopile, on which incident wave is impinging. In this Fig. the mean water level represents X axis and the vertical axis from mean water level is Z . The wave height is H , instantaneous wave height is η , wave length L and depth of water is d . The diameter of the cylinder is D . The total in-line wave load for unit height of monopile at a depth $z + d$ for an accelerated water environment where the cylinder is held stationary is given by

$$F_T = \frac{1}{2} \rho C_D D U |U| + \rho C_m A \dot{U} + \rho A \ddot{U} \quad (1)$$

where F_T is the total force per unit length of the cylinder, ρ the fluid density, C_D the drag coefficient, C_m the hydrodynamic mass coefficient, U is horizontal wave induced velocity of water and \dot{U} is the horizontal wave induced acceleration of water and A is the cross sectional area of the cylinder [9].

On the right hand side of Equation number (1), the first term represents drag force, the second term the hydrodynamic mass force and the third term the Froude-Krylov force. The Froude-Krylov force is caused by the acceleration of the fluid in the immediate surroundings of the body.

equation number (1) can be written in the following form:

$$F_T = \frac{1}{2} \rho C_D D U |U| + \rho (C_m + 1) A \ddot{U} \quad (2)$$

Defining a new coefficient, C_M , as

$$C_M = C_m + 1 \quad (3)$$

Equation number (2) becomes

$$F_T = \frac{1}{2} \rho C_D D U |U| + \rho C_M A \dot{U} \quad (4)$$

Equation number (4) is known as the Morison equation [10]. The new force term, $\rho C_M A \dot{U}$, is called the inertia force and the new coefficient C_M is called the inertia coefficient.

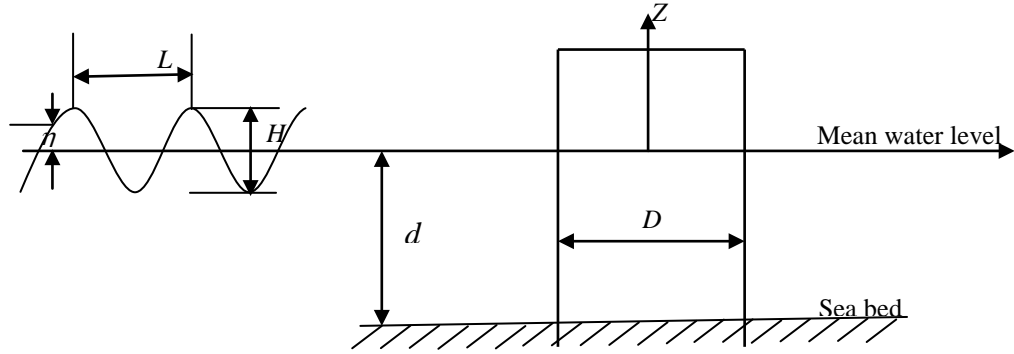


Fig. 2. Definition sketch of a circular cylinder on which incident wave is impinging.

The drag and inertia coefficients are in general functions of the Reynolds number, the Keulegan-Carpenter number and the relative roughness. The coefficients also depend on the cross-sectional shape of the structure and of the orientation of the body.

The Reynolds number (Re) and the Keulegan-Carpenter number (KC) are calculated using the following expressions:

$$\left. \begin{aligned} Re &= \frac{U_{\max} D}{\nu} \quad \text{and} \\ KC &= \frac{U_{\max} T}{D} \end{aligned} \right\} \quad (5)$$

where U_{\max} is the maximum horizontal velocity of water at still water level, ν is the kinematic viscosity of seawater, and T is the period of the waves. The drag coefficient C_{DS} for steady-state flow can be used as a basis for calculation of C_D and C_M [11].

The potential function for a small amplitude progressive wave is

$$\phi = \frac{HC}{2} \frac{\cosh m(z+d)}{\sinh md} \sin(mx - nt) \quad (6)$$

where C is the wave celerity, m is the wave number and n is the wave frequency [12].

$$\left. \begin{aligned} C &= \frac{L}{T} \\ m &= \frac{2\pi}{L} \\ \text{and} \\ n &= \frac{2\pi}{T} \end{aligned} \right\} \quad (7)$$

The well known expression for wave celerity is

$$C^2 = \frac{g}{m} \tanh md \quad (8)$$

where g is the gravitational acceleration.

From equation numbers (7) and (8), we obtain

$$L = \frac{gT^2}{2\pi} \tanh \frac{2\pi d}{L} \quad (9)$$

The horizontal velocity of the water particle is

$$U = \frac{\partial \phi}{\partial x} = \frac{HCm}{2} \frac{\cosh m(z+d)}{\sinh md} \cos(mx - nt) \quad (10)$$

From equation numbers (7) and (10), we get

$$U = \frac{\pi H}{T} \frac{\cosh m(z+d)}{\sinh md} \cos(mx - nt) \quad (11)$$

The horizontal acceleration of the water particle is

$$\dot{U} = \frac{\partial U}{\partial t} = \frac{2\pi^2 H}{T^2} \frac{\cosh m(z+d)}{\sinh md} \sin(mx-nt) \quad (12)$$

The term $(mx-nt)$ in equation numbers (11) and (12) is called the phase angle.

Let

$$mx - nt = \theta \quad (13)$$

Thus equation (11) and equation (12) can be written as

$$U = \frac{\pi H}{T} \frac{\cosh m(z+d)}{\sinh md} \cos \theta \quad (14)$$

and

$$\dot{U} = \frac{2\pi^2 H}{T^2} \frac{\cosh m(z+d)}{\sinh md} \sin \theta \quad (15)$$

From equation number (4), the expression of drag force can be written as

$$F_D = \frac{1}{2} \rho C_D D U |U| \quad (16)$$

Combining equations (14) and (16), we get

$$F_D = \frac{1}{2} \rho C_D D \left(\frac{\pi H}{T} \frac{\cosh m(z+d)}{\sinh md} \cos \theta \right) \left| \frac{\pi H}{T} \frac{\cosh m(z+d)}{\sinh md} \cos \theta \right| \quad (17)$$

From equation number (4), the inertia force can be expressed as

$$F_I = \rho C_M A \dot{U} \quad (18)$$

Combining equation numbers (15) and (18), we get

$$F_I = \rho C_M A \left(\frac{2\pi^2 H}{T^2} \frac{\cosh m(z+d)}{\sinh md} \sin \theta \right) \quad (19)$$

Let the submerged length of the monopile be s .

$$\therefore s = z + d \quad (20)$$

The total horizontal force over the submerged length of the monopile foundation F_{ST} can be found by integration of Morison's equation for values of s from 0 to the instantaneous wave height from the seabed $(d+\eta)$.

$$F_{ST} = \int_0^{d+\eta} \frac{1}{2} \rho C_D D U |U| ds + \int_0^{d+\eta} \rho C_M A \dot{U} ds \quad (21)$$

The instantaneous wave height can be expressed as

$$\eta = \frac{H}{2} \cos(mx-nt) \quad (22)$$

For simplicity, let the monopile be located at $x = 0$. Then we get

$$\left. \begin{aligned} \theta &= mx - nt = -nt \\ \eta &= \frac{H}{2} \cos nt \\ U &= \frac{\pi H}{T} \frac{\cosh m(z+d)}{\sinh md} \cos nt \\ \text{and} \\ \dot{U} &= -\frac{2\pi^2 H}{T^2} \frac{\cosh m(z+d)}{\sinh md} \sin nt \end{aligned} \right\} \quad (23)$$

Combining equation numbers (20), (21) and (23), we get

$$F_{ST} = \int_0^{d+\eta} \frac{1}{2} \rho C_D D \left(\frac{\pi H}{T} \right)^2 \cos nt |\cos nt| \frac{\cosh^2 ms}{\sinh^2 md} ds - \int_0^{d+\eta} \rho C_M A \left(\frac{2\pi^2 H}{T^2} \right) \sin nt \frac{\cosh ms}{\sinh md} ds \quad (24)$$

Using the well known relationship $n^2 = mg \tanh md$ and integrating equation (24), we get

$$F_{ST} = \frac{1}{8} \rho C_D D H^2 g m d \frac{\cos nt |\cos nt|}{\sinh 2md} \left[\frac{1}{2md} \sinh 2md \left(1 + \frac{\eta}{d} \right) + \left(1 + \frac{\eta}{d} \right) \right] - \frac{1}{8} \rho C_M \pi D^2 g H \frac{\sin nt}{\cosh md} \left[\sinh md \left(1 + \frac{\eta}{d} \right) \right] \quad (25)$$

The total moment about the ocean floor is derived as

$$M_T = \int_0^{d+\eta} s dF_T \quad (26)$$

and if the integration is carried out,

$$M_T = \frac{1}{8} \rho C_D D H^2 d g m d \frac{\cos nt |\cos nt|}{\sinh 2md} \left[\frac{\left(1 + \frac{\eta}{d} \right)^2}{2} + \frac{\left(1 + \frac{\eta}{d} \right)}{2md} \sinh 2md \left(1 + \frac{\eta}{d} \right) + \frac{1}{(2md)^2} \left(1 - \cosh 2md \left(1 + \frac{\eta}{d} \right) \right) \right] - \frac{1}{8} \rho C_M \pi D^2 H d g \frac{\sin nt}{\cosh md} \left[\left(1 + \frac{\eta}{d} \right) \sinh md \left(1 + \frac{\eta}{d} \right) + \frac{1}{md} \left(1 - \cosh md \left(1 + \frac{\eta}{d} \right) \right) \right] \quad (27)$$

Equation numbers (25) and (27) are valid for both deep and shallow water waves.

3. Results and discussion

In order to demonstrate the actual calculation procedure, a typical monopile foundation of 5 m diameter (D) at a location of 25 m water depth (d) is chosen. The following metocean data is considered for the calculation.

Table 1. Metocean data for calculating wave load on monopile foundation

Parameter	Values
Wave height, H (m)	8.0
Wave period, T (sec)	9.4
Mass density of sea water, ρ (kg/m ³)	1025

The wave length L is calculated as 119.4 m by trial and error method using Equation (12). We get the value of C_{DS} as 0.65 for smooth steel pipe.

Fig. 3 (a) shows the variation of drag force (F_D), inertia force (F_I) and total force (F_T) with the phase angle (θ). Equation numbers (4), (17) and (19) are used to plot this figure. It is observed that the variation of the drag force is not a sinusoidal one. The maximum drag force (18447.43 N) occurs at 0 and 360 degrees and minimum force (-18447.43 N) at 180 and 540 degrees. It is interesting to note that the variation of inertia force is sinusoidal. The maximum and minimum values are ± 91199.09 N. The maximum inertia force occurs at θ equal to 90 and 450 degrees whereas the minimum inertia force occurs at θ equal to 270 and 630 degrees. It is observed that the variation of the total force is represented by a curve which is nearly sinusoidal. This can be easily understood from the fact that the inertia force is much greater than the drag force and there is a phase difference of 90 degrees between these two components of the total wave force.

Equation number (25) is used for plotting Fig. 3(b). The total horizontal force over the submerged length of the monopile foundation (F_{ST}) and its two components (drag force and inertia force) are varied with non-dimensional time (t/T). It is to be noted that the inertia force component is negative in equation number (25). It is seen that the maximum total horizontal force over the submerged length of the monopile foundation occurs at $t/T = 0.8$. The inertia force is much greater than the drag force and there is a phase difference of 90 degrees between these two components of the total wave force.

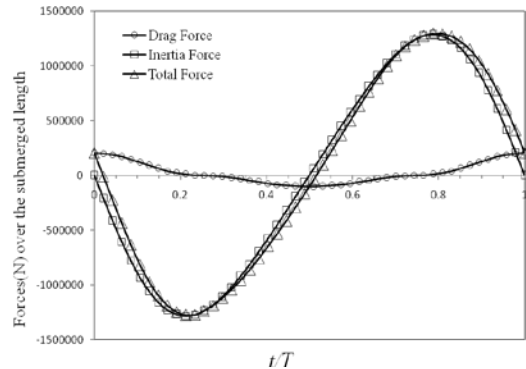
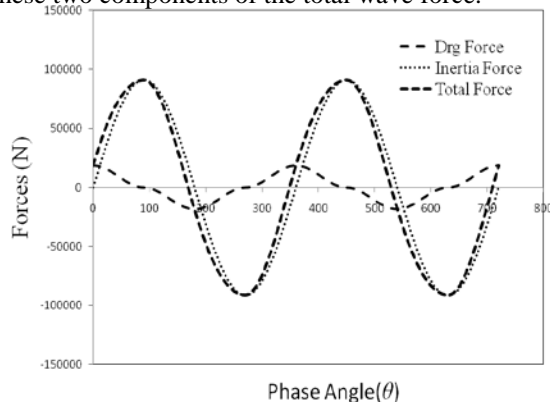


Fig. 3. Variation of forces with phase angle (θ) and non-dimensional time (t/T)

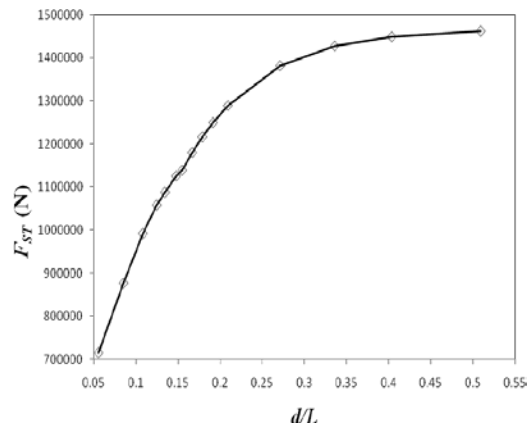


Fig. 4. Variation of total horizontal force (F_{ST}) with relative depth (d/L)

The relative depth is defined as the ratio of depth of water to the wave length (d/L). Fig. 4 shows the variation of the total horizontal force (F_{ST}) with relative depth. It is observed that F_{ST} increases almost linearly up to $d/L = 0.3$ and then the rate of increase is somewhat lower.

4. Conclusions

This paper presents a hydrodynamic analysis of the wave impact forces on the monopile foundation of an offshore wind turbine. The following conclusions can be drawn from the present work:

1. The linear wave theory is used to calculate the drag force (F_D), inertia force (F_I) and total force (F_T) acting on a monopile foundation.
2. The inertia force (F_I) component is much larger than the drag force component (F_D).
3. The variation of the drag force (F_D) with the phase angle (θ) is not sinusoidal whereas the variation of the inertia force (F_I) with the phase angle (θ) is sinusoidal.
4. The variation of the total force (F_T) with the phase angle (θ) is nearly sinusoidal.
5. The total horizontal force over the submerged length of the monopile foundation is maximum when inertia force component is maximum.
6. The relative depth (d/L) has a great influence on the magnitude of the total horizontal force (F_{ST}). It is observed that (F_{ST}) increases almost linearly up to $d/L = 0.3$ and then the rate of increase is somewhat low.

5. References

- [1] REN21 "Renewables 2011 (Global Status Report)", *REN21 Secretariat*, France, 2011.
- [2] Y. Goda, "Wave forces on a vertical circular cylinder: Experiments and a proposed method of wave force computation", *Report No. 8, Port and Harbour Technical Research Institute*, 1964.
- [3] J. Wienke, U. Sparboom, and H. Oumeraci, "Theoretical formulae for wave slamming loads on slender circular cylinders and application for support structures of wind turbines", *ICCE-2004*.
- [4] C. Corte, and S.T. Grilli, "Numerical modeling of extreme wave slamming on cylindrical offshore support structures", *Proceedings of the Sixteenth International Offshore and Polar Engineering Conference, San Francisco, California, USA*, 2006.
- [5] G. Ferro, and A.E. Mansour, "Probabilistic analysis of the combined slamming and wave induced responses", *JSR*, Vol. 29, 1985.
- [6] M. Arai, and K. Matsunaga, "A numerical and experimental study of bow flare slamming", *Journal of Society of Naval Arch. Japan*, PP. 343-353, 1989.
- [7] D.R. Basco, and J.M. Niedzwecki, "Breaking wave force distributions and design criteria for slender piles", *Offshore Technology Conference, OTC*, pp. 425-431, 1989.
- [8] H.G. Matthies, C. Nath, T.E. Schellin, A.D. Garrard, M.A. Wastling, D.C. Quarton, J. Wei, M. Scherweit, and T. Siebers, "Study of Offshore Wind Energy in the EC", *Verlag Natürliche Energie, Brekendorf*, 1995.
- [9] B.M. Sumer, and J. Fredsoe, "Hydrodynamics around cylindrical structures", *World Scientific*, pp. 130-131, 1997.
- [10] J.R. Morison, M.P. O'Brien, J.W. Johnson, and S.A. Schaaf, "The forces exerted by surface waves on piles. Journal of Petroleum Technology", *Petroleum Transactions, AIME, (American Inst. Mining Engineers)*, pp. 149-154, 1950.
- [11] Det Norske Veritas, "Offshore Standard DNV-OS-J101 (Design of Offshore Wind Turbine Structures)", *Det Norske Veritas*, 210.
- [12] A.T. Ippen, "Estuary and Coastline Hydrodynamics", *Mcgraw-Hill book company, Inc*, pp. 21-29, 1966.

Effect of Roughness Height on the Turbulence Models for Ahmed Car Body Simulation

Abul Kalam Azad¹, Mohammad Arif Hossain¹, AKM Sadrul Islam²

¹Department of Mathematics, Khulna University of Engineering & Technology, Khulna-9203, Bangladesh

²Department of Mechanical and Chemical Engineering, Islamic University of Technology, Dhaka, Bangladesh

E-mail: arifhkhann63@hotmail.com

Abstract

Effects of roughness height over various turbulence models are important for the computational simulation. To know the position of the point of separation of the recirculation, its behaviour and swirling structure around the vehicle we depend on turbulence models. But efficiency of turbulence models partly depends on the roughness height. In this study comparison between the turbulence models $k-\epsilon$ and RNG $k-\epsilon$ is done on the basis of their impact on the coefficient of drag over Ahmed car body. In the simulations all geometric quantities of Ahmed body are normalized with the body height. The channel length is about 8.8069 times of the length of the body and the blockage is about 4.27%. ANSYS-11 software is used for CFD analysis. In these simulations five roughness heights 0.0001m, 0.0002m, 0.0003m, 0.0004m and 0.0005m are used with the bulk air velocity 40m/s. The obtained drags are compared with the experimental values of LSTM.

Keywords: Turbulence models, roughness height, CFD and aerodynamics.

1. Introduction

Turbulence are of great importance in computational fluid dynamics. The understanding of the physics of turbulence is crucial and many different models have evolved to explain them. Sometimes the turbulence models are validated through vehicle aerodynamics. Computers have been used to solve fluid flow problems for many years. Numerous programs have been written to solve either specific problems, or specific classes of problems. From the mid-1970's, the complex mathematics required to generalize the algorithms began to be understood, and general purpose computational fluid dynamics (CFD) solvers were developed. Recent advances in computing power, together with powerful graphics and interactive 3D manipulation of models have made the process of creating a CFD model and analyzing results much less labor intensive, reducing time and, hence, cost. Advanced solvers contain algorithms which enable robust solutions of the flow field in a reasonable time.

A real-life automobile is a very complex shape to model or to study experimentally [1]. Because of the complexity of cars aerodynamics and in order to simplify studies Ahmed car body has become reference geometry (Montinat et al.,2008)[2]. The vehicle shape employed by Ahmed and Ramm (1984) is known as Ahmed body[3]. Several researchers have worked on the experiments and numerical modeling of the flow over the Ahmed body. Lienhart et al.,2000 conducted the experiments for two near slant angles (25° , 35°) at LSTM at Erlangen university, Germany. Craft et al. 2001 compared the performance of linear and non-linear $k-\epsilon$ model with two different wall functions. A dimensionless coefficient, Called drag coefficient and related to the drag force acting on the bluff body but the drag coefficient and turbulence are related to the roughness height [4]. In most CFD program a standard roughness height is need to set. But if we take much rough surface like sand grain size, we need to modify the wall function for the turbulence model with the more active roughness height. Flow over rough surface has significant importance in industrial application but much less knowledge is available for flow over rough surface. In this study comparison is done among the drag coefficients at different roughness heights over the Ahmed body for $k-\epsilon$ and RNG $k-\epsilon$ turbulence models. Velocity 40 m/s is taken in these simulations.

2. Description

The geometry of body is shown in Fig.1(a,b). All the geometric quantities are normalized with the body height $H=0.288\text{m}$. The values of the geometric quantities are $l_r/H=2.928$, $G/H=0.697$ and $W/H=1.35$, where l_r is the

length from the beginning of the slant to the front, G is the length of the slant region and W is the width of the body. The front part is rounded with a radius of $R/H=0.347$ in the plane, $y=0$ and $z=0$. The body is placed in the channel with a cross section of $B \times F=6.493H \times 4.861H$ (width \times height). The front face of the body is located at a distance of $7.3H$ from the channel inlet and the downstream length between the rear face of the body and the channel outlet is $21H$. The body is lifted from the floor, producing a ground clearance of $C/H=0.174$ on the four pillars. The slant angle is taken as 25° . As a result the channel length is about 8.8069 times of the body length and the blockage is about 4.27%.

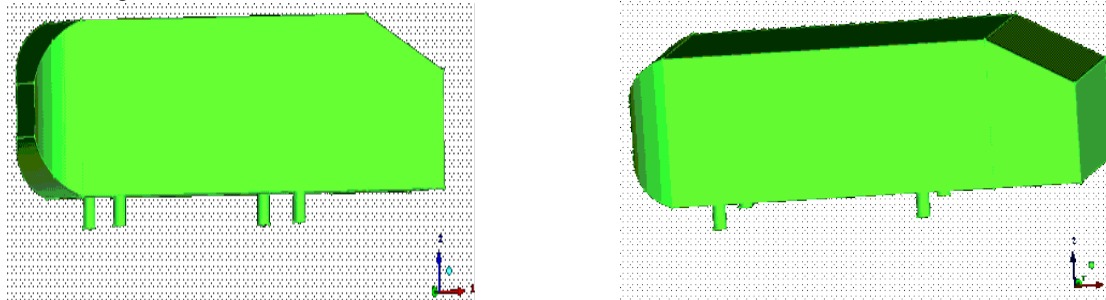


Fig. 1(a, b)- Geometric presentation of the body from different angle.

In the simulations Ansys 11[®] with high resolution advection scheme along with Physical timescale (physical time = length of the tunnel/velocity of the fluid) is used. The following conditions are used as simulation parameters.

Simulation type :	Stationary	Boundary condition and numerical scheme:	
Domain type	Fluid domain	Inlet:	
Fluid	Air at 25°C	Flow region	Subsonic
Buoyancy	Buoyant	Turbulence	Low(intensity1%)
Reference pressure	1 [atm]	Temperature	298K
Gravity-	X= 0	Outlet:	
	Y= 0	Flow region	Subsonic
	Z= -9.807m/s ²	Static pressure	0 Pa
Buoyancy reference temperature	298K	Wall:	
Domain motion	Stationary	Wall influence on flow	No slip
Heat transfer option	Isothermal	Wall roughness	Rough wall
Wall function	Scalable	Roughness height	0.0001- 0.0005m
Buoyancy turbulence	Production and dissipation	Fixed temperature	298K

3. Turbulence Modeling

Generating turbulence information by solving the full Navier–Stokes equations remains incomplete at the time. Instead, analysts resort to approximate approaches, called as modeling. Turbulence modeling is based on the assumption that the real flow field may be substituted by an imaginary field of mathematically defined continuous functions. These functions usually represent physical quantities measurable in the flow field. Many turbulence modeling techniques deal with approximation to the Navier-Stokes or Reynolds-Stress equations. Any model, up to some extent can be analytically derived from Reynolds- stress equations. The main goals of turbulence modeling are: develop a set of constitutive relations valid for any general turbulent flow problem; yield sufficiently reliable answers and offer a degree of universality sufficient to justify their usage in comparison to cheaper, less general methods or to more expensive but potentially more reliable methods.

Early work on modeling turbulence was attracted by Newton’s law of viscosity. An eddy viscosity a new property of turbulence was introduced and specified for different turbulent flows. Many simple models based on the eddy viscosity concept, particularly Prandtl mixing length models were developed to predict the mean velocity profiles in turbulent flows. These models continue to be in use because of their simplicity and sufficient accuracy in determining global quantities such as boundary-layer thickness, wall shear stress and point of separation. Uses of these models produce analytical solutions for many simple engineering problems. Advanced engineering applications require identification of structures of structures and calculation of statistical parameters, spectral functions, Reynolds stress distribution and turbulence heat and mass flux distributions. The model that must then be selected depends on the level of detail to be captured by the solution.

The k-epsilon model

Jones and Launder [5] developed the k-ε turbulence model in 1972. The k-ε turbulence model predicts the kinematic eddy viscosity value through the modeling of the turbulence velocity and length scale. This is achieved by solving additional transport equation of mean turbulent kinetic energy (velocity scale) and dissipation rate (length scale) and thus it falls in the category of two equation model. Here k is the turbulence kinetic energy and is defined as the variance of the fluctuations in velocity and has dimension of L^2T^{-2} , and ε is the turbulence eddy dissipation (the rate at which the velocity fluctuations dissipate) and has dimensions of k per unit time (L^2T^{-3}). The model has shown its robust and economical properties but has deficiencies to predict highly strained flow, swirling flow, rotating and separating flows.

The RNG k-epsilon model

The RNG k-ε turbulence model provides with accuracy and efficiency in the modeling of turbulent flow. This model follows the two equation turbulence modeling framework and has been derived from the original governing equations for fluid flow using mathematical techniques called Renormalization Group (RNG) method due to Yakhot and Orszag [6]. The RNG model provides a more general and fundamental model and yield improved prediction of near wall flows, separated flows, flows in curved geometries and flows that are strained by effects such as impingement or stagnation. Time dependent flows with large-scale motions, as in turbulent vortex shedding are far better predicted by RNG k-ε turbulence model.

4. Roughness height and Drag coefficient

Roughness height: The roughness height is the height of the surface irregularities for uniform sand grain roughness, or a mean height value for non-uniform sand-grain roughness. All surfaces in technical applications like the surface of a car are rough with a deviation in roughness height. We have it even for very smooth surface. In most CFD program a standard roughness is set. But if we have a much rough surface like sand corn size we have to modify the wall functions for the turbulence model with the right roughness height.

Drag coefficient: The drag experienced by a plate is purely friction drag. This can easily be determined from the equation given below.

$$D = b \int_0^l \tau_w(x) dx \quad (1)$$

From the equation (1) we get the drag of one side of the plate, where b is the width of the plate and l its length. Now the local wall shear stress is

$$\tau_w(x) = \mu \left(\frac{\partial u}{\partial y} \right)_w = \mu U_\infty \sqrt{\frac{U_\infty}{2\nu x}} f_w'' = 0.332 \mu U_\infty \sqrt{\frac{U_\infty}{\nu x}} \quad (2)$$

where f_w'' is the characteristic value for the boundary layer on a flat plate at zero incidence. The skin-friction coefficient in the equation

$$C_f(x^*) = \frac{2\tau_w(x^*)}{\rho V^2} \quad (3)$$

With the reference velocity U_∞ then becomes

$$C_f(x) = \frac{2\tau_w(x)}{\rho U_\infty^2} = \frac{0.664}{\sqrt{\text{Re}_x}} \quad (4)$$

Where the following form of the Reynolds number formed with the length x has been used:

$$\text{Re}_x = \frac{U_\infty x}{\nu} \quad (5)$$

Combining equation (1) and (2) we find the drag on one side of the plate;

$$D = f_w'' \mu b U_\infty \sqrt{\frac{U_\infty}{2\nu}} \int_0^l \frac{dx}{\sqrt{x}} = f_w'' b U_\infty \sqrt{2\mu \rho l U_\infty} \quad (6)$$

The drag of the plate is therefore proportional to $U_\infty^{3/2}$ and to $l^{1/2}$, that is not proportional to l . This has to do with the fact that the parts of the plate at the rear contribute a relatively lower amount to the total drag than those at the front. This is because they are located in a region which has a thicker frictional layer and thus a smaller wall shear stress. If we want to estimate the value of drag coefficient in the usual manner, then we use the following equation:

$$C_D = \frac{2D}{\rho U_\infty^2 bl} \quad (7)$$

where the wetted area bl serves as a reference area.

5. Results and discussion

As all the car body dimensions are normalized with the body height H so the roughness height is also normalized by the same. As a result though simulations are done with the roughness heights 0.0001m, 0.0002m etc but plots are not showing that values. Let λ denotes that normalized roughness height.

Fig. 2 and Fig 3 are representing the over all effects of roughness height on the total drag coefficient for the k- ϵ turbulence model and RNG k- ϵ turbulence model respectively. From Fig. 2 it is clear that with the increase in the roughness height the total drag primarily decreases and latter increases, which indicates that k- ϵ turbulence model has dependency on the roughness height. On the other hand, from Fig. 3, the total drag increases rapidly with the increase in roughness height but after certain value though it remains increasing but the rate slows down.

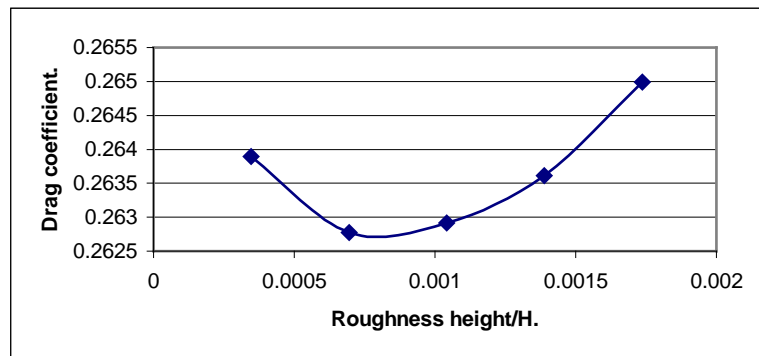


Fig.2. Drag coefficient profiles for different value of λ for k- ϵ turbulence model

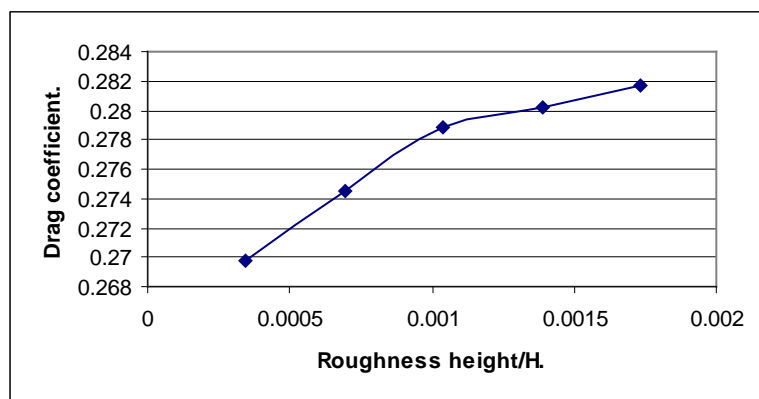


Fig.3. Drag coefficient profiles for different value of λ for RNG k- ϵ turbulence model

Not only the total drag is the matter of interest but also the drags at the nose, rear slope and at the back are of interest. Thus the drag coefficients at the nose, at the back and at the rear slope along with their sum treated as the total drag coefficients are tabulated for different values of the normalized roughness height in Table 1 and 2 for k- ϵ and RNG k- ϵ turbulence model respectively.

Table 1. Drag coefficient values for k-ε model.

Roughness height/Body height	Drag coefficient at the nose	Drag coefficient at the rear slope	Drag coefficient at the back	Total drag coefficient
0.0003472	0.01400	0.13589	0.11400	0.26389
0.0006944	0.01795	0.12892	0.11590	0.26277
0.0010416	0.02058	0.12505	0.11728	0.26291
0.0013888	0.02270	0.12203	0.11888	0.26361
0.0017360	0.02466	0.12012	0.12021	0.26499

It is seen from Table 1 that with the increase in the normalized roughness height the drag coefficient at the nose is continuously increasing. The drag coefficient at the back is also monotonously increases but the drag at the rear slope decreases with the increase in the normalized roughness height. These up and down effects finally have produced primary decrease and then increase effect. From Table it is observed that with the increase in the normalized roughness height the drag coefficient at the nose grows primarily faster but afterward slows down.

Table 2. Drag coefficient values for RNG k-ε model.

Roughness height/Body height	Drag coefficient at the nose	Drag coefficient at the rear slope	Drag coefficient at the back	Total drag coefficient
0.0003472	0.014552	0.115008	0.140176	0.269736
0.0006944	0.017966	0.115004	0.141573	0.274543
0.0010416	0.020612	0.114932	0.143282	0.278826
0.0013888	0.024207	0.113039	0.143021	0.280267
0.0017360	0.024788	0.114038	0.142814	0.281640

The drag coefficient at the back primarily increases but afterward decreases, whereas that at the rear slope primarily decreases and then increases, but the sum, the total drag coefficient increases continuously with the increase in the normalized roughness height.

Finally the minimum obtained coefficient of drags at the rear slant and at the back are tabulated in Table 3 to compare among k-ε and RNG k-ε turbulence models with LSTM benchmark values. It is observed that the simulations produced drags are comparable with the LSTM benchmarks.

Table 3. Comparison between drag coefficients of different models

Model	Drag coefficient at the rear slope	Drag coefficient at the back
LSTM	0.121	0.129
k-ε	0.1289	0.1159
RNG k-ε	0.115008	0.140176

6. Conclusion

In this paper Ahmed car body is used to view the effect of roughness height on k-ε and RNG k-ε turbulence models. On the basis of the observations it may be mentioned that

- i) k-ε turbulence model has dependency on the roughness height, so in simulations care must be taken to choose this parameter.
- ii) Drag coefficients at different positions do not show the same behaviour.
- iii) Both k-ε and RNG k-ε turbulence models have the capability to estimate drags comparable to the benchmark.

Wherever Times is specified, Times Roman or Times New Roman may be used.

7. References

- [1] H. Lienhart, C. Stoots, S. Becker, “Flow and turbulence structure on the wake of a simplified car model (Ahmed model)”, *DGLR Fach. Symp. der AG ATAB, Stuttgart University*, 2000.
- [2] G. Martinat, R. Bourguet, Y. Hoarau, F. Dehaeze, B. Jorez and M. Braza “ Numerical Simulation of the Flow in the Wake of Ahmed Body Using Detached Eddy Simulation and URANS Modeling”. *Peng S-H and Haase W (Eds.): Adv. in Hybrid RANS-LES Modeling; NNFM 97*, pp. 125-31, 2008.
- [3] S.R. Ahmed., G Ramm.,”Some Salient Features of the Time –Averaged Ground Vehicle Wake,” *SAE Technical Paper* 840300, 1984.
- [4] T.J. Craft,S. E.Gant, H. Iacovides and B.E. Launder, “ Computational study of flow around the Ahmed car body”, *9 th ERCOFTAC workshop on refined turbulence modeling, Darmstadt University of Technology, Germany*, 2001.
- [5] W.P. Jones and B.E. Launder, “The prediction of laminarization with a two-equation model, *Int. J. Heat and Mass Trans.*, Vol. 15, pp. 301-314, 1972.
- [6] V.Yakhot and S. A. Orazag , “Renormalization Group analysis of Turbulence, I. Basic Theory”, *Journal of Scientific Computing*, Vol. I, pp. 3-51, 1986.

Flow over Circular Cylinders in Axial Flow with Different Nose Shapes

Qin Sun, Md. Mahbub Alam*, C.W. Wong and Y. Zhou

Institute for Turbulence-Noise-Vibration Interaction and Control, Shenzhen Graduate School,
Harbin Institute of Technology, Shenzhen, China

*email: alam28@yahoo.com; alam@hitsz.edu.cn

Abstract

Wall pressure measurements were performed in the separation bubble and behind the shear-layer reattachment on a blunt circular cylinder in axial flow, with Reynolds number ranging from 3.3×10^3 to 5×10^4 based on the cylinder diameter and free-stream velocity. In addition, the effects of nose shape as well as yaw angle on the flow features were investigated with conical and hemispherical noses. Time-mean pressure coefficient C_p , fluctuating (rms) pressure coefficient C'_p , and power spectral density function of fluctuating pressure are presented. It was found that C_p and C'_p are highly sensitive to Re_D for the hemispherical nose. The blunt nose presents highest C'_p , while the hemispherical nose corresponds to the lowest C'_p . With increasing yaw angle from 0° to 3.5° , C_p declines and C'_p increases for both the blunt and conical cases, while those for hemispherical case vary less regularly.

Keywords: Separation, Axial and near-axial flow, Wall pressure, Nose shape.

1. Introduction

The typical configuration where flow separation and reattachment occur on the leading edge of a circular cylinder in axial flow is common in engineering field, such as aircraft fuselages, submarines, missiles, road vehicles, etc. The separation and reattachment of the flow lead to a formation of bubble/cavitation that is a major source of disturbance, vibration, and noise.

A number of works on the features of flow over a blunt cylinder have been done in the literature (e.g. [1-6]). The reattachment length x_R/D is a crucial parameter to characterize the flow near the leading edge. See Fig. 1 for the definition of x_R and D (cylinder diameter). The x_R/D dramatically decreases from 2.4 to 1.5 when the Reynolds number (Re_D) based on D varies from 2×10^3 to 10^4 . Beyond $Re_D = 10^4$, x_R/D is about 1.5 ~ 1.6, independent of Re_D . Ota & Mogegi [7] measured the turbulent characteristics using hotwire at $Re_D = 4.21 \times 10^4$ and observed that the turbulent boundary layer becomes fully developed at least a distance of $10D$ from the leading edge. Kiya et al. [2] measured the surface pressure fluctuation at $Re_D = 2 \times 10^5$ along the reattachment line with a number of pressure taps. They observed that the flow in the separation bubble oscillates at two different frequencies. While the low frequency was connected to the flapping motion of the separated shear layer, and the other was associated with the shedding of the large-scale vortices from the separated zone.

Though the front part (nose) of the body in engineering applications is not always blunt, but may be of the cone or hemispherical shape, fluid dynamics around a cylinder with a cone or hemispherical nose has received much less attention than that around a blunt cylinder. Tayler et al. [8] estimated the shedding frequencies of circular cylinders of cone-shaped nose and hemispherical nose from the power spectral density functions of sectional lift coefficients obtained by integrating the pressure data measured at 24 pressure taps at the mid-span of the model. They found that variation in normalized shedding frequency with Re_D from 1×10^4 to 3×10^4 was not significant in both cases.

Researches on features of flow near the leading edge of the blunt cylinder were conducted at some particular Re_D , while Re_D effects on the surface pressure fluctuation in the flow separation region is not yet well understood for not only blunt nose, but also cone-shaped and hemispherical noses. In addition, the incident flow on the cylinder-like submarines in reality is always not axial, but may at a small yaw angle. The effect of yaw angle on the leading edge flow behavior is however not well understood. In fact, the pressure fluctuation at a

point is the integrated effect of the velocity fluctuation, hence giving an overall picture of the flow around the point. In the present paper, the surface pressure fluctuation in the separation of circular cylinders with blunt, conical, hemispherical noses were investigated experimentally, with Re_D ranging from 3.3×10^3 to 5×10^4 . Apart from a cylinder in axial flow, the cylinder with yaw angle of 2° and 3.5° was studied, as well. Time-mean and rms pressures are measured at points immediately behind the shear-layer separation, ahead the reattachment and following the reattachment (Fig. 1a) and Re_D effects are discussed. FFT analysis of fluctuating pressures is also done to extract frequencies of shear-layer flapping and large-scale vortices.

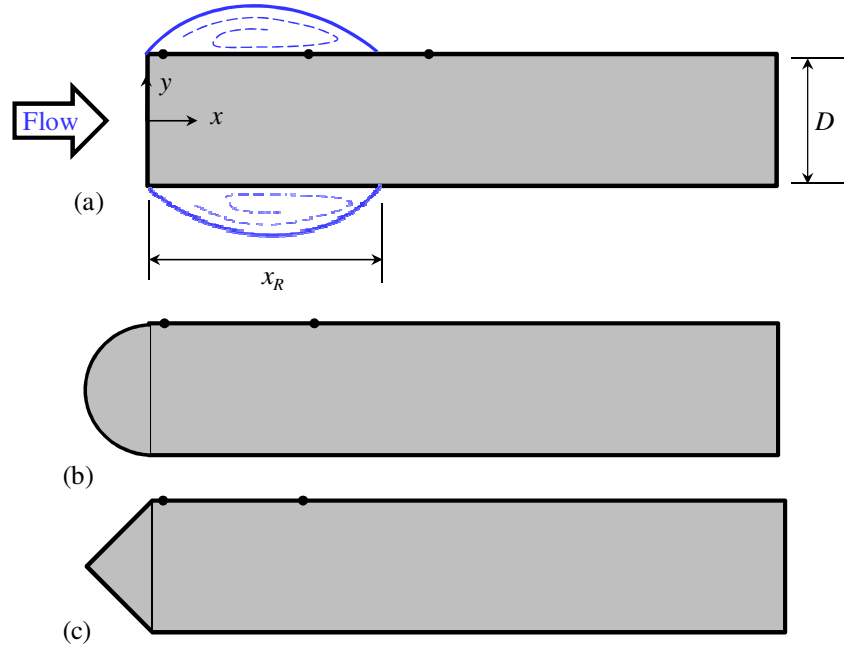


Fig. 1. Sketches of models. (a) Blunt cylinder and definition of reattachment length x_R , (b) hemispherical-nose cylinder, (c) cone-nose cylinder. Small solid circles denote the pressure tap positions.

2. Experimental approach

Experiments were performed in a closed-circuit wind tunnel with a 3-m-long test section of 0.9 m in width and 1.0 m in height. The flow non-uniformity was within $\pm 0.1\%$ (rms) within the central cross sectional area of $0.85 \text{ m} \times 0.95 \text{ m}$ in the test section, and the longitudinal turbulence intensity was less than 0.2% in the absence of the cylinder. The free-stream velocity, U_∞ was varied from 6.65 to 46.8 m/s. Two different cylinders of $D = 7.5$ and 16 , each having an aspect ratio of 12, were adopted to extend Re_D range from 3.3×10^3 to 5×10^4 . Furthermore, the cylinder with $D = 16 \text{ mm}$ was adopted with three noses, i.e., blunt, conical and hemispherical. The model was positioned horizontally at the centerline of the test section and supported by a L-shape stainless steel rod which was vertically fixed by a metal stand without being in contact with the wind tunnel wall, so that the model vibration caused by the wind tunnel can be avoided. Two yaw angles of $\alpha = 2^\circ$ and 3.5° are achieved through rotating a plate which holds the L-shape support.

It is known that x_R/D is larger than 1.5 at least over a wide range of Re_D as mentioned in the introduction. We were interested to know the difference in pressure fluctuations (i) immediately behind the separation, (ii) around the center of the separation bubble and (iii) behind the reattachment. Therefore three pressure taps on the cylinder of $D = 7.5 \text{ mm}$ at $x/D = 0.15$, 1.0 and 2.5 , respectively were made (Fig. 1). The cylinders of $D = 16 \text{ mm}$ were however furnished with two pressure taps only at $x/D = 0.15$ and 1.0 , respectively. Therefore, data for $x/D = 2.5$ will be available at $Re_D < 2.5 \times 10^4$ only. All the pressure taps were connected to a pressure transducer (Toyoda PD104K) with a small cavity between the pressure taps and the transducer diaphragm. The transducer had an excellent frequency response up to 450 Hz. For yaw angle cases, the pressure taps were on the downstream side.

3. Results and discussion

Figure 2 shows time-mean surface-pressure coefficient $C_p = (P - P_\infty)/(0.5\rho U_\infty^2)$ and fluctuating (rms) pressure coefficient C_p' at $x/D = 0.15, 1.0$ and 2.5 for the blunt cylinder, where P is the pressure on the cylinder surface, P_∞ is pressure in free-stream flow and ρ is the density of air. The figure also includes data from the literature, showing validation of the present measurements. At $Re_D = 3.3 \times 10^3 \sim 1.0 \times 10^4$, C_p and C_p' at $x/D = 1.0$ decline and increase, respectively, which is attributed to the fact that the reattachment of the separated shear layer proceeds towards the leading edge with Re_D which enhances the turbulence in the bubble. On the other hand, for $Re_D > 1.0 \times 10^4$, both C_p and C_p' tend to be constant as a result of the bubble size being almost insensitive to Re_D . However, the C_p and C_p' at $x/D = 0.15$ augment slightly, because the shear layer near the separation narrows when Re_D is increased. While C_p at $x/D = 0.15$ and 1.0 ranges between -0.52 and -0.68 , that at $x/D = 2.5$ is between -0.1 and 0.0 . The observation implies that C_p magnitude in the cavity is larger than that behind the reattachment. Ota's [1] data measured at $x/D \approx 0.15$ and 2.3 ($Re_D = 6.62 \times 10^4$) and Kiya et al.'s [2] data at $x/D \approx 0.8$ ($Re_D = 10^5$), both accord well with our present measurements, according to the trends of C_p . With an increase in Re_D , C_p' at $x/D = 2.5$ wanes rapidly. The waning of C_p' results from the combine effect of shifts of both shear-layer transition and reattachment to the upstream.

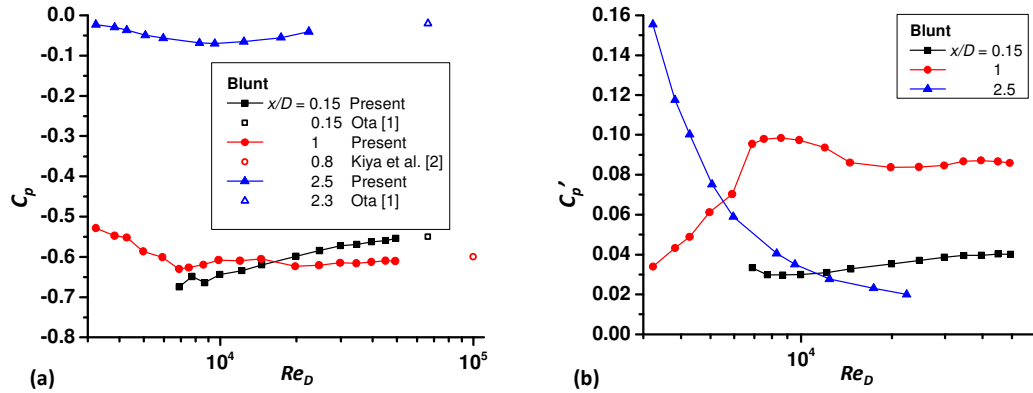


Fig. 2. Dependences on Re_D of (a) time-mean pressure coefficient C_p , and (b) fluctuating pressure coefficient C_p' .

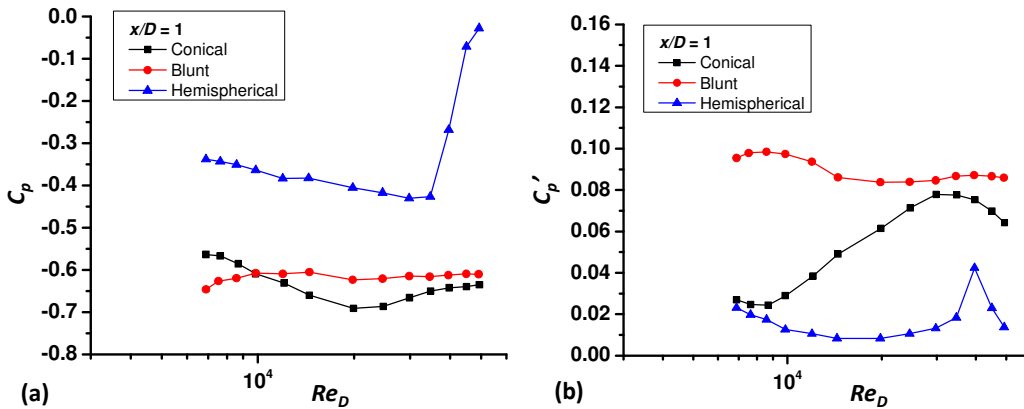


Fig. 3. Dependences on Re_D for the three nose shapes of (a) time-mean pressure coefficient C_p , and (b) fluctuating pressure coefficient C_p' .

Figure 3 compares C_p and C_p' at $x/D = 1.0$ between the three nose shapes. The magnitude of C_p is smaller for the hemispherical nose and larger for the conical nose, compared to that for the blunt nose. Furthermore C_p and C_p' are highly sensitive to Re_D for the hemispherical nose, due to easy shift of the separation point with increasing Re_D . The blunt nose presents the highest C_p' , while the hemispherical nose corresponds to the lowest C_p' . For hemispherical nose, a sharp peak in C_p' variation at $Re_D = 5 \times 10^4$ is observed and C_p around the same Re_D recovers drastically. Both observations indicate that the reattachment occurs beyond and before $x/D = 1.0$ for $Re_D < 5 \times 10^4$ and $Re_D > 5 \times 10^4$, respectively, and exactly at $x/D = 1.0$ at $Re_D = 5 \times 10^4$. On the other hand, for the blunt and conical noses, absences of recovery in C_p and sharp peak in C_p' suggest that the reattachment nestles beyond $x/D = 1.0$.

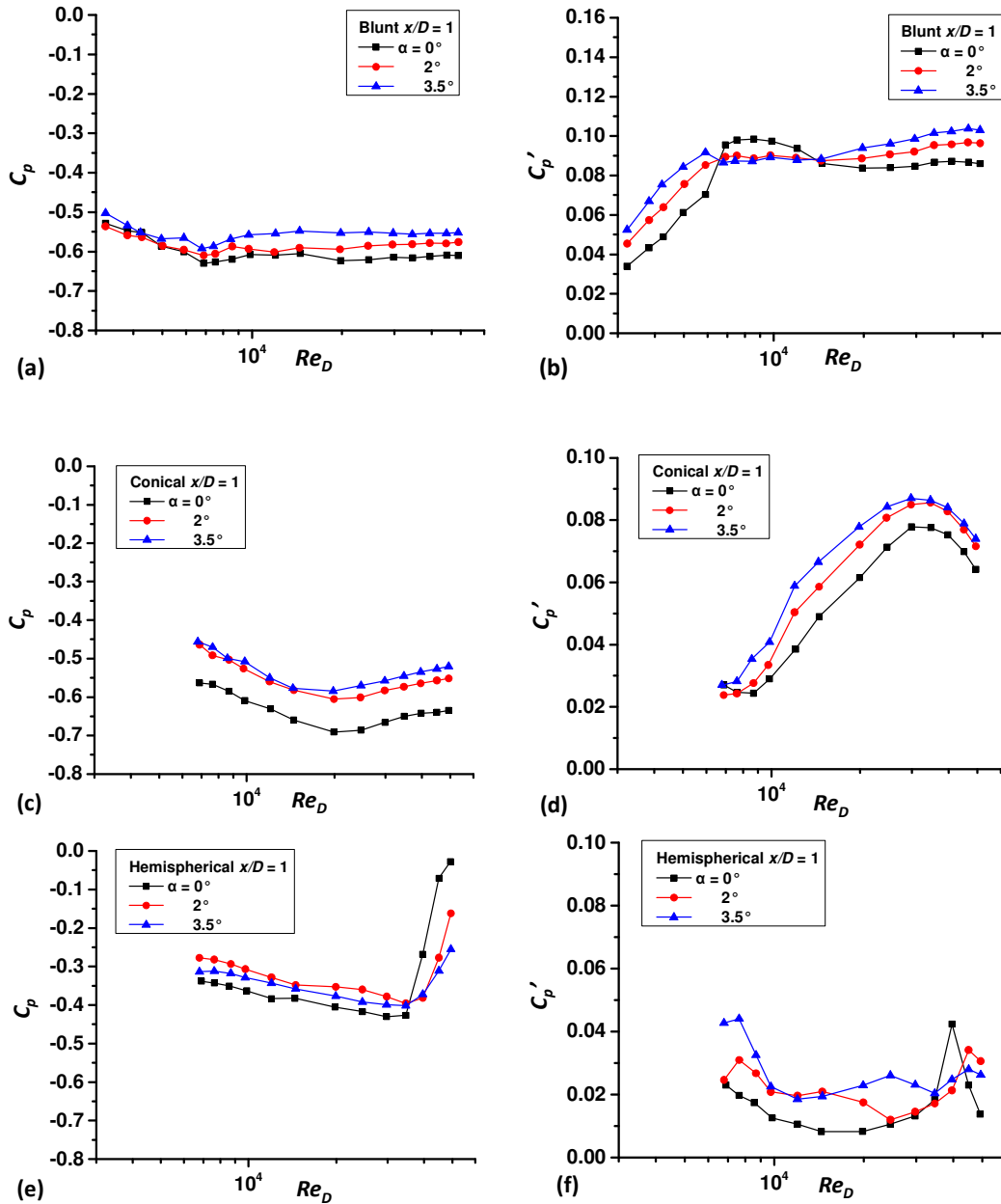


Fig. 4. Yaw angle effect on C_p and C_p' for (a, b) blunt nose, (c, d) conical nose, (e, f) hemispherical nose.

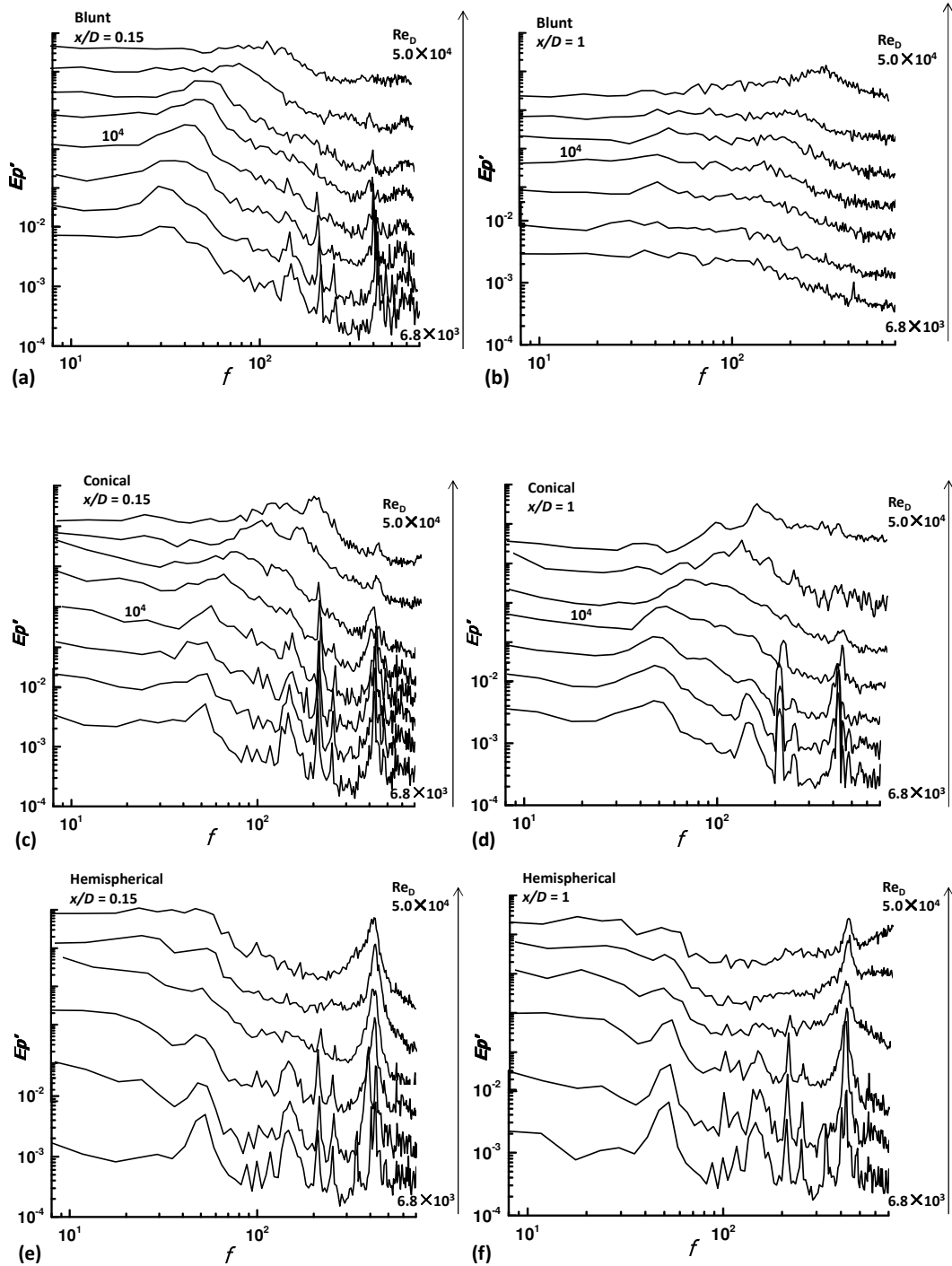


Fig. 5. Power spectral density functions E_p' of fluctuating pressure for three nose shapes at $\alpha = 0^\circ$, (a, c, e) $x/D = 0.15$ and (b, d, f) $x/D = 1.0$.

Figure 4 compares the yaw angle effect on C_p and C_p' for the three nose shapes. With increasing α from 0° to 3.5° , C_p magnitude reduces and C_p' is enhanced for both blunt and conical noses, while the magnitudes of C_p and C_p' for the hemispherical nose are small and variations with α are irregular. Flow around the cylinder at $\alpha \neq 0^\circ$ is highly three-dimensional and asymmetric around the cylinder axis, while that at $\alpha = 0^\circ$ is symmetric. The normal component of the flow at $\alpha \neq 0^\circ$ weakens the cavity intensity, resulting in C_p declining for both blunt and

conical noses. With increasing α , the bubble is elongated accordingly and the normal component makes an additional contribution to C_p' . On the other hand, both separation and reattachment points change with α for hemispherical nose, leading to an irregular change in C_p and C_p' . Again C_p recovery and peak in C_p' are observed for $\alpha \neq 0^\circ$ as well, but at higher Re_D .

Figure 5 illustrates power spectral density functions E_p' of fluctuating pressure for the three noses at $x/D = 0.15$ and 1.0. There are two frequencies that are worthy to be discussed. One is a low frequency, $f \approx 35 \sim 90$ Hz (Fig. 5a), and the other is a high frequency, $f \approx 120 \sim 300$ Hz (Fig. 5b), both increase with Re_D . The low frequency results from the flapping motion of the separated shear layer, and the other is associated with the shedding of the large-scale eddies from the separation region [2]. The low frequency is however about $f = 50 \sim 180$ and $55 \sim 60$ Hz for the conical and hemispherical noses, respectively, being less sensitive to Re_D for the latter case. The high frequency is not discernible for the conical and hemispherical noses, perhaps because they are much less bluff than the blunt one.

4. Conclusions

C_p , C_p' and power spectral density function of fluctuating pressure are examined for a cylinder with three nose shapes, namely, blunt, cone and hemisphere in a wide range of $Re_D = 3.3 \times 10^3 \sim 5 \times 10^4$. Measurements were conducted at three points on the cylinder, immediately behind the boundary-layer separation, in the separation bubble and behind the shear-layer reattachment. C_p behind the reattachment was found to be smaller in magnitude compared to the other points measured. For the blunt cylinder, at $Re_D = 3.3 \times 10^3 \sim 10^4$, the changing bubble size plays a significant role in determining both C_p and C_p' in the separation bubble. Beyond the Re_D range, C_p and C_p' in the separation bubble was less sensitive to Re_D because of the nearly unchanged bubble size. The magnitude of C_p is smaller for the hemispherical nose and larger for the conical nose compared to that for the blunt nose. Furthermore C_p and C_p' are highly sensitive to Re_D for the hemispherical nose, as a result of easy shift of the separation point with increasing Re_D . The blunt nose presents highest C_p' , while the hemispherical nose corresponds to the lowest C_p' . With increasing α from 0° to 3.5° , C_p declines and C_p' increases for both blunt and conical cases, while those for hemispherical case vary less regularly. The FFT analysis results of fluctuating pressure indicate that both low and high frequencies appear for the blunt nose, augmenting with the increasing Re_D . On the other hand, only the low frequency emerges for the conical and hemisphere noses.

5. Acknowledgement

Alam wishes to acknowledge supports given to him from Shenzhen Government through grant CB24405004 and from China Govt through '1000-young-talent-program'.

6. References

- [1] T. Ota, "An Axisymmetric Separated and Reattached Flow on a Longitudinal Blunt Circular Cylinder", Journal of Applied Mechanics, pp. 311-315, 1975.
- [2] M. Kiya, O. Mochizuki, H. Tamura, T. Nozawa, R. Ishikawa, and K. Kushioka, "Turbulence Properties of an Axisymmetric Separation-and-Reattaching Flow", AIAA Journal, Vol. 29, No. 6, pp. 936-941, 1991.
- [3] Y.F. Dong, Z.L. Wei, C. Xu, X.Q. Jiang, and Y.F. Liao, "on Separated Shear Layer of Blunt Circular Cylinder", Acta Mechanica Sinica, Vol. 13, No. 4, pp. 313-322, 1997.
- [4] H. Higuchi, H.Sawada, van Langen, and Pieter, "Flow over a Magnetically Suspended Cylinder in an Axial Free Stream", AIAA Paper 05-1078, 2005.
- [5] H. Higuchi, van Langen, H.Sawada, and C.E. Tinney, "Axial Flow over a Blunt Circular Cylinder with and without Shear Layer Reattachment", Journal of Fluids and Structures, Vol. 22, pp. 949-959, 2006.
- [6] H. Higuchi, H.Sawada, and H. Kato, "Sting-Free Measurements on a Magnetically Supported right Circular Cylinder aligned with the Free Stream", Journal of Fluid Mechanics, Vol. 596, pp. 49-72, 2008.
- [7] T. Ota, and H. Motegi, "Turbulence Measurements in an Axisymmetric Separated and Reattached Flow over a Longitudinal Blunt Circular Cylinder", Journal of Applied Mechanics, Vol. 47, pp. 1-6, 1980.
- [8] Z.J. Taylor, E. Palombi, R. Gurka, and G.A. Kopp, "Features of the turbulent flow around symmetric elongated bluff bodies", Journal of Fluids and Structures, Vol. 27, pp. 250-265, 2011.